Structural, vibrational and thermodynamic properties of carbon allotropes from first-principles: diamond, graphite, and nanotubes
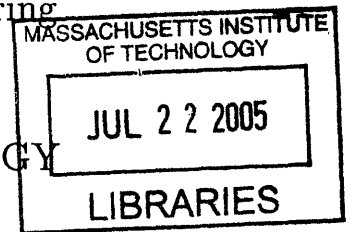
by

Nicolas Mounet

Submitted to the Department of Materials Science and Engineering
in partial fulfillment of the requirements for the degree of

Master of Science in Materials Science and Engineering

at the

MASSACHUSETTS INSTITUTE OF TECHNOLOGY

June 2005
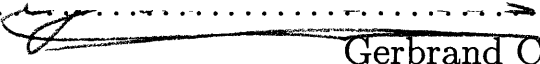
Author ....
Department of Materials Science and Engineering
February 23, 2005

Certified by...
Nicola Marzari
AMAX Assistant Professor in Computational Materials Science
Thesis Supervisor

Accepted by ....
Gerbrand Ceder
R. P. Simmons Professor of Materials Science and Engineering
Chairman, Department Committee on Graduate Students

Structural, vibrational and thermodynamic properties of carbon allotropes from first-principles: diamond, graphite, and nanotubes

by

Nicolas Mounet

Abstract

The structural, dynamical, and thermodynamic properties of different carbon allotropes are computed using a combination of ab-initio methods: density-functional theory for total-energy calculations and density-functional perturbation theory for lattice dynamics. For diamond, graphite, graphene, and armchair or zigzag single-walled nanotubes we first calculate the ground-state properties: lattice parameters, elastic constants and phonon dispersions and density of states. Very good agreement with available experimental data is found for all these, with the exception of the c/a ratio in graphite and the associated elastic constants and phonon dispersions. Agreement with experiments is recovered once the experimental c/a is chosen for the calculations. Results for carbon nanotubes confirm and expand available, but scarce, experimental data. The vibrational free energy and the thermal expansion, the temperature dependence of the elastic moduli and the specific heat are calculated using the quasi-harmonic approximation. Graphite shows a distinctive in-plane negative thermal-expansion coefficient that reaches its lowest value around room temperature, in very good agreement with experiments. The predicted value for the thermal-contraction coefficient of narrow single-walled nanotubes is half that of graphite, while for graphene it is found to be three times as large. In the case of graphene and graphite, the ZA bending acoustic modes are shown to be responsible for the contraction, in a direct manifestation of the membrane effect predicted by I. M. Lifshitz over fifty years ago. Stacking directly hinders the ZA modes, explaining the large numerical difference between the thermal-contraction coefficients in graphite and graphene, notwithstanding their common physical origin. For the narrow nanotubes studied, both the TA bending and the "pinch" modes play a dominant role. For larger single-walled nanotubes, it is postulated that the radial breathing mode will have the most significant effect on the thermal contraction, ultimately reaching the graphene limit as the diameter is increased.

3

Thesis Supervisor: Nicola Marzari
Title: AMAX Assistant Professor in Computational Materials Science

Acknowledgments

The work that I am going to present in the following pages was performed at MIT from January 2004 to February 2005. During that period, many things would not have been possible if a lot of people had not helped me in various ways. I would like to thank all of them, and I apologize in advance for any omission.

First and foremost, I am very grateful to my thesis supervisor, Prof. Nicola Marzari, for his exceptional kindness and availability, for his attention on all the issues, scientific or not, that I met, and for his strong support. He fully inspired and motivated the work I am presenting here. I also greatly enjoyed being part of his research group, both because of the great competence of all of its members and the very friendly atmosphere that was always present. They helped me on countless occasions with patience and care, and I personally thank all of them. In alphabetical order, they are Mayeul D'Avezac, Dr. Matteo Cococcioni, Ismaila Dabo, Dr. Cody Friesen, Boris Kozinsky, Heather Kulik, Young-Su Lee, Nicholas Miller, Dr. Damian Scherlis, Patrick Sit, Dr. Paolo Umari, and Brandon Wood.

I thank Dr. Paolo Giannozzi and Dr. Stefano de Gironcoli who were always very helpful in answering my questions. I also thank all the people developing the ν-Espresso code (http://www.pwscf.org/) for the truly exceptional work they are doing on this freely available *ab initio* code.

I gratefully acknowledge financial support from NSF-NIRT DMR-0304019 and the Interconnect Focus Center MARCO-DARPA 2003-IT-674.

I would also like to thank the Ecole Polytechnique of Palaiseau (France) and the Fondation de l'Ecole Polytechnique for making my studies in the USA possible.

I give many thanks to my parents and brothers for all their useful advice and their constant support.

Finally, I give my very special thanks to my wife Irina, who made my life so much easier. She has always been the strongest supporter of my work and study, whatever the cost was for her. My gratitude goes far beyond what I could express with words, and I am dedicating this thesis to her.

Contents

List of Figures

10

List of Tables

13

Chapter 1

Introduction

The extraordinary variety of carbon allotropes, as well as their present and potential applications in such diverse fields as nanoelectronics [1] or bioengineering [2] gives them a special place among all elements. Both experimental and computational studies are still needed to characterize fully these materials. For instance, single crystalline forms of carbon such as diamond, graphite and graphene (i.e. a single graphite layer) still lack a complete characterization of their thermodynamic stability under a broad range of conditions (see e.g. Refs. [3, 4, 5, 6, 7] and citations therein). As for fullerenes and the recently discovered carbon nanotubes [8] and their derivatives, even more investigations are needed. In particular, experimental data on single-walled carbon nanotubes (SWNTs) with a defined chirality are both scarce and very difficult to obtain, due the complexity of growth and manipulation of these low-dimensional materials. While structural constants are well known, elastic and thermodynamic properties are still under very active investigation (see e.g. Refs. [9, 10, 11, 12, 13, 14] and citations therein).

In particular, vibrational properties play a crucial role in determining the thermodynamic properties of all these materials. Indeed, diamond and semiconductor nanotubes exhibit a band gap (E_g= 5.5 eV for diamond, and for the typical semiconductor SWNTs that we study here — of diameter less than 1 nm — $E_g > 1$ eV [15, 16, 17]), so electronic excitations do not account for thermal properties up to high temperatures. Graphite, graphene and certain SWNTs are metallic, but the gap vanishes only

at isolated points in the Brillouin zone, where the two massless bands cross (see e.g. Refs. [15, 16]); thus, electronic excitations can often be neglected in these materials, and the phonon dispersions provide all the information that is needed to calculate thermodynamic quantities such as the thermal expansion or specific heat.

The aim of this thesis is to provide a converged, accurate determination of the structural, dynamical, and thermodynamic properties of diamond, graphite, graphene, rhombohedral graphite and zigzag and armchair SWNTs from first-principles. Although the phonon spectrum of diamond and its thermal properties have been studied extensively with experiments [18, 19] and calculations [20], the phonon spectra of graphite [21, 22] and SWNTs [23, 24, 25, 26, 27] are still under active investigation, as well as their thermal properties [28, 11, 10, 29, 12, 30, 31, 32]. Graphite in-plane thermal expansion has long been recognized to be negative [33, 34], and it has even been suggested [7, 34] that this may be due to the internal stresses related to the large expansion in the c direction (Poisson effect).

To resolve some of the open questions, and to provide a coherent theoretical picture for all these materials, we used extensive ab-initio density-functional theory (DFT) and density-functional perturbation theory (DFPT) [35, 36] calculations. DFT is a very efficient and accurate tool to obtain ground-state and linear-response properties, especially when paired with plane-wave basis sets, which easily allow to reach full convergence with respect to basis size, and ultrasoft pseudo-potentials [37] for optimal performance and transferability. We adopted the PBE-GGA [38] exchange-correlation functional, at variance with most of the ab-initio studies on diamond [20, 39, 40], graphite [41, 42, 22, 23, 43, 24] and nanotubes [23, 24, 25, 27], which have been performed using the local density approximation (LDA). GGA calculations have appeared mostly for the cases of diamond (GGA-PBE, Ref. [40]) and graphene (GGA-PBE, Refs. [21, 22]), with some data for graphite appearing in Refs. [44, 45, 22, 46] (GGA-PBE) and for nanotubes in Refs. [47, 48, 49, 50] (mostly GGA-PBE). DFPT [35, 36] is then used to compute the phonon frequencies at any arbitrary wave-vector, without having to resort to the use of supercells. The vibrational free energy is calculated in the quasi-harmonic approximation (QHA) [20, 51], to predict

finite-temperature lattice properties such as thermal expansion and specific heat.

To the best of our knowledge, this is the first study on the thermodynamic properties of graphite, graphene or SWNTs from first-principles. For the case of diamond, graphene and SWNTs, calculations are fully ab-initio and do not use any experimental input. For the case of graphite and rhombohedral graphite we argue that the use of the experimental c/a greatly improves the agreement with experimental data. This experimental input is required since DFT, in its current state of development, yields poor predictions for the interlayer interactions, dominated by Van Der Waals dispersion forces not well described by local or semi-local exchange correlation functionals (see Refs. [52] and [53] for details; the agreement between LDA predictions and experimental results for the c/a ratio is fortuitous). It is found that the weak interlayer bonding has a small influence on most of the properties studied and that forcing the experimental c/a corrects almost all the remaining ones. This allows us to obtain results for all the materials considered that are in very good agreement with the available experimental data.

This thesis is structured as follows. We give a brief summary of our approach and definitions and introduce DFPT and the QHA in Chapter 2. Our ground-state, zero-temperature results for diamond, graphite, graphene, rhombohedral graphite and SWNTs are presented in Chapter 3: Lattice parameters and elastic constants from the equations of state in Section 3.1, phonon frequencies and vibrational density of states in Section 3.2, and first-principles, linear-response interatomic force constants in Section 3.3. The lattice thermal properties, such as thermal expansion, mode Grüneisen parameters, and specific heat as obtained from the vibrational free energy are presented in Chapter 4. Chapter 5 contains our final remarks.

Chapter 2

Theoretical framework

2.1 Crystalline structures studied

2.1.1 Diamond

The structure of diamond is that of an FCC Bravais lattice with a two-atom basis —
one at the origin and one at one-fourth of the cube diagonal. The carbon atoms are
bound together by sp^3 bonds. The lattice constant a is the length of the side of the
conventional cubic unit cell. Fig. 2-1 shows the crystal structure of diamond.

a
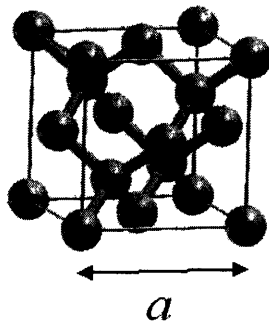
Figure 2-1: Crystal structure of diamond, together with the conventional (cubic) unit
cell. a is the lattice constant.
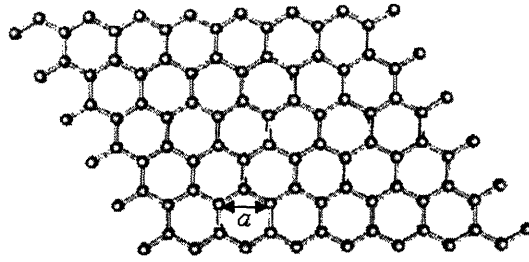
Figure 2-2: Crystal structure of graphene. a is the in-plane lattice parameter.

2.1.2 Graphene, graphite and rhombohedral graphite

Graphene is a two-dimensional monolayer of carbon atoms bound together by sp^2 bonds. It exhibits a hexagonal "honeycomb" crystal lattice containing two atoms per unit cell, as shown in Fig. 2-2. A single parameter characterizes this structure: the distance a between two equivalent atoms in the lattice (which is also the distance between an atom and its second nearest neighbors).

Graphite is made of graphene sheets bound together by Van der Waals forces. The layers are stacked with a periodic pattern of type "ABABAB...": the B layers are shifted with respect to the A ones such that the centers of the hexagonal cells of B lie directly above an atom of A (see Fig. 2-3). Rhombohedral graphite is stacked "AB-CABC..." (see Fig. 2-3). Both of these three-dimensional structures are represented by an hexagonal lattice whose primitive cell contains four atoms for graphite and six for rhombohedral graphite. Note that rhombohedral graphite can be equivalently represented by a rhombohedral lattice whose unit cell contains only two atoms. Both of these structures are fully characterized by the in-plane lattice parameter a (same as in graphene) and the out-of-plane parameter c equal to two (graphite) or three (rhombohedral graphite) times the interlayer distance.

2.1.3 Achiral nanotubes

A single-walled nanotube is a quasi-one-dimensional system obtained by rolling one graphene sheet on itself in such a way that a graphene lattice vector **c** becomes the
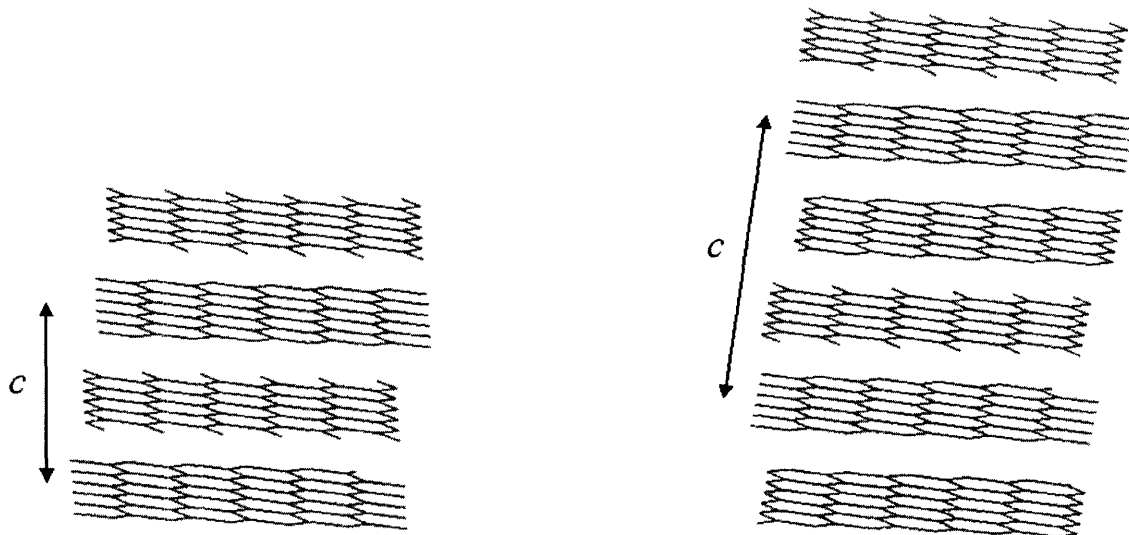
Figure 2-3: Crystal structure of graphite and rhombohedral graphite. c is the out-of-plane lattice parameter

circumference of the tube. **c** is called the chiral vector, and its components in terms of the two primitive vectors of graphene indicate the chirality of the nanotube. For achiral nanotubes, these two chirality indices are either in the form (n, n) (armchair SWNT) or $(n, 0)$ (zigzag SWNT), where n is an integer. In Fig. 2-4 we show the chiral vector on the graphene lattice for both armchair and zigzag nanotubes. Periodicity of a SWNT occurs only in one dimension (along its axis); for achiral tubes (n, n) or $(n, 0)$ the unit cell contains $4n$ atoms. Such a unit cell is shown for the cases of the armchair (5,5) and zigzag (8,0) nanotubes in Figs. 2-5 and 2-6. Once the chirality of a SWNT is fixed, usually two parameters are sufficient to characterize its structure: the radius r and the length l of the unit cell (see Figs. 2-5, 2-6, 2-7 and 2-8).

More details on the general structure of SWNTs can be found in Ref. [16].

2.2 Density-Functional Perturbation Theory

In density-functional theory [54, 55] the ground state electronic density and wavefunctions of a crystal are found by solving self-consistently a set of one-electron equations. In atomic units (used throughout the article), these are
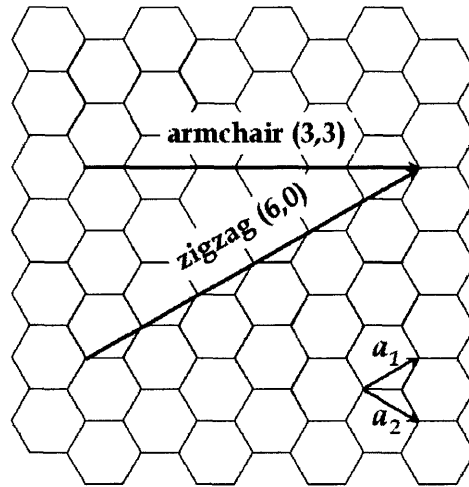
Figure 2-4: Chiral vectors for armchair and zigzag SWNTs. The primitive lattice vectors of graphene (a_1, a_2) are also shown (courtesy of Young-Su Lee, MIT).
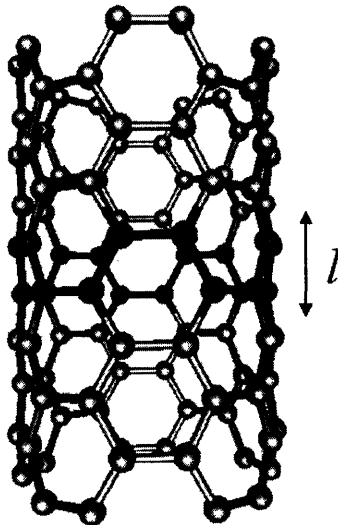
Figure 2-5: Structure of an armchair (5,5) SWNT. The primitive unit cell is highlighted in black.
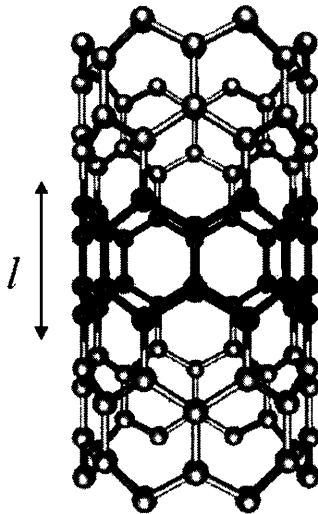
Figure 2-6: Structure of a zigzag (8,0) SWNT. The primitive unit cell is highlighted in black
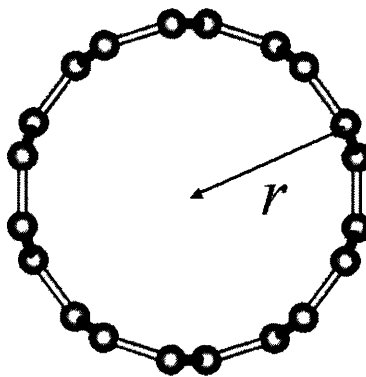
Figure 2-7: Axial view of an armchair (5,5) SWNT
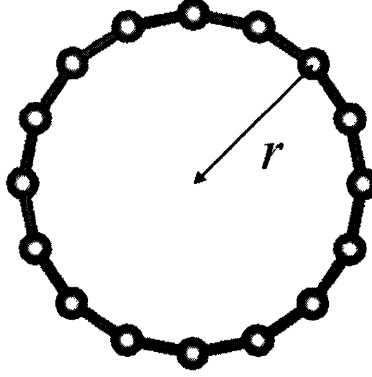
Figure 2-8: Axial view of a zigzag (8,0) SWNT

$$(-\frac{1}{2}\nabla^2 + V_{SCF}(\mathbf{r}))|\psi_i\rangle = \varepsilon_i|\psi_i\rangle, \tag{2.1a}$$

$$V_{SCF}(\mathbf{r}) = \int \frac{n(\mathbf{r}')}{|\mathbf{r}-\mathbf{r}'|}d^3\mathbf{r}' + \frac{\delta E_{xc}}{\delta(n(\mathbf{r}))} + V_{ion}(\mathbf{r}), \tag{2.1b}$$

$$n(\mathbf{r}) = \sum_i |\psi_i(\mathbf{r})|^2 f(\varepsilon_F - \varepsilon_i), \tag{2.1c}$$

where $f(\varepsilon_F - \varepsilon_i)$ is the occupation function, ε_F the Fermi energy, E_{xc} the exchange-correlation functional (approximated by GGA-PBE in our case), $n(\mathbf{r})$ the electronic-density, and $V_{ion}(\mathbf{r})$ the ionic core potential (actually a sum over an array of pseudo-potentials).

Once the unperturbed ground state is determined, phonon frequencies can be obtained from the interatomic force constants, i.e. the second derivatives at equilibrium of the total crystal energy versus displacements of the ions:

$$C_{\alpha i,\beta j}(\mathbf{R}-\mathbf{R}') = \frac{\partial^2 E}{\partial u_{\alpha i}(\mathbf{R})\partial u_{\beta j}(\mathbf{R}')}\bigg|_{equil}$$

$$= C_{\alpha i,\beta j}^{ion}(\mathbf{R}-\mathbf{R}') + C_{\alpha i,\beta j}^{elec}(\mathbf{R}-\mathbf{R}')$$

$$\tag{2.2}$$

Here $\mathbf{R}$ ($\mathbf{R}'$) is a Bravais lattice vector, i (j) indicates the ith (j^{th}) atom of the unit cell, and $\alpha(\beta)$ represents the cartesian components. $C_{\alpha i, \beta j}^{ion}$ are the second derivatives [36] of Ewald sums corresponding to the ion-ion repulsion potential, while the electronic contributions $C_{\alpha i, \beta j}^{elec}$ are the second derivatives of the electron-electron and electron-ion terms in the ground state energy. From the Hellmann-Feynman theorem [36] one obtains:

$$C_{\alpha i, \beta j}^{elec}(\mathbf{R} - \mathbf{R}') = \int \left[\frac{\partial n(\mathbf{r})}{\partial u_{\alpha i}(\mathbf{R})} \frac{\partial V_{ion}(\mathbf{r})}{\partial u_{\beta j}(\mathbf{R}')} + n_0(\mathbf{r}) \frac{\partial^2 V_{ion}(\mathbf{r})}{\partial u_{\alpha i}(\mathbf{R}) \partial u_{\beta j}(\mathbf{R}')} \right] d^3\mathbf{r} \qquad (2.3)$$

(where the dependence of both $n(\mathbf{r})$ and $V_{ion}(\mathbf{r})$ on the displacements has been omitted for clarity, and $V_{ion}(\mathbf{r})$ is considered local).

It is seen that the electronic contribution can be obtained from the knowledge of the linear response of the system to a displacement. The key assumption is then the Born-Oppenheimer approximation which views a lattice vibration as a static perturbation on the electrons. This is equivalent to say that the response time of the electrons is much shorter than that of ions, that is, each time ions are slightly displaced by a phonon, electrons instantaneously rearrange themselves in the state of minimum energy of the new ionic configuration. Therefore, static linear response theory can be applied to describe the behavior of electrons upon a vibrational excitation.

For phonon calculations, we consider a periodic perturbation ΔV_{ion} of wave-vector $\mathbf{q}$, which modifies the self-consistent potential V_{SCF} by an amount ΔV_{SCF}. The linear response in the charge density $\Delta n(\mathbf{r})$ can be found using first-order perturbation theory. If we consider its Fourier transform $\Delta n(\mathbf{q} + \mathbf{G})$, and calling $\psi_{o,\mathbf{k}}$ the one-particle wavefunction of an electron in the occupied band "o" at the point $\mathbf{k}$ of the Brillouin zone (and $\varepsilon_{o,\mathbf{k}}$ the corresponding eigenvalue), one can get a self-consistent set of linear equations similar to Eqs. (2.1) [56]:

$$(\varepsilon_{o,\mathbf{k}} + \frac{1}{2}\nabla^2 - V_{SCF}(\mathbf{r}))\Delta\psi_{o,\mathbf{k}+\mathbf{q}} = \hat{P}_e^{\mathbf{k}+\mathbf{q}}\Delta V_{SCF}^{\mathbf{q}}\psi_{o,\mathbf{k}} \qquad (2.4a)$$

$$\Delta n(\mathbf{q} + \mathbf{G}) = \frac{4}{V} \sum_{\mathbf{k},o} \langle \psi_{e,\mathbf{k}} | e^{-i(\mathbf{q}+\mathbf{G})\cdot\mathbf{r}} \hat{P}_e^{\mathbf{k}+\mathbf{q}} | \Delta\psi_{o,\mathbf{k}+\mathbf{q}} \rangle \tag{2.4b}$$

$$\Delta V_{SCF}(\mathbf{r}) = \int \frac{\Delta n(\mathbf{r}')}{|\mathbf{r} - \mathbf{r}'|} d^3\mathbf{r}' + \Delta n(\mathbf{r}) \left[\frac{d}{dn} \left(\frac{\delta E_{xc}}{\delta(n(\mathbf{r}))} \right) \right]_{n_0(\mathbf{r})} + \Delta V_{ion}(\mathbf{r}) \tag{2.4c}$$

$\hat{P}_e^{\mathbf{k}+\mathbf{q}}$ refers to the projector on the empty-state manifold at $\mathbf{k} + \mathbf{q}$, V to the total crystal volume, and $\mathbf{G}$ to any reciprocal lattice vector. Note that the linear response contains only Fourier components of wave vector $\mathbf{q} + \mathbf{G}$, so we add a superscript $\mathbf{q}$ to $\Delta V_{SCF}^{\mathbf{q}}$. We implicitly assume for simplicity that the crystal has a band gap and that pseudo-potentials are local, but the generalization to metals [57] and to non-local pseudo-potentials [36] are all well established (see Ref. [35] for a detailed and complete review of DFPT).

Linear-response theory allows us to calculate the response to any periodic perturbation; i.e. it allows direct access to the dynamical matrix related to the interatomic force constants via a Fourier transform:

$$\tilde{D}_{\alpha i, \beta j}(\mathbf{q}) = \frac{1}{\sqrt{M_i M_j}} \sum_{\mathbf{R}} C_{\alpha i, \beta j}(\mathbf{R}) \, e^{-i\mathbf{q}\cdot\mathbf{R}} \tag{2.5}$$

(where M_i is the mass of the ith atom).

Phonon frequencies at any $\mathbf{q}$ are the solutions of the eigenvalue problem:

$$\omega^2(\mathbf{q})u_{\alpha i}(\mathbf{q}) = \sum_{\beta j} u_{\beta j}(\mathbf{q})\tilde{D}_{\alpha i, \beta j}(\mathbf{q}) \tag{2.6}$$

In practice, one calculates the dynamical matrix on a relatively coarse grid in the Brillouin zone (say, a $8 \times 8 \times 8$ grid for diamond), and obtains the corresponding interatomic force constants by inverse Fourier transform (in this example it would correspond to a $8 \times 8 \times 8$ supercell in real space). Finally, the dynamical matrix (and phonon frequencies) at any $\mathbf{q}$ point can be obtained by Fourier interpolation of the real-space interatomic force constants.

2.3   Thermodynamic properties

When no external pressure is applied to a solid, the equilibrium structure at any temperature T can be found by minimizing the Helmholtz free energy $F(\{a_i\}, T) = U - TS$ with respect to all its geometrical degrees of freedom $\{a_i\}$. If now the crystal is supposed to be perfectly harmonic, F is the sum of the ground state total energy and the vibrational free energy coming from the partition function (in the canonical ensemble) of a collection of independent harmonic oscillators. In a straightforward manner, it can be shown [58] that:

$$
\begin{aligned}
F(\{a_i\}, T) &= E(\{a_i\}) + F_{vib}(T) \\
&= E(\{a_i\}) + \sum_{\mathbf{q},j} \frac{\hbar\omega_{\mathbf{q},j}}{2} + k_B T \sum_{\mathbf{q},j} \ln\left(1 - \exp\left(-\frac{\hbar\omega_{\mathbf{q},j}}{k_B T}\right)\right)
\end{aligned}
$$

$$(2.7)$$

where $E(\{a_i\})$ is the ground state energy and the sums run over all the Brillouin zone wave-vectors and the band index j of the phonon dispersions. The second term in the right hand side of Eq. (2.7) is the zero-point motion.

If anharmonic effects are neglected, the phonon frequencies do not depend on lattice parameters, therefore the free energy dependence on structure is entirely contained in the equation of state $E(\{a_i\})$. Consequently the structure does not depend on temperature in a harmonic crystal.

Thermal expansion is recovered by introducing in Eq. (2.7) the dependence of the phonon frequencies on the structural parameters $\{a_i\}$; direct minimization of the free energy

$$
\begin{aligned}
F(\{a_i\}, T) &= E(\{a_i\}) + F_{vib}(\omega_{\mathbf{q},j}(\{a_i\}), T) \\
&= E(\{a_i\}) + \sum_{\mathbf{q},j} \frac{\hbar\omega_{\mathbf{q},j}(\{a_i\})}{2} + k_B T \sum_{\mathbf{q},j} \ln\left(1 - \exp\left(-\frac{\hbar\omega_{\mathbf{q},j}(\{a_i\})}{k_B T}\right)\right)
\end{aligned}
$$

$$(2.8)$$

provides the equilibrium structure at any temperature T. This approach goes under the name *quasi-harmonic approximation* (QHA) and has been applied successfully to many bulk systems [20, 59, 60]. The linear thermal expansion coefficients of the cell dimensions of a lattice are then

$$\alpha_i = \frac{1}{a_i}\frac{\partial a_i}{\partial T} \qquad (2.9)$$

The Grüneisen formalism [61] assumes a linear dependence of the phonon frequencies on the three orthogonal cell dimensions $\{a_i\}$; developing the ground state energy up to second order (thanks to the equation of state at $T = 0K$) one can get from the condition $\left(\frac{\partial F}{\partial a_i}\right)_T = 0$ the alternative expression

$$\alpha_i = \sum_{\mathbf{q},j} c_v(\mathbf{q},j) \sum_k \frac{S_{ik}}{V_0} \left(\frac{-a_{0,k}}{\omega_{0,\mathbf{q},j}} \frac{\partial \omega_{\mathbf{q},j}}{\partial a_k}\bigg|_0 \right) \qquad (2.10)$$

We follow here the formalism of Ref. [10]: $c_v(\mathbf{q},j)$ is the contribution to the specific heat from the mode $(\mathbf{q},j)$, S_{ik} is the elastic compliance matrix, and the subscript "0" indicates a quantity taken at the ground state lattice parameter. The Grüneisen parameter of the mode $(\mathbf{q},j)$ is by definition

$$\gamma_k(\mathbf{q},j) = \frac{-a_{0,k}}{\omega_{0,\mathbf{q},j}} \frac{\partial \omega_{\mathbf{q},j}}{\partial a_k}\bigg|_0 \qquad (2.11)$$

For a structure which depends only on one lattice parameter a (e.g. diamond or graphene) one then gets for the linear thermal expansion coefficient

$$\alpha = \frac{1}{a_0^2 \frac{\partial^2 E}{\partial a^2}\big|_0} \sum_{\mathbf{q},j} c_v(\mathbf{q},j) \frac{-a_0}{\omega_{0,\mathbf{q},j}} \frac{\partial \omega_{\mathbf{q},j}}{\partial a}\bigg|_0 \qquad (2.12)$$

In the case of graphite there are two lattice parameters: a in the basal plane and c perpendicular to the basal plane (see Section 2.1.2), so that one gets

$$\alpha_a = \frac{1}{V_0} \sum_{\mathbf{q},j} c_v(\mathbf{q},j) \left((S_{11} + S_{12}) \frac{-a_0}{2\omega_{0,\mathbf{q},j}} \frac{\partial \omega_{\mathbf{q},j}}{\partial a}\bigg|_0 + S_{13} \frac{-c_0}{\omega_{0,\mathbf{q},j}} \frac{\partial \omega_{\mathbf{q},j}}{\partial c}\bigg|_0 \right) \qquad (2.13a)$$

$$\alpha_c = \frac{1}{V_0} \sum_{\mathbf{q},j} c_v(\mathbf{q},j) \left(S_{13} \frac{-a_0}{\omega_{0,\mathbf{q},j}} \left. \frac{\partial \omega_{\mathbf{q},j}}{\partial a} \right|_0 + S_{33} \frac{-c_0}{\omega_{0,\mathbf{q},j}} \left. \frac{\partial \omega_{\mathbf{q},j}}{\partial c} \right|_0 \right) \qquad (2.13b)$$

Finally, in the case of SWNTs, when calculating the thermal properties we will use only one parameter, the length l of the unit cell, and relax the other degrees of freedom (in particular the radius). Therefore the linear thermal expansion coefficient according to the Grüneisen formalism is given by exactly the same equation as for diamond and graphene (Eq. 2.12), substituting l to a wherever it appears.

The mode Grüneisen parameters provide useful insight in the thermal expansion mechanisms. They are usually positive, since phonon frequencies decrease when the solid expands, although some negative mode Grüneisen parameters for low-frequency acoustic modes can arise and sometimes compete with positive ones, giving a negative thermal expansion at low temperatures, when only the lowest acoustic modes can be excited.

Finally, the heat capacity per unit cell at constant volume can be obtained from $C_v = -T \left(\frac{\partial^2 F_{vib}}{\partial T^2} \right)_V$ [58]:

$$C_v = \sum_{\mathbf{q},j} c_v(\mathbf{q},j) = k_B \sum_{\mathbf{q},j} \left(\frac{\hbar \omega_{\mathbf{q},j}}{2k_B T} \right)^2 \frac{1}{\sinh^2 \left(\frac{\hbar \omega_{\mathbf{q},j}}{2k_B T} \right)} \qquad (2.14)$$

2.4 Computational details

All the calculations that follow are performed using the ν-ESPRESSO [62] package, which is a full ab-initio DFT and DFPT code available under the GNU Public License [63], developed by a consortium of universities including our own group, and to which several additions were made as a direct outcome of this work. We use a plane-wave basis set, ultrasoft pseudo-potentials [37] from the standard distribution [64] (generated using a modified RRKJ [65] approach), and the generalized gradient approximation (GGA) for the exchange-correlation functional in its PBE parameterization [38]. We also use the local density approximation (LDA) in order to compare some results between the two functionals. In this case the parameterization used is the one proposed by Perdew and Zunger [66].

In all the calculations, periodic boundary conditions have to be set in all three directions. The three-dimensional crystals diamond, graphite and rhombohedral graphite are naturally fitting such boundary conditions, but the two-dimensional graphene sheet and quasi-one-dimensional SWNTs are not. These are still periodically repeated in all the directions, but a large amount of vacuum is introduced between periodic images. For graphene, periodic sheets are separated by a considerable interlayer distance – much larger than that of graphite. SWNTs are put into a tetragonal lattice whose out-of-plane lattice parameter corresponds to the height l of the nanotube unit cell (see Section 2.1.3) while the in-plane lattice constant is set to a large value compared to the radius of the SWNT.

For the semi-metallic graphite and graphene cases, we use 0.03 Ryd of cold smearing [67], and 0.05 Ryd in the case of armchair metallic SWNT. We carefully and extensively check the convergence in the energy differences between different configurations and the phonon frequencies with respect to the wavefunction cutoff, the dual (i.e. the ratio between charge density cutoff and wavefunction cutoff), the k-point sampling of the Brillouin zone, and the vacuum spacing for graphene and nanotubes. Energy differences are converged within 5 meV/atom or better, and phonon frequencies within $5\,\mathrm{cm}^{-1}$. In the case of graphite, graphene and metallic SWNT phonon frequencies are converged with respect to the k-point sampling after having fixed the smearing parameter. Besides, for graphite and graphene values of the smearing between 0.02 Ryd and 0.04 Ryd do not change the frequencies by more than $5\,\mathrm{cm}^{-1}$. On the contrary some armchair SWNT phonon frequencies are more sensible to the smearing, especially a few optical modes around Γ. This is due to the Kohn anomalies [68, 46], but since these only affect high optical frequencies the influence on the thermodynamic properties is negligible.

In a solid, translational invariance guaranties that three phonon frequencies at Γ will go to zero. In our GGA-PBE DFPT formalism this condition is exactly satisfied only in the limit of infinite k-point sampling and full convergence with the plane-wave cutoffs. For the case of graphene and graphite we found in particular that an exceedingly large cutoff (100 Ryd) and dual (28) would be needed to recover

phonon dispersions (especially around Γ and the $\Gamma - A$ branch) with the tolerances mentioned; on the other hand, application of the acoustic sum rule (i.e. forcing the translational symmetry on the interatomic force constants) allows us to recover these highly converged calculations with a more reasonable cutoff and dual. The same remark applies for the rotational invariance of SWNTs. Indeed, these one-dimensional systems have a fourth phonon frequency going to zero at Γ, since they are invariant for continuous rotations around their axis. Very high cutoffs and vacuum separations would be needed to obtain numerically this zero-frequency limit; forcing the corresponding rotational acoustic sum rule allows us to recover it with more reasonable choices of computational parameters. Applying the rotational sum rules is less straightforward than applying the translational ones, and we refer the reader to Appendix A for a detailed explanation of our approach to enforce these.

Finally, the cutoffs used are 40 Ryd for the wavefunctions in all the carbon materials presented, except for SWNTs where 30 Ryd is used. The dual is 8 for diamond and 12 for graphite, graphene and nanotubes, corresponding to a charge density cutoff of 320 Ryd for diamond, 480 Ryd for graphite and graphene, and 360 Ryd for SWNTs. We use a $8 \times 8 \times 8$ Monkhorst-Pack mesh for the Brillouin zone sampling in diamond, $16 \times 16 \times 8$ in graphite, $16 \times 16 \times 4$ in rhombohedral graphite, $16 \times 16 \times 1$ in graphene, $1 \times 1 \times 8$ in zigzag SWNTs and $1 \times 1 \times 12$ in armchair SWNTs. All these meshes are not shifted (i.e. they include Γ). The dynamical matrix is explicitly calculated on a $8 \times 8 \times 8$ q-points mesh in diamond, $8 \times 8 \times 4$ in graphite, $8 \times 8 \times 2$ in rhombohedral graphite, $16 \times 16 \times 1$ in graphene, $1 \times 1 \times 4$ in the nanotubes.

Finally, integrations over the Brillouin zone for the vibrational free energy or the heat capacity are done using phonon frequencies that are Fourier interpolated on much finer meshes. The phonon frequencies are usually computed at several lattice parameters and the results interpolated to get their dependence on lattice constants.

Chapter 3

Zero-temperature results

3.1 Structural and elastic properties

We perform ground state total-energy calculations on diamond, graphite, graphene and SWNTs over a broad range of lattice parameters. The potential energy surface is then fitted by an appropriate equation of state, and its minimum provides theoretical predictions for the ground state equilibrium lattice parameter(s). The second derivatives at the minimum are related to the bulk modulus and elastic constants.

3.1.1 Diamond

The equation of state of diamond over a broad range of lattice parameters is plotted in Fig. 3-1. We choose the Birch equation of state [69] (up to the fourth order) to fit the total energy vs. the lattice constant a:

$$
\begin{aligned}
E(a) = \ & -E_0 + \frac{9}{8} B_0 V_0 \left[\left(\frac{a_0}{a} \right)^2 - 1 \right]^2 + A \left[\left(\frac{a_0}{a} \right)^2 - 1 \right]^3 \\
& + B \left[\left(\frac{a_0}{a} \right)^2 - 1 \right]^4 + \mathcal{O} \left(\left(\frac{a_0}{a} \right)^2 - 1 \right)^5
\end{aligned}
\tag{3.1}
$$

where B_0 is the bulk modulus, V_0 the primitive cell volume (here $V_0 = \frac{a^3}{4}$) and A and B are fit parameters. The Murnaghan equation of state or even a polynomial
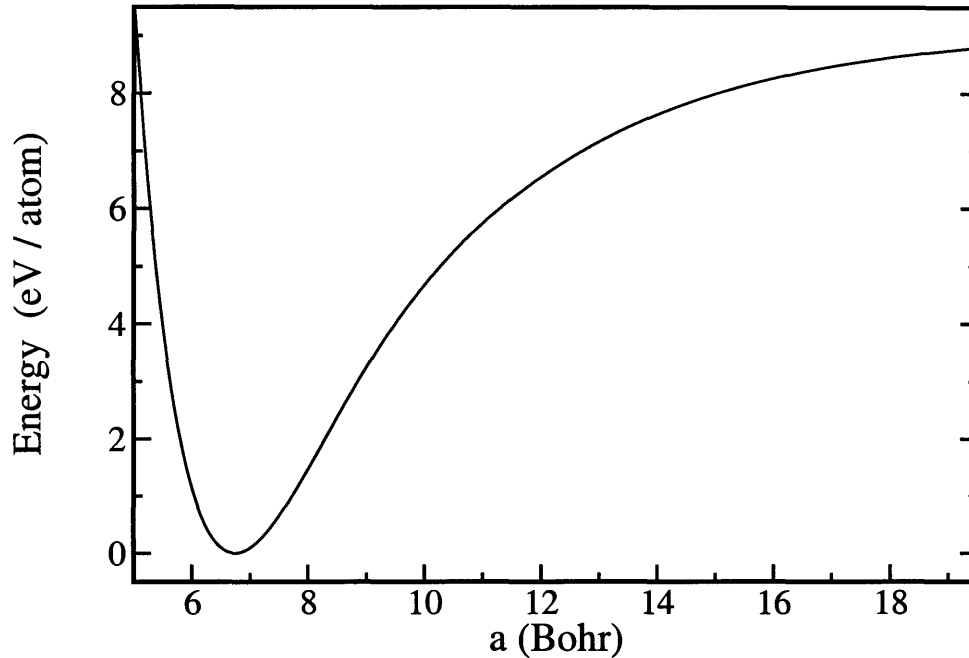
Figure 3-1: Ground state energy of diamond as a function of the lattice constant a. The zero of energy is set to the minimum.

would fit equally well the calculations around the minimum of the curve. A best fit of this equation on our data gives us both the equilibrium lattice parameter and the bulk modulus; our results are summarized in Table 3.1. The agreement with the experimental values is very good, even after the zero-point motion and thermal expansion are added to our theoretical predictions (see Chapter 4).

3.1.2 Graphene and graphite

The equation of state for graphene is shown in Fig. 3-2, fitted by a 4th order polynomial. The minimum is found for $a = 4.654$ a.u., which is very close to the experimental in-plane lattice parameter of graphite. The graphite equation of state is fitted by a two-dimensional 4th order polynomial in the variables a and c. To illustrate the very small dependence of the ground state energy with the c/a ratio, we plot the results of our calculations over a broad range of lattice constants in Figs. 3-3 and 3-4.

A few elastic constants can be obtained from the second derivatives of this energy [41]:

Table 3.1: Equilibrium lattice parameter a_0 and bulk modulus B_0 of diamond at the ground state (GS) and at 300 K (see Chapter 4), compared to experimental values.

	Present calculation	Experiment (300 K)
Lattice constant a_0 (a.u.)	6.743 (GS) 6.769 (300 K)	6.740 [a]
Bulk modulus B_0 (GPa)	432 (GS) 422 (300 K)	442 ± 2 [b]

[a]Ref. [70]
[b]Ref. [71]
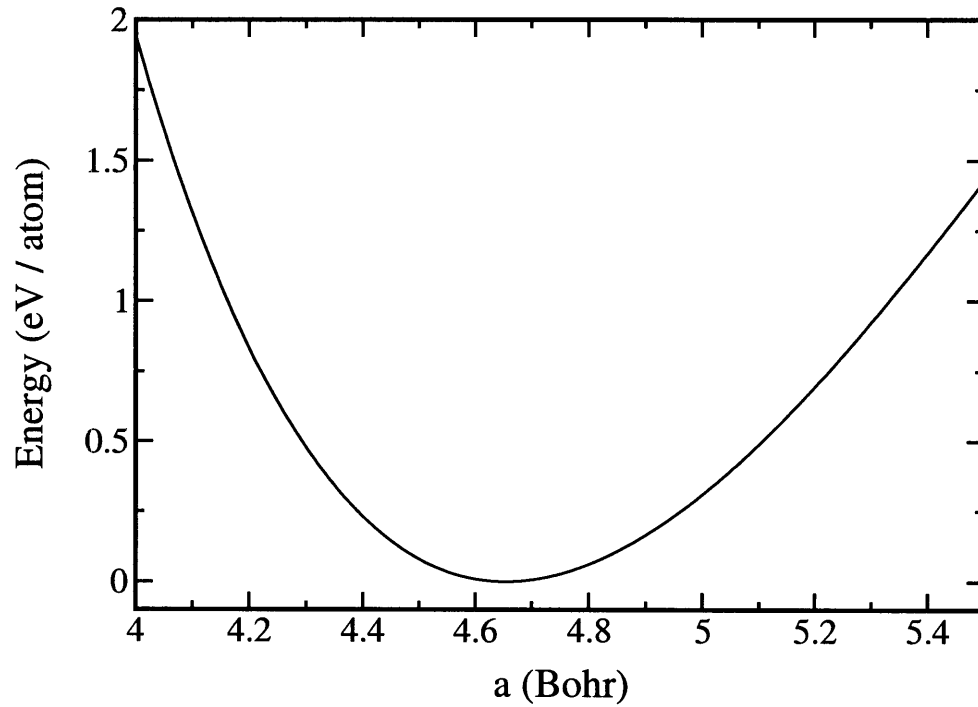
Figure 3-2: Ground state energy of graphene as a function of the lattice constant a. The zero of energy is set to the minimum.
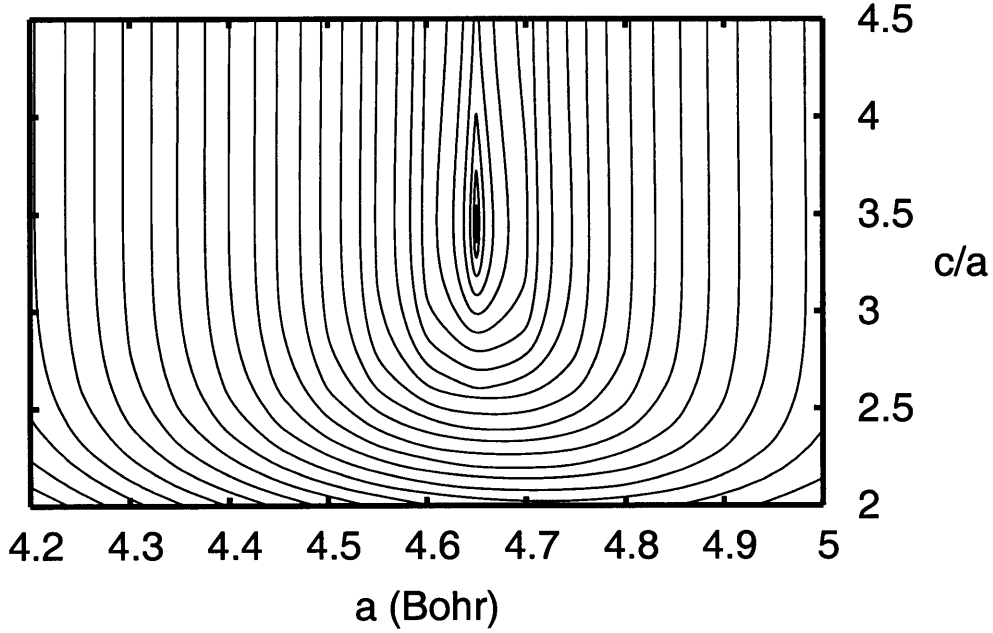
Figure 3-3: Contour plot of the ground state energy of graphite as a function of a and c/a (isoenergy contours are not equidistant).

$$\text{Stiffness coefficients}\begin{cases} C_{11} + C_{12} = \dfrac{a_0^2}{2V_0}\dfrac{\partial^2 E}{\partial a^2} \\[2ex] C_{33} = \dfrac{c_0^2}{V_0}\dfrac{\partial^2 E}{\partial c^2} \\[2ex] C_{13} = \dfrac{a_0 c_0}{2V_0}\dfrac{\partial^2 E}{\partial a \partial c} \end{cases} \qquad (3.2a)$$

$$\text{Tetragonal shear modulus} \quad C^t = \frac{1}{6}\left[(C_{11} + C_{12}) + 2C_{33} - 4C_{13}\right] \qquad (3.2b)$$

$$\text{Bulk modulus} \quad B_0 = \frac{C_{33}(C_{11} + C_{12}) - 2C_{13}^2}{6C^t} \qquad (3.2c)$$

where $V_0 = \frac{\sqrt{3}}{2}a_0^2 c_0$ is the volume of the unit cell.

We summarize all our LDA and GGA results in Table 3.2: For LDA, both the lattice parameter a_0 and the c_0/a_0 ratio are very close to experimental data. Elastic constants are calculated fully from first-principles, in the sense that the second

36
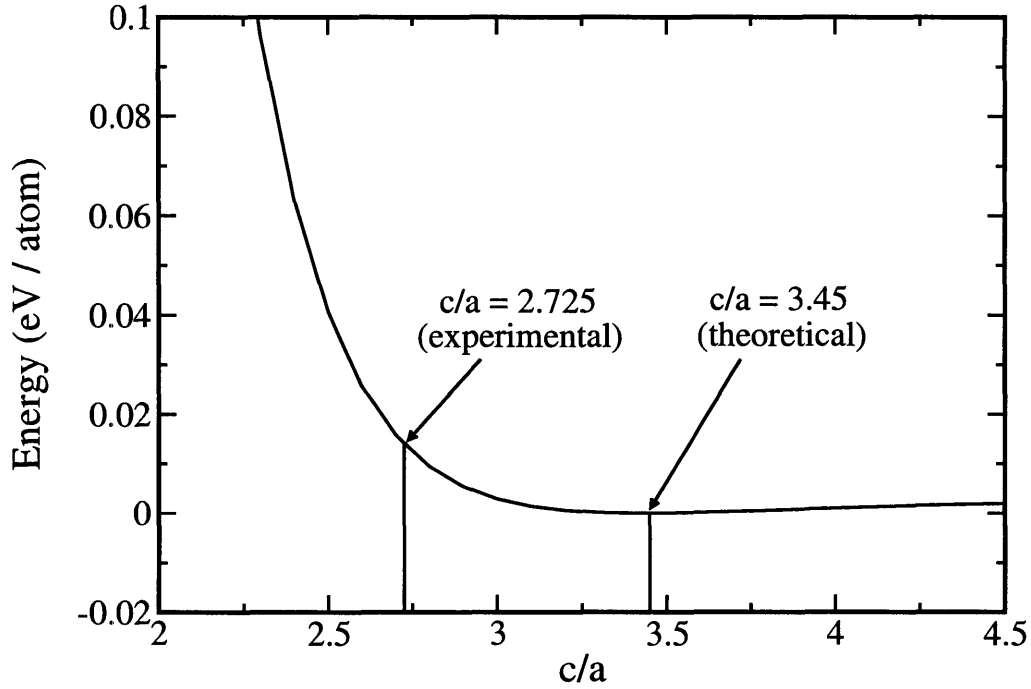
Figure 3-4: Ground state energy of graphite as a function of c/a at fixed $a = 4.65\,a.u.$. The theoretical (PBE) and the experimental c/a are shown. The zero of energy is set to the PBE minimum.

Table 3.2: Structural and elastic properties of graphite according to LDA, GGA, and experiments

	LDA fully theoretical	GGA fully theoretical	GGA using exp. c_0 in Eqs. (3.2a)	GGA with 2nd derivatives taken at exp. c_0/a_0	Experiment (300 K)
Lattice constant a_0(a.u.)	4.61	4.65	4.65	4.65(fixed)	4.65±0.003[1]
$\frac{c_0}{a_0}$ ratio	2.74	3.45	3.45	2.725(fixed)	2.725±0.001[1]
$C_{11} + C_{12}$ (GPa)	1283	976	1235	1230	1240±40[2]
C_{33} (GPa)	29	2.4	1.9	45	36.5±1 [2]
C_{13} (GPa)	-2.8	-0.46	-0.46	-4.6	15±5 [2]
B_0 (GPa)	27.8	2.4	1.9	41.2	35.8 [3]
C^t (GPa)	225	164	207	223	208.8 [3]

[a]Refs. [72, 73, 74], as reported by Ref. [41].
[b]Ref. [6]
[c]Ref. [75], as reported by Ref. [41]

derivatives of the energy are taken at the theoretical LDA a_0 and c_0, and that only these theoretical values are used in Eqs. (3.2a). Elastic constants are found in good agreement with experiments, except for the case of C_{13} which comes out as negative (meaning that the Poisson's coefficient would be negative).

Fully theoretical GGA results (second column of Table 3.2) compare poorly to experimental data except for the a_0 lattice constant, in very good agreement with experiments. Using the experimental value for c_0 in Eqs. (3.2a) improves only the value of $C_{11} + C_{12}$ (third column of Table 3.2). Most of the remaining disagreement is related to the poor value obtained for c/a; if the second derivatives in Eqs. (3.2a) are taken at the experimental value for c/a all elastic constants are accurately recovered except for C_{13} (fourth column of Table 3.2).

In both LDA and GGA, errors arise from the fact that Van Der Waals interactions between graphitic layers are poorly described. These issues can still be addressed within the framework of DFT (as shown by Langreth and collaborators, Ref. [52]) at the cost of having a non-local exchange-correlation potential.

3.1.3   Single-walled nanotubes

For achiral nanotubes we compute structural and elastic properties in two different ways. The first one consists in calculating the energy of a pristine SWNT for different values of the two parameters r and l, without performing any structural relaxation. This assumes that the atoms remain on a perfectly cylindrical shell, and that the only degrees of freedom that matter are the radius and the length. The parameters r and l play then exactly the same role as a and c for graphite (see Section 3.1.2 above) and after having fitted the equation of state by a two-dimensional 2nd order polynomial we obtain the stiffness coefficients using the same relations as for graphite (Eqs. 3.2), simply replacing a by r and c by l:

$$
\text{Stiffness coefficients} \left\{
\begin{array}{rcl}
C_{11} + C_{12} & = & \frac{r_0^2}{2V_0} \frac{\partial^2 E}{\partial r^2} \\\\
C_{33} & = & \frac{l_0^2}{V_0} \frac{\partial^2 E}{\partial l^2} \\\\
C_{13} & = & \frac{r_0 c_0}{2V_0} \frac{\partial^2 E}{\partial r \partial l}
\end{array}
\right.
\qquad (3.3\text{a})
$$

$$
\text{Tetragonal shear modulus} \quad C^t = \frac{1}{6} \left[(C_{11} + C_{12}) + 2C_{33} - 4C_{13} \right] \qquad (3.3\text{b})
$$

$$
\text{Bulk modulus} \quad B_0 = \frac{C_{33}(C_{11} + C_{12}) - 2C_{13}^2}{6C^t} \qquad (3.3\text{c})
$$

V_0 is defined here as the surface of the nanotube (equal to $2\pi r_0 l_0$) times the experimental interlayer spacing of graphite ($h = 6.34\,a.u.$), which plays the role of "wall thickness". This convention is the one followed by numerous studies on the elastic properties of nanotubes [76, 77, 78, 79] and facilitates comparison between different results on nanotubes or graphite.

Another approach consists in relaxing the whole structure for different fixed values of the unit cell height l: the energy is minimized with respect to all the degrees of freedom except l, i.e. versus all the atomic positions in the cell. This gives the total energy as a function of l. When fitting this energy by a 2nd order polynomial, the second derivative at the minimum l_0 gives us directly the Young's modulus in the axial direction Y:

$$
Y = \frac{l_0^2}{V_0} \left. \frac{d^2 E}{dl^2} \right|_{l_0} \qquad (3.4)
$$

where we take the same convention as above for V_0, r_0 being in this case the "average radius" of the SWNT, i.e. the average of the distance between each atom of the cell and the center axis of the nanotube, after relaxation.

The two methods are equivalent in the sense that l_0 is the same in each case, and the equilibrium value r_0 coming from the first approach is also the same as the average radius of the relaxed structure in the second method (in each case, the error
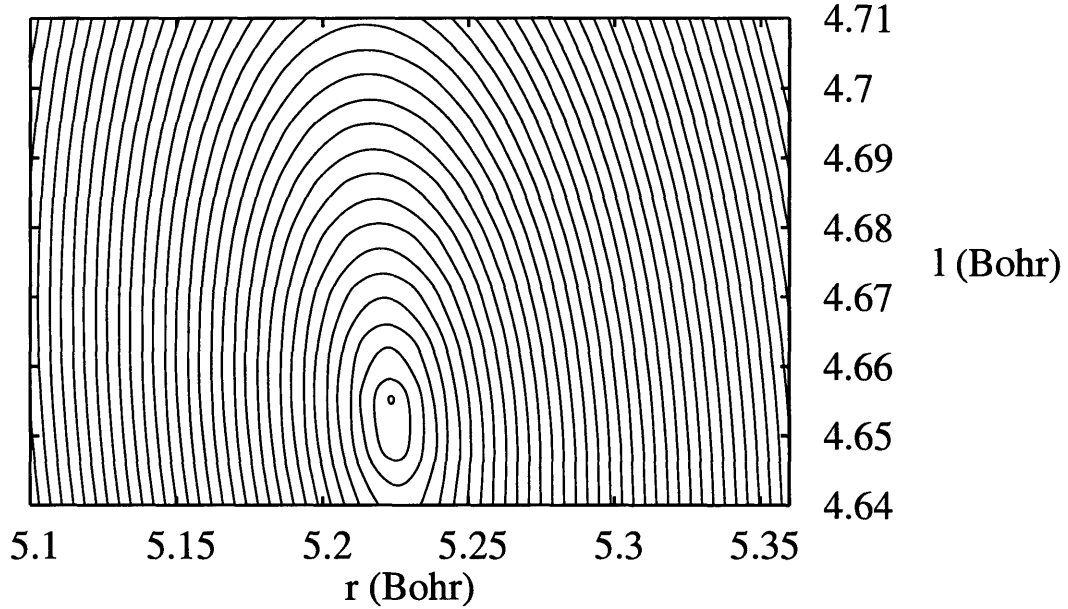
Figure 3-5: Contour plot of the ground state energy of an armchair (4,4) SWNT fitted by a second order polynomial of r and l (isoenergy contours are not equidistant).

is less than 0.01%). In Fig. 3-5 we show a contour plot of the energy of an armchair (5,5) SWNT versus both r and l (first method). In Fig. 3-6 we show the equation of state of an armchair (4,4) versus l, where the second method is used.

Results for structural properties and elastic constants are summarized in Table 3.3. We also include the quantity $\frac{d^2 E}{d\epsilon^2}$ which corresponds to the second derivative of the relaxed energy per atom (second method) versus axial strain. This quantity is directly proportional to the Young's modulus (the proportionality factor being V_0 over the number of atoms in the unit cell), and it does not depend on any arbitrary convention concerning the wall thickness.

The radii obtained are in very good agreement with theoretical values obtained in Refs. [76, 47, 79, 25], the difference being at most 1%. The height of the nanotube cell is also in excellent agreement with values obtained in Ref. [47]. The elastic constants depend on diameter only for very narrow SWNTs, where curvature reduces the C_{33} constant. Except for these narrow SWNTs, the elastic constants do not depend on
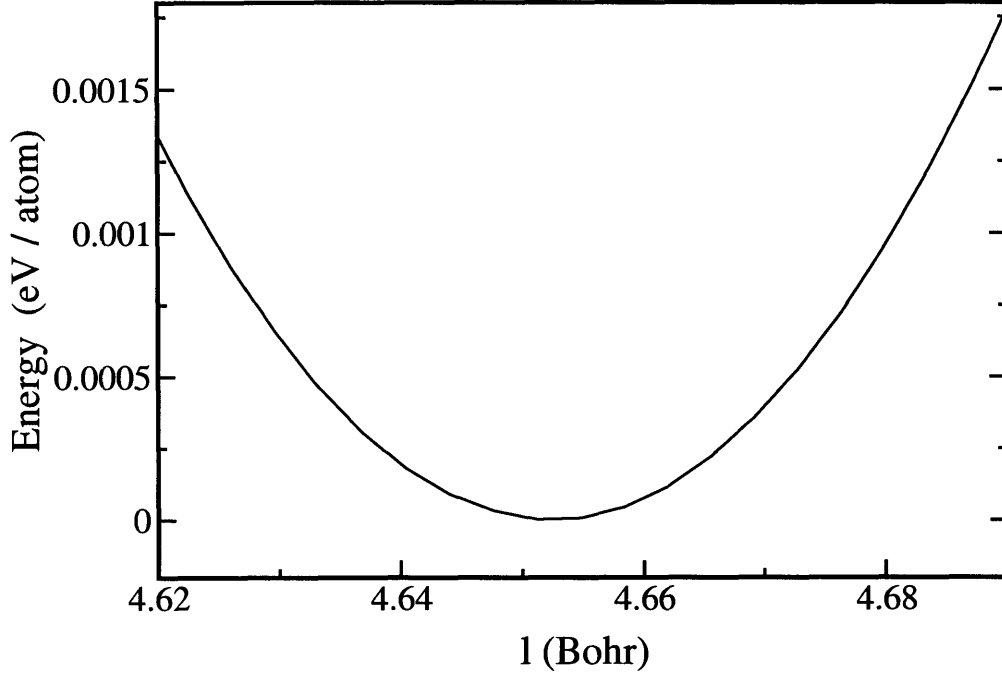
Figure 3-6: Ground state energy of a relaxed armchair (5,5) SWNT as a function of the unit cell length l. The zero of energy is set to the minimum.

diameters nor on chirality, as also pointed out in Refs. [14, 76, 25]. The C_{33} elastic constant is very similar to the in-plane C_{11} constant of graphite and the C_{11} constant of diamond (respectively 1060 and 1076 GPa, see Section 3.2 below). The values of Y and $\frac{d^2E}{d\epsilon^2}$ are in very good agreement with those obtained using ab-initio calculations in Refs. [25, 47], empirical potential calculations in Ref. [76], and similar to those calculated for long capped SWNTs using Hartree-Fock theory (Ref. [79]). Other elastic constants such as C_{33} and the bulk modulus B_0 agree well with the values of Ref. [76]. Finally, our results are in good agreement with the experimental value of the Young's modulus of SWNTs obtained as $1.25 - 0.35/ + 0.45$ TPa in Ref. [77] and 1 TPa in Ref. [78].

Table 3.3: Structural and elastic properties of several SWNTs: equilibrium radius r_0 and unit cell length l_0, stiffness coefficients $C_{11} + C_{12}$, C_{33} and C_{13}, bulk modulus B_0, Young's modulus Y, and second derivative of the strain energy with respect to the axial strain $\frac{d^2E}{d\epsilon^2}$

	r_0 (a.u)	l_0 (a.u.)	$C_{11} + C_{12}$ (GPa)	C_{33} (GPa)	C_{13} (GPa)	B_0 (GPa)	Y (GPa)	$\frac{d^2E}{d\epsilon^2}$ (eV/atom)
Armchair (3,3)	3.972	4.655	529	946	88.4	235		
Armchair (4,4)	5.224	4.653	502	980	78.2	223		
Armchair (5,5)	6.486	4.653	539	1009	81.7	238	982	54.6
Armchair (6,6)	7.757	4.653	532	1017	79.7	235		
Armchair (8,8)	10.307	4.653	526	1026	76.9	232		
Armchair (10,10)	12.863	4.653	522	1030	75.5	231	988	54.5
Zigzag (8,0)	6.010	8.052					986	55

3.2 Phonon dispersion curves

3.2.1 Diamond and graphite

We calculate the phonon dispersion relations for diamond, graphite, rhombohedral graphite and graphene. For diamond and graphene, we use the theoretical lattice parameter(s). For graphite, we either use the theoretical c/a or the experimental one ($c/a = 2.725$). We will comment extensively in the following on the role of c/a on our calculated properties. In rhombohedral graphite, we use the same in-plane lattice parameter and same interlayer distance as in graphite (that is, a c/a ratio multiplied by 1.5). Results are presented in Figs. 3-7, 3-8, 3-9, 3-10 and 3-11, together with the experimental data.

In Table 3.4 and 3.5 we summarize our results at high-symmetry points and compare them with experimental data. In diamond, GGA produces softer modes than LDA [20] on the whole (as expected), particularly at Γ (optical mode) and in the optical Γ-X branches. For these, the agreement is somehow better in LDA; on the other hand the whole Γ-L dispersion is overestimated by LDA.

The results on graphite require some comments. In Table 3.5 and Figs. 3-8, 3-9, 3-10 and 3-11, modes are classified as follow: L stands for longitudinal polarization, T for in-plane transversal polarization and Z for out-of-plane transversal polarization. For graphite, a prime (as in LO') indicates an optical mode where the two atoms in
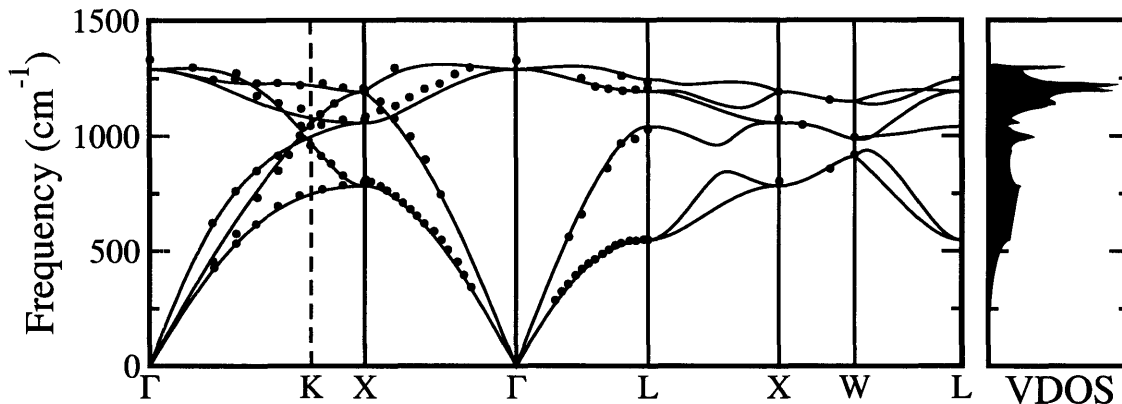
Figure 3-7: GGA ab-initio phonon dispersions (solid lines) and vibrational density of states (VDOS) for diamond. Experimental neutron scattering data from Ref. [18] are shown for comparison (circles).
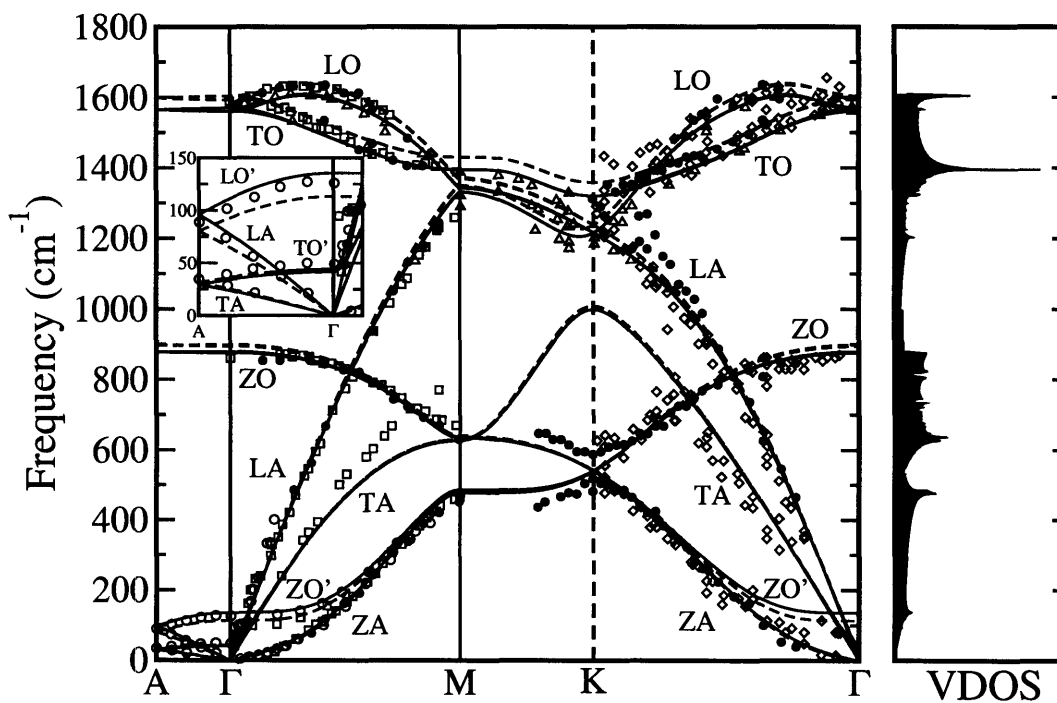
Figure 3-8: GGA (solid lines) and LDA (dashed line) ab-initio phonon dispersions for graphite, together with the GGA vibrational density of states (VDOS). The inset shows an enlargement of the low-frequency Γ-A region. The experimental data are EELS (Electron Energy Loss Spectroscopy) from Refs. [80], [81] and [82] (respectively squares, diamonds, and filled circles), neutron scattering from Ref. [83] (open circles), and x-ray scattering from Ref. [21] (triangles). Data for Refs. [80] and [82] were taken from Ref. [22].
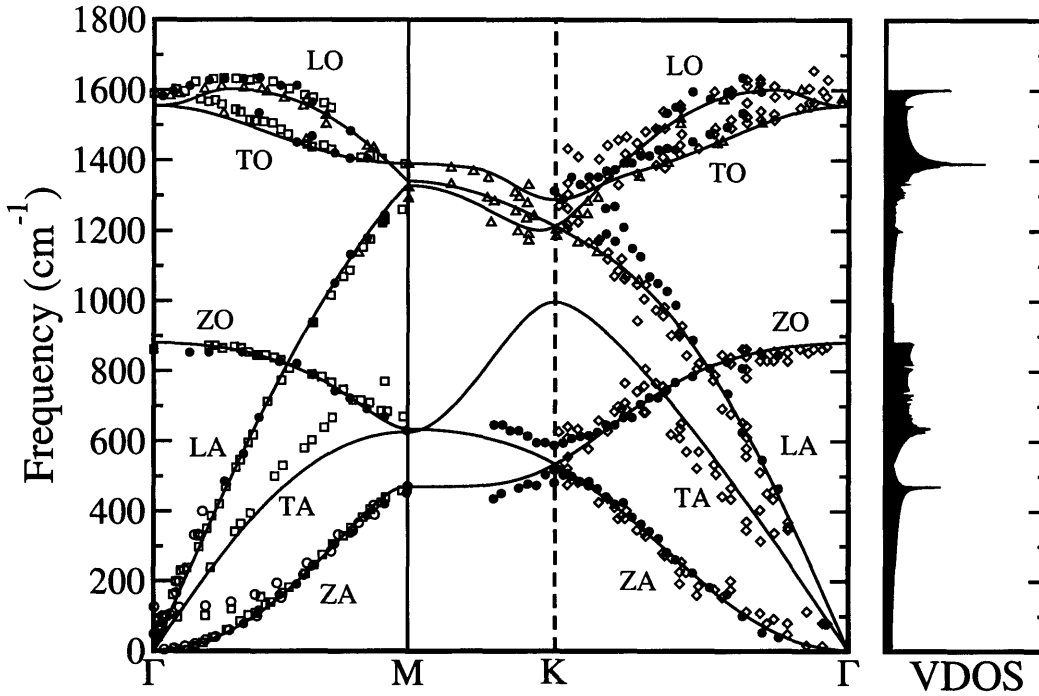
Figure 3-9: GGA ab-initio phonon dispersions for graphene (solid lines). Experimental data for graphite are also shown, as in Fig. 3-8.
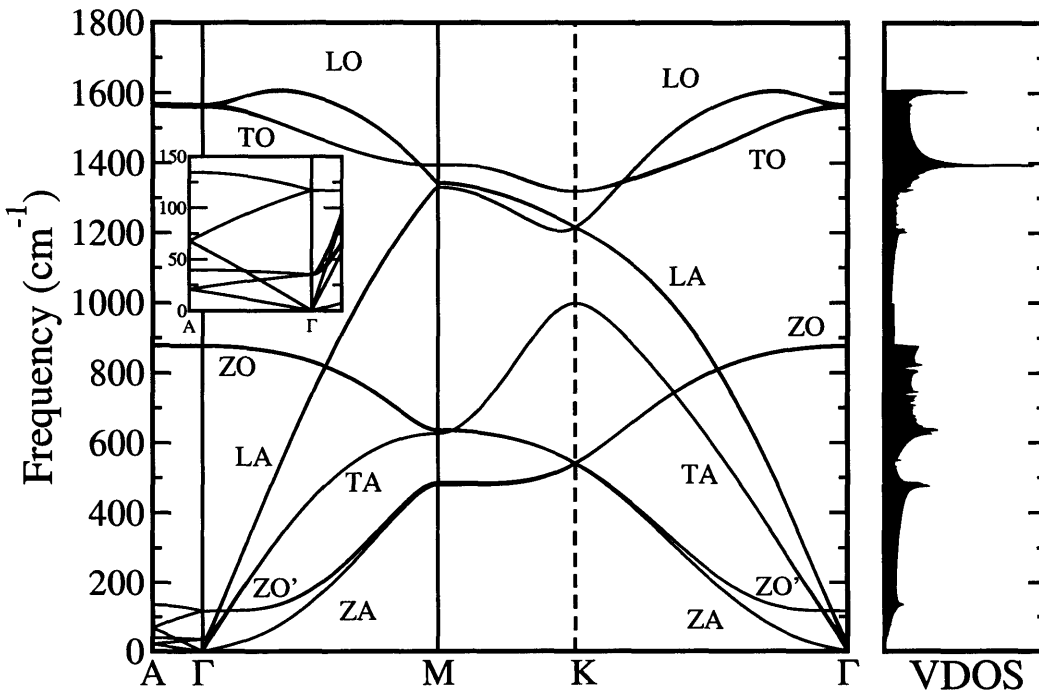
Figure 3-10: GGA ab-initio phonon dispersions for rhombohedral graphite. The inset shows an enlargement of the low-frequency Γ-A region.
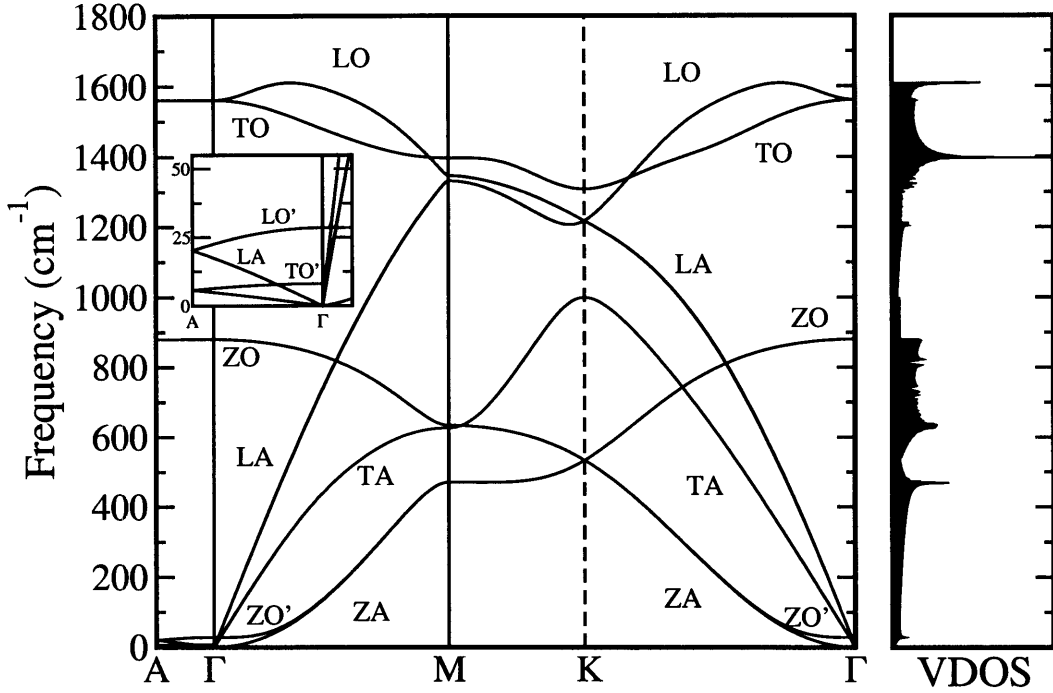
Figure 3-11: GGA ab-initio phonon dispersions for graphite at the theoretical c/a. The inset shows an enlargement of the low-frequency Γ-A region.

Table 3.4: Phonon frequencies of diamond at the high-symmetry points Γ, X and L, in cm^{-1}.

	Γ_O	X_{TA}	X_{TO}	X_{LO}	L_{TA}	L_{LA}	L_{TO}	L_{LO}
LDA[a]	1324	800	1094	1228	561	1080	1231	1275
GGA[b]	1289	783	1057	1192	548	1040	1193	1246
Exp.[c]	1332	807	1072	1184	550	1029	1206	1234

[a]Ref. [20]
[b]Present calculation
[c]Ref. [18]

Table 3.5: Phonon frequencies of graphite and derivatives at the high-symmetry points A, Γ, M and K, in cm^{-1}. The lattice constants used in the calculations are also shown.

	Graphite			Rhombo. graphite	Graphene	Graphite
Functional	LDA	GGA	GGA	GGA	GGA	Experiment
In-plane lattice ct. a_0	4.61 a.u.	4.65 a.u.	4.65 a.u.	4.65 a.u.	4.65 a.u.	4.65 a.u.
Interlayer distance/a_0	1.36	1.725	1.36	1.36	15	1.36
$A_{TA/TO'}$	31	6	29			35[1]
$A_{LA/LO'}$	80	20	96			89[1]
A_{LO}	897	880	878			
A_{TO}	1598	1561	1564			
$\Gamma_{LO'}$	44	8	41	35		49[1]
$\Gamma_{ZO'}$	113	28	135	117		95[2], 126[1]
Γ_{ZO}	899	881	879	879	881	861[2]
$\Gamma_{LO/TO}$	1593	1561	1559	1559	1554	1590[2], 1575[6]
	1604	1561	1567			
M_{ZA}	478	471	477	479	471	471[1], 465[2], 451[4]
M_{TA}	630	626	626	626	626	630[4]
M_{ZO}	637	634	634	635	635	670[2]
M_{LA}	1349	1331	1330	1330	1328	1290[3]
M_{LO}	1368	1346	1342	1344	1340	1321[3]
M_{TO}	1430	1397	1394	1394	1390	1388[3], 1389[2]
K_{ZA}	540	534	540	535	535	482[4], 517[4], 530[5]
K_{ZO}	544	534	542	539	535	588[4], 627[5]
K_{TA}	1009	999	998	998	997	
$K_{LA/LO}$	1239	1218	1216	1216	1213	1184[3], 1202[3]
K_{TO}	1359	1308	1319[7]	1319	1288[7]	1313[4], 1291[5]

[a]Ref. [83]

[b]Ref. [80]

[c]Ref. [21]

[d]Ref. [82]

[e]Ref. [81]

[f]Ref. [84]

[g]Note that a direct calculation of this mode with DFPT (instead of the Fourier interpolation result given here) leads to a significantly lower value in the case of graphite — 1297 cm^{-1} instead of 1319 cm^{-1}. This explains much of the discrepancy between the graphite and graphene result, since in the latter we used a denser q-points mesh. This effect is due to the Kohn anomaly occurring at K [46].

each layer of the unit cell oscillate together and in phase opposition to the two atoms of the other layer. A non-primed optical mode is instead a mode where atoms inside the same layer are "optical" with respect to each other. Of course "primed" optical modes do not exist for graphene, since there is only one layer (two atoms) per unit cell.

We observe that stacking has a negligible effect on all the frequencies above 400 cm^{-1}, since both rhombohedral graphite and hexagonal graphite show nearly the same dispersions except for the Γ-A branch and the in-plane dispersions near Γ. The in-plane part of the dispersions is also very similar to that of graphene, except of course for the low optical branches (below 400 cm^{-1}) that appear in graphite and are not present in graphene.

For graphite as well as diamond GGA tends to underestimate high optical modes while LDA overestimates them. The opposite happens for the low optical modes, and for the Γ-A branch of graphite; the acoustic modes show marginal differences and are in very good agreement with experiments. Overall, the agreement of both LDA and GGA calculations with experiments is very good and comparable to that between different measurements.

Some characteristic features of both diamond and graphite are well reproduced by our ab-initio results, such as the LO branch overbending and the associated shift of the highest frequencies away from Γ. Also, in the case of graphite, rhombohedral graphite and graphene, the quadratic dispersion of the in-plane ZA branch in the vicinity of Γ is observed; this is a characteristic feature of the phonon dispersions of layered crystals [85, 86], observed experimentally e.g. with neutron scattering [83]. Nevertheless, some discrepancies are found in graphite. The most obvious one is along the Γ-M TA branch, where EELS [80] data show much higher frequencies than calculations. Additionally, several EELS experiments [81, 82] report a gap between the ZA and ZO branches at K while these cross each other in all the calculations. In these cases the disagreement could come either from a failure of DFT within the approximations used or from imperfections in the crystals used in the experiments. There are also discrepancies between experimental data, in particular in graphite for

the LA branch around K: EELS data from Ref. [81] agree with our ab-initio results while those from Ref. [82] deviate from them.

Finally, we should stress again the dependence of the graphite phonon frequencies on the in-plane lattice parameter and c/a ratio. The results we have analyzed so far were obtained using the theoretical in-plane lattice parameter a and the experimental c/a ratio for both GGA and LDA. Since the LDA theoretical c/a is very close to the experimental one (2.74 vs. 2.725) and the interlayer bonding is very weak, these differences do no matter. However this is not the case for GGA, as the theoretical c/a ratio is very different from the experimental one (3.45 vs. 2.725). Fig. 3-11 and the second column of Table 3.5 show results of GGA calculations performed at the theoretical c/a. Low frequencies (below 150 cm^{-1}) between Γ and A are strongly underestimated, as are the ZO$'$ modes between Γ and M, while the remaining branches are barely affected.

The high-frequency optical modes are instead strongly dependent on the in-plane lattice constant. The difference between the values of a in LDA and GGA explains much of the discrepancy between the LDA optical modes and the GGA ones. Indeed, a LDA calculation performed at $a = 4.65$ a.u. and $c/a = 2.725$ (not shown here) brings the phonon frequencies of these modes very close to the GGA ones obtained with the same parameters, while lower-energy modes (below 1000 cm^{-1}) are hardly affected.

Our final choice to use the theoretical in-plane lattice parameter and the experimental c/a seems to strike a balance between the need of theoretical consistency and that of accuracy. Therefore, the remaining of this chapter is based on calculations performed using the parameters discussed above ($a = 4.61$ for LDA, $a = 4.65$ for GGA and $c/a = 2.725$ in each case).

Elastic constants can be extracted from the data on sound velocities. Indeed, the latter are the slopes of the dispersion curves in the vicinity of Γ and can be expressed as the square root of linear combinations of elastic constants (depending on the branch considered) over the density (see Ref. [87] for details). We note in passing that we compute the density consistently with the geometry used in the calculations (see

Table 3.6: Elastic constants of diamond and graphite as calculated from the phonon dispersions, in GPa.

| Functional | Diamond | | | Graphite | | |
	GGA	Exp.	LDA	GGA	Exp.	
C_{11}	1060	1076.4 ± 0.2[2]	1118	1079	1060 ± 20[1]	
C_{12}	125	125.2 ± 2.3[2]	235	217	180 ± 20[1]	
C_{44}	562	577.4 ± 1.4[2]	4.5	3.9	4.5 ± 0.5[1]	
C_{33}	-	-	29.5	42.2	36.5 ± 1 [1]	

[a]Ref. [6]
[b]Ref. [71]

Table 3.5 for details, first column for LDA and third one for GGA), and not the experimental density. Our results are shown in Table 3.6.

The overall agreement with experiment is good to very good. LDA leads to larger elastic constants, as expected from the general tendency to "overbind", but still agrees well with experiment. For diamond, the agreement is particularly good. As for C_{13} in graphite, it is quite difficult to obtain it from the dispersion curves since it enters the sound velocities only in a linear combination involving other elastic constants, for which the error is almost comparable to the magnitude of C_{13} itself.

3.2.2 Armchair and zigzag nanotubes

Phonon dispersions of both armchair (5,5) and zigzag (8,0) are computed. We use structures that have been fully relaxed, that is, the energy minimized versus all degrees of freedom, including the unit cell length l (see Section 3.1.3). Results are presented in Figs. 3-12 and 3-13.

To achieve higher accuracy in the dispersions, we use a $1 \times 1 \times 8$ q-point sampling for the zigzag nanotube and $1 \times 1 \times 16$ for the armchair one. Also, the k-point grid used for armchair is denser than the standard set in Section 2.4, i.e. $1 \times 1 \times 16$ instead of $1 \times 1 \times 12$. In the case of armchair tubes this is needed because Kohn anomalies arise in the phonon dispersions [68, 46, 27]. Even with such dense grids, a few high optical frequencies at Γ might not be fully converged in our armchair (5,5) calculations. The

49
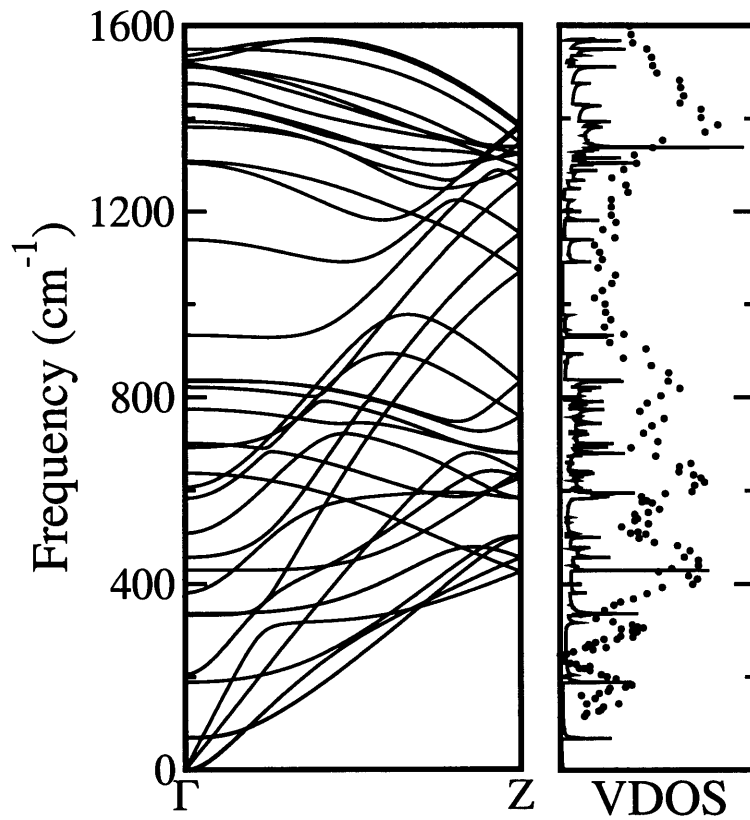
Figure 3-12: GGA ab-initio phonon dispersions and vibrational density of states (VDOS) for an armchair (5,5) SWNT. VDOS from experimental inelastic neutron scattering data (Ref. [26]) is shown for comparison (circles).
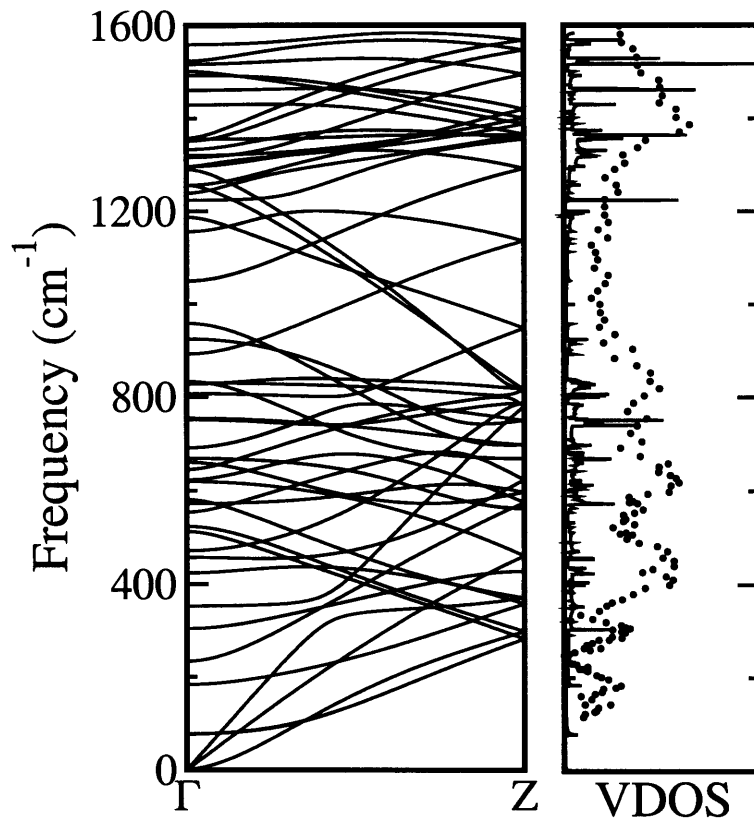
Figure 3-13: GGA ab-initio phonon dispersions and vibrational density of states (VDOS) for a zigzag (8,0) SWNT. VDOS from experimental inelastic neutron scattering data (Ref. [26]) is shown for comparison (circles).

translational and rotational acoustic sum rules are applied to the interatomic force constants before drawing the dispersion curves, following the methodology explained in Appendix A.

As in diamond and graphite, the dispersions exhibit an overbending of the highest optical frequencies, which is more visible for the armchair tube than for the zigzag one. The lowest and doubly-degenerate acoustic modes (called TA bending modes) have a parabolic shape near Γ, in analogy to layered materials, as was inferred in Refs. [86, 88] and explained for the case of SWNTs in Ref. [89]. An additional acoustic branch, the "twisting" mode, appears in the vicinity of Γ, corresponding to a twist of the nanotubes about their axis.

Our dispersions are in good qualitative agreement with other ab-initio calculations on (10,0) and (10,10) SWNTs (Ref. [23]), on (4,4) and (10,10) SWNTs (Ref. [25]) and on a (3,3) SWNT (Ref. [27]). All these results disagree with the ab-initio calculations on (5,5), (6,6) and (10,10) SWNTs of Ref. [24], where the overbending is not present. Our vibrational density of states (VDOS) exhibits significant discrepancies with respect to the experimental VDOS obtained from inelastic neutron scattering data [26]. This is at least partly due to the fact that SWNTs of different diameters and chirality were present in the experimental sample, which broadens and shifts the VDOS peaks compared to the defined-chirality SWNTs of our calculations.

An accurate description of the phonon dispersions of all these materials allows us to predict the low-energy structural excitations and thus several thermodynamic quantities. Before exploring this in Chapter 4, we want to discuss the nature and decay of the interatomic force constants in carbon based materials.

3.3 Interatomic force constants

As explained in Section 2.2, the interatomic force constants $C_{i,j}(\mathbf{R} - \mathbf{R}')$ are obtained in our calculations from the Fourier transform of the dynamical matrix $\tilde{D}_{i,j}(\mathbf{q})$ calculated on a regular mesh inside the Brillouin zone ($8 \times 8 \times 8$ for diamond, $8 \times 8 \times 4$ for graphite, $16 \times 16 \times 1$ for graphene, $1 \times 1 \times 8$ for zigzag (8,0) and $1 \times 1 \times 16$ for
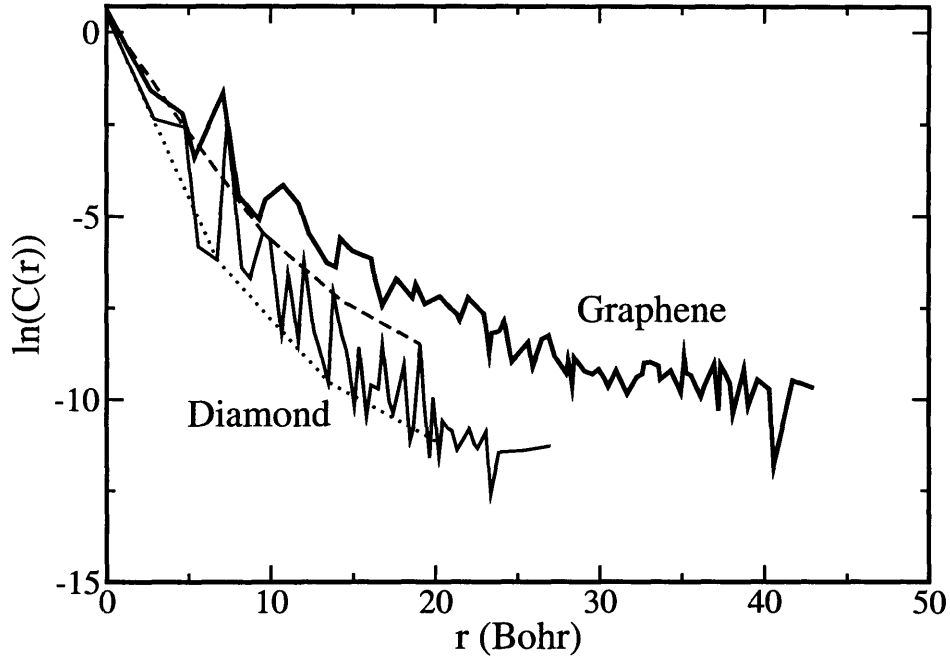
Figure 3-14: Decay of the norm of the interatomic force constants as a function of distance for diamond (thin solid line) and graphene (thick solid line), in a semi-logarithmic scale. The dotted and dashed lines show the decay for diamond along the (100) and (110) directions.

armchair (5,5)). This procedure is exactly equivalent (but much more efficient) than calculating the interatomic force constants with frozen phonons (up to 47 neighbors in diamond, 74 in graphene, etc.). At a given $\mathbf{R}$, $C_{i,j}(\mathbf{R})$ is actually a 2nd order tensor, and the decay of its norm (defined as the square root of the sum of the squares of all the matrix elements) with distance is a good measure to gauge the effect of distant neighbors. In Fig. 3-14 we plot the natural logarithm of such a norm with respect to the distance from a given atom, for diamond and graphene. The norm is averaged on all the neighbors located at the same distance before taking the logarithm.

The force-constants decay in graphene is slower than in diamond, and it depends much less on direction. In diamond decay along (110) is much slower than in other directions due to long-range elastic effects along the covalent bonds. This long-range decay is also responsible for the flattening of the phonon dispersions in zincblende and diamond semiconductors along the K-X line (see Fig. 3-7 and Ref. [36], for instance).

In Fig. 3-15 we show the decay plot for graphite and graphene, averaged over all

53
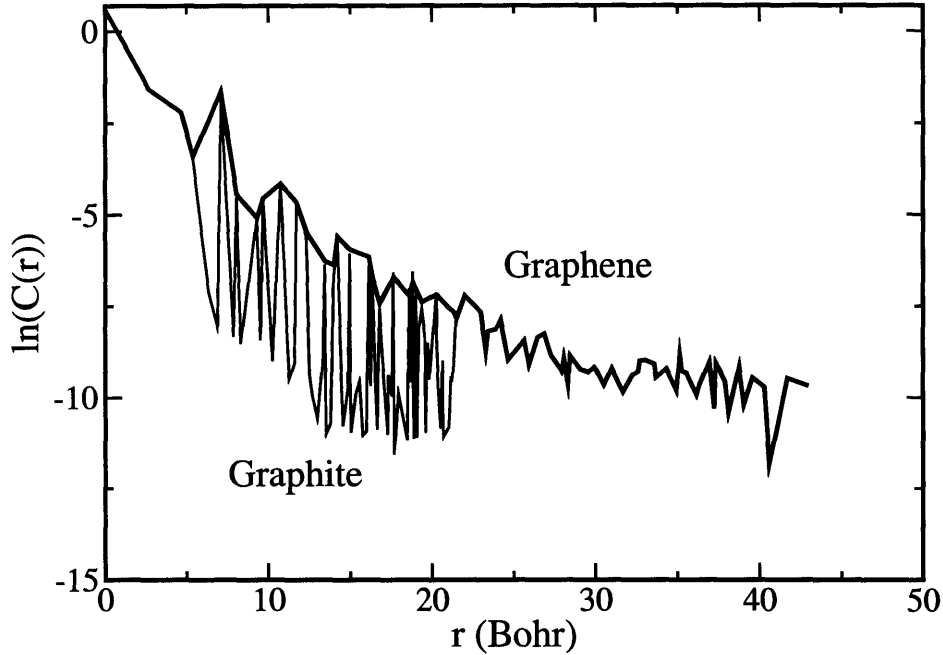
Figure 3-15: Decay of the norm of the interatomic force constants as a function of distance for graphite (thin solid line) and graphene (thick solid line).

directions. The graphite interatomic force constants include values corresponding to graphene (in-plane nearest neighbors) and smaller values corresponding to the weak interlayer interactions.

Finally, in Fig. 3-16 we show the decay for the interatomic force constants in armchair (5,5) and zigzag (8,0) SWNTs, compared to the ones for graphene. The three curves have the same trend, showing the great similarity between the force constants of graphene and those of SWNTs.

It is interesting to assess the effect of truncation of these interatomic force constants on the phonon dispersions. This can be done by replacing the force constants corresponding to distant neighbors by zero. In this way short-range and long-range contributions can be examined. The former are relevant for short-range force-constant models such as the VFF (Valence Force Field) [15] or the 4NNFC (4th Nearest-Neighbor Force Constant) [90] used e.g. in graphene. Note however that a simple truncation is not comparable to the VFF or 4NNFC models, where effective interatomic force constants would be renormalized.
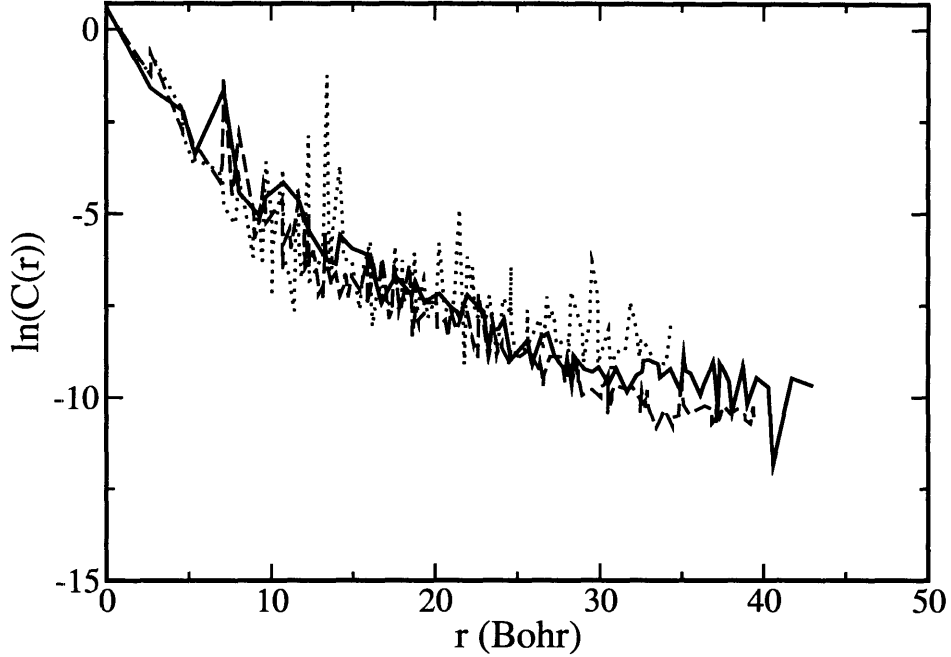
Figure 3-16: Decay of the norm of the interatomic force constants as a function of distance for graphene (solid line), armchair (5,5) SWNT (dashed line) and zigzag (8,0) SWNT (dotted line).

Figs. 3-17 and 3-18 show the change in frequency for selected modes in diamond and graphene as a function of the truncation range. The modes we chose are those most strongly affected by the number of neighbors included.

For diamond, our whole supercell contains up to 47 neighbors, and the graph shows only the region up to 20 neighbors included, since the selected modes do not vary by more than $1\,\mathrm{cm}^{-1}$ after that. With 5 neighbors, phonon frequencies are already near their converged value, being off by at worst 4%; very good accuracy ($5\,\mathrm{cm}^{-1}$) is obtained with 13 neighbors.

For graphene, our $16 \times 16 \times 1$ supercell contains up to 74 neighbors, but after the 30th no relevant changes occur. At least 4 neighbors are needed for the optical modes to be converged within 5-8%. Some acoustic modes require more neighbors, as also pointed out in Ref. [23]. As can be seen in Fig. 3-18, the frequency of some ZA modes in the Γ-M branch (at about one fourth of the branch) oscillates strongly with the number of neighbors included, and can even become imaginary when less than 13 are used, resulting into an instability of the crystal. This behavior does not appear in
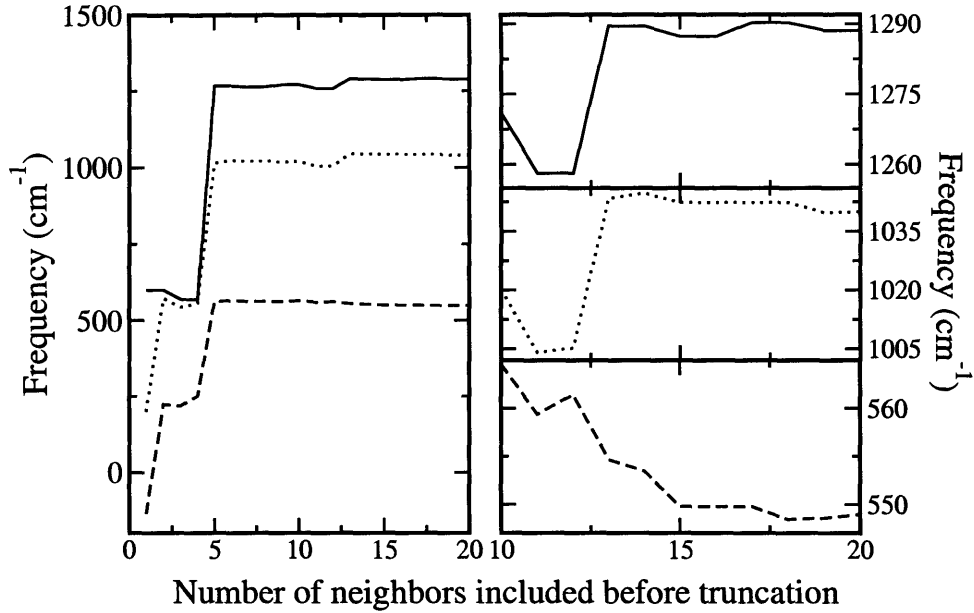
Figure 3-17: Phonon frequencies of diamond as a function of the number of neighbors included in the interatomic force constants: Γ_O (solid line), X_{TO} (dotted line), and L_{TA} (dashed line).

diamond. Also, the K_{TO} mode keeps varying in going down from 20 to 30 neighbors, though this effect remains small (8 − 9 cm^{-1}). This drift signals the presence of a Kohn anomaly [68]. Indeed, at the K point of the Brillouin zone the electronic band gap vanishes in graphene, so that a singularity arises in the highest optical phonon mode. Therefore a finer q-point mesh is needed around this point, and longer-ranged interatomic force constants. This effect is discussed in detail in Ref. [46].
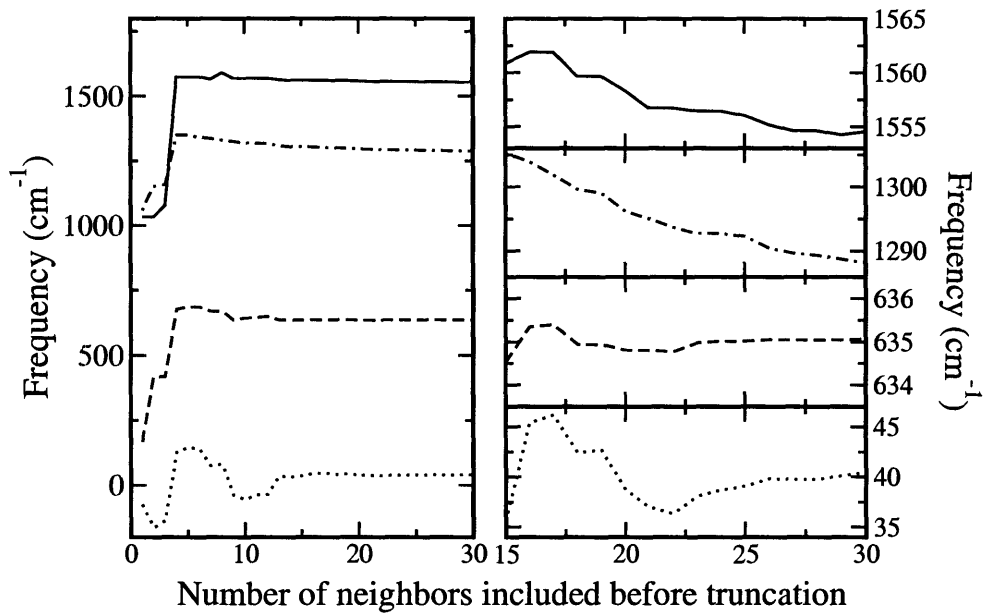
Figure 3-18: Phonon frequencies of graphene as a function of the number of neighbors included in the interatomic force constants: $\Gamma_{LO/TO}$ (solid line), K_{TO} (dot-dashed), M_{ZO} (dashed), and for the dotted line a phonon mode in the ZA branch one-fourth along the Γ to M line.

Chapter 4

Thermodynamic properties

We present in this chapter our results on the thermodynamic properties of diamond, graphite, graphene and SWNTs using the quasi-harmonic approximation and phonon dispersions at the GGA level. As outlined in Section 2.3 we first perform a direct minimization over the lattice parameter(s) $\{a_i\}$ of the vibrational free energy $F(\{a_i\}, T)$ (Eq. 2.8). This gives us, for any temperature T, the equilibrium structure, shown in Figs. 4-1, 4-2, 4-3, 4-4 and 4-5. For diamond, graphene and SWNTs we use in Eq. (2.8) the equations of state obtained from the ground state calculations presented in Section 3.1. For graphite this choice would not be useful or accurate, since the theoretical c/a is much larger than the experimental one. So we *force* the equation of state to be a minimum for c/a=2.725 and a=4.65 a.u. (fixing only c/a and relaxing a would give a=4.66 a.u., with negligible effects on the thermal expansion). In particular, our "corrected" equation of state is obtained by fitting with a fourth order polynomial the true equation of state around the experimental a and c/a, and then dropping from this polynomial the linear order terms. Since the second derivatives of the polynomial remain unchanged, we keep the elastic constants unchanged, and the only input from experiments remains the c/a ratio. We have also checked the effects of imposing to C_{13} its experimental value (C_{13} is the elastic constant that is predicted least accurately), but the changes were small.

The dependence of the phonon frequencies on the lattice parameters is determined by calculating the whole phonon dispersions at several values and interpolating these
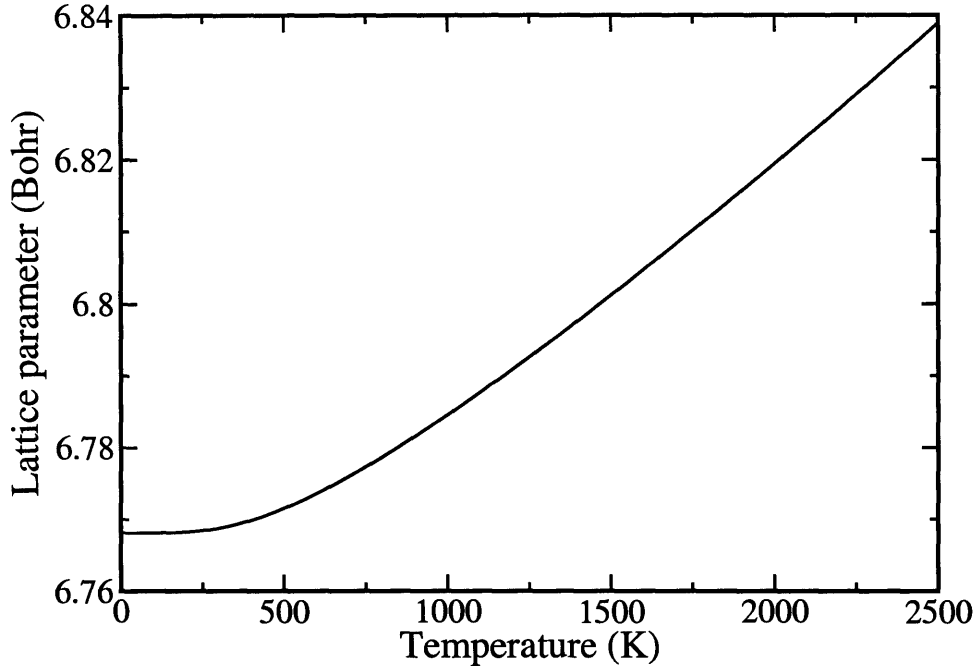
Figure 4-1: Lattice parameter of diamond as a function of temperature

in between. For diamond and graphene we use four different values of a (from 6.76 a.u. to 6.85 a.u. for diamond, and from 4.654 a.u. to 4.668 a.u. for graphene) and interpolate them with a cubic polynomial. For graphite, where two independent structural parameters are needed, we restrict ourselves to linear interpolations and calculate the phonon dispersions for the three combinations of $(a, c/a)$=(4.659,2.725), (4.659,2.9) and (4.667,2.725). We also use linear interpolation for SWNTs and compute the phonon dispersions of fully relaxed structures (see Section 3.1.3) for two different values of l: the equilibrium one and a value 1% higher. The dispersions are computed with the same q-point grids detailed in Section 3.2.

Before focusing on the thermal expansion, we examine zero-point motion. Indeed, the effects of temperature up to about 1000 K remains small or comparable to the zero-point expansion of the lattice parameters. In diamond, once the zero-point motion is added the equilibrium lattice parameter a expands from 6.743 a.u. to 6.768 a.u., a difference of 0.4%. For graphene, a changes from 4.654 a.u. to 4.668 a.u. with zero-point motion corrections (+0.3%); for graphite a increases from 4.65 to 4.664 a.u. (+0.3%) and c from 12.671 to 12.711 (+0.3%); for armchair (5,5) nanotubes, l goes
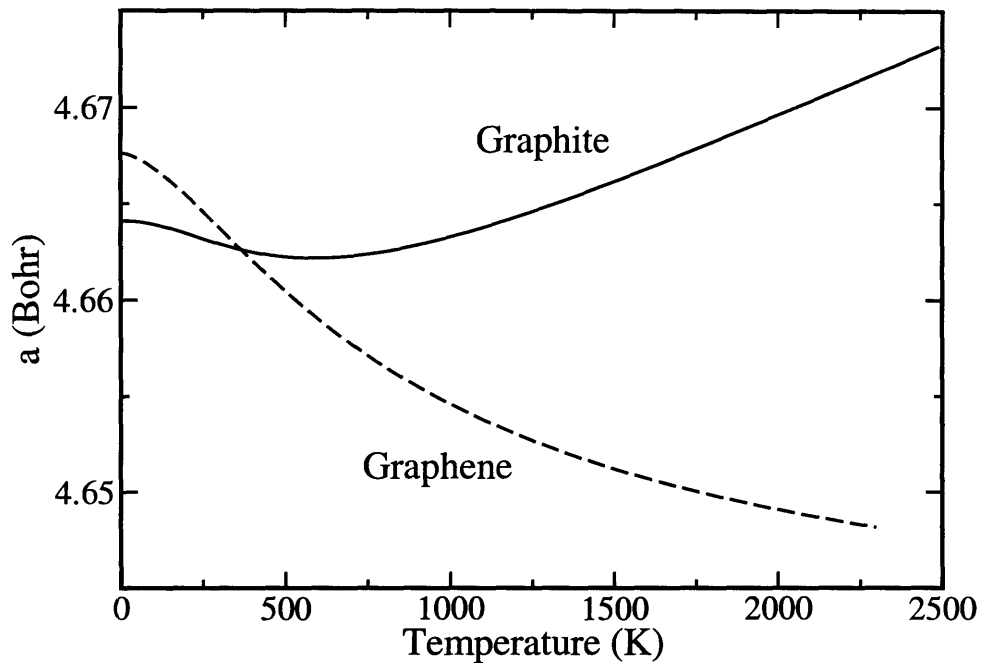
Figure 4-2: In-plane lattice parameter of graphite (solid line) and graphene (dashed line) as a function of temperature
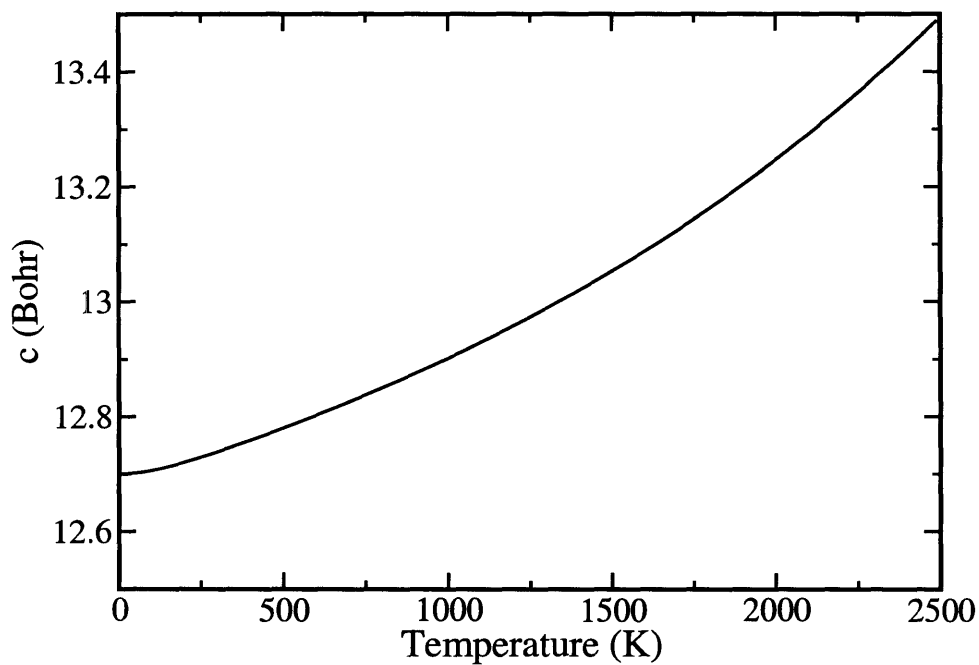
Figure 4-3: Out-of-plane lattice parameter of graphite as a function of temperature
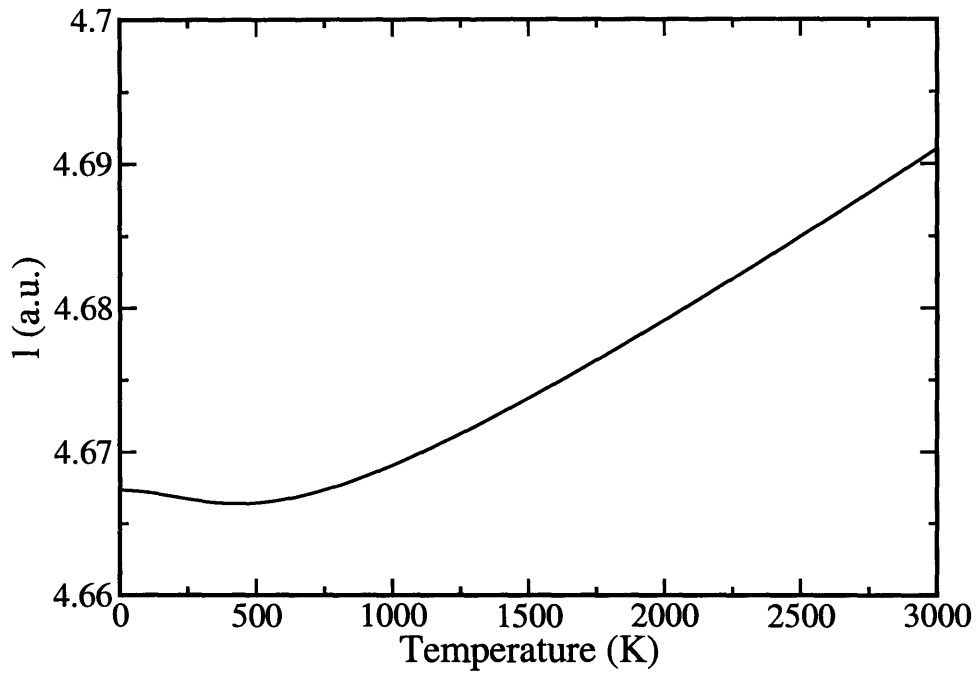
Figure 4-4: Axial lattice parameter of an armchair (5,5) SWNT as a function of temperature
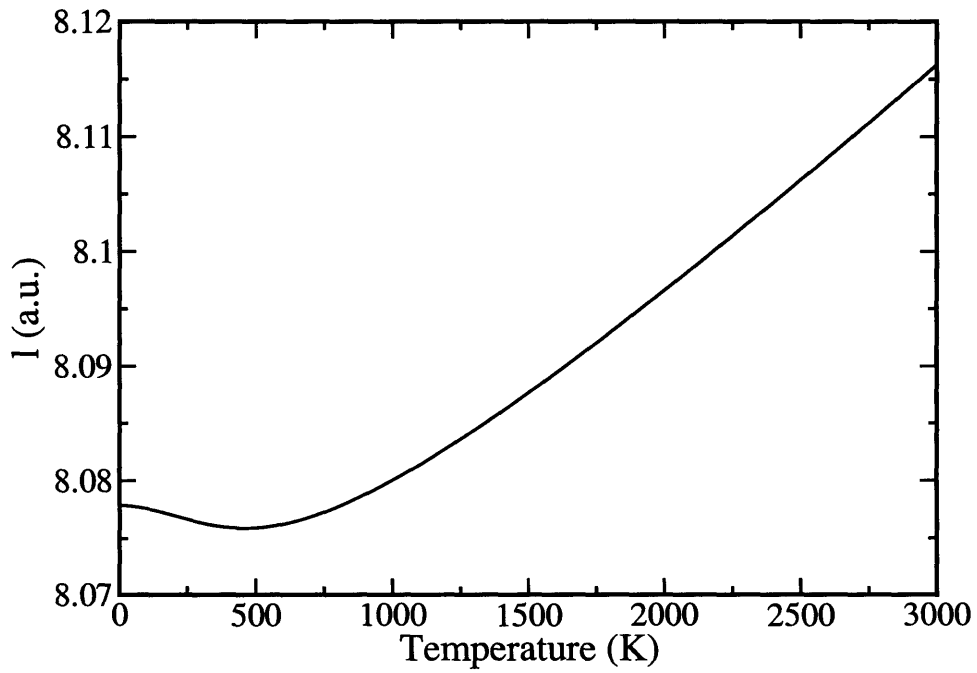
Figure 4-5: Axial lattice parameter of a zigzag (8,0) SWNT as a function of temperature
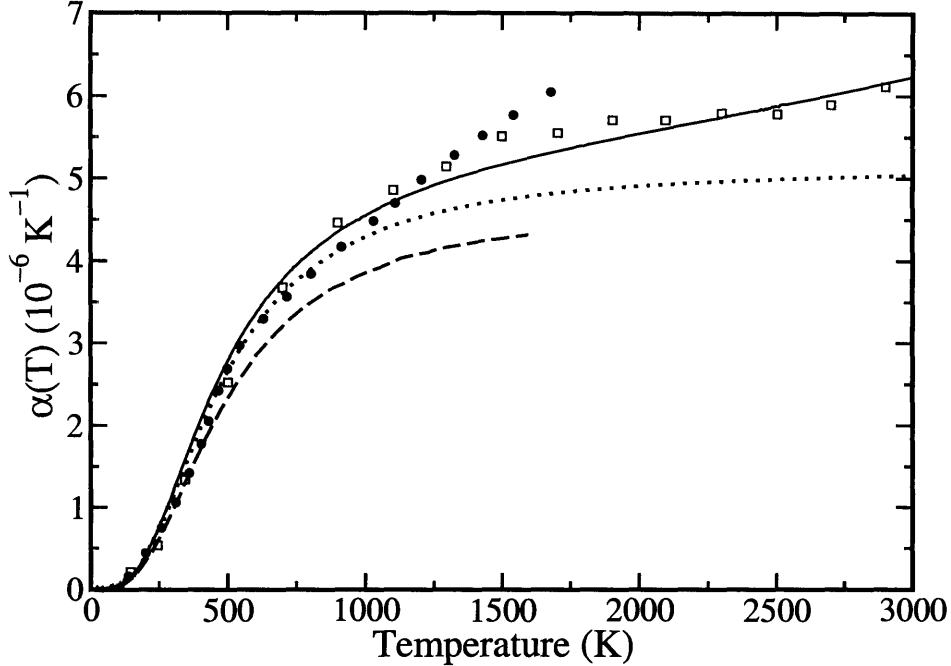
Figure 4-6: Coefficient of linear thermal expansion for diamond as a function of temperature. We compare our QHA-GGA ab-initio calculations (solid line) to experiments (Ref. [19], filled circles), a path integral Monte-Carlo study using a Tersoff empirical potential (Ref. [91], open squares) and the QHA-LDA study by Pavone *et al* [20] (dashed line). The QHA-GGA thermal expansion calculated using the Grüneisen equation (Eq. 2.12) is also shown (dotted line).

from 4.653 a.u. to 4.667 (+ 0.3%) and from 8.052 a.u to 8.078 (+ 0.3%) for zigzag (8,0). The increase is similar in each case, and even comparable to the discrepancy between experiments and GGA or LDA ground states.

The coefficients of linear thermal expansion at any temperature are obtained by direct numerical differentiation of the previous data. Results are shown in Figs. 4-6, 4-7, 4-8 and 4-9. For the case of diamond, we also plot the linear thermal expansion coefficient calculated using the Grüneisen formalism (Eq. 2.12) instead of directly minimizing the free energy. While at low temperature the two curves agree, a discrepancy becomes notable above 1000 K, and direct minimization should be performed. This difference between the Grüneisen approach and a direct minimization seems to explain much of the discrepancy between the calculations of Ref. [20] and our results. Finally a Monte-Carlo path integral study by Herrero and Ramírez [91], which does
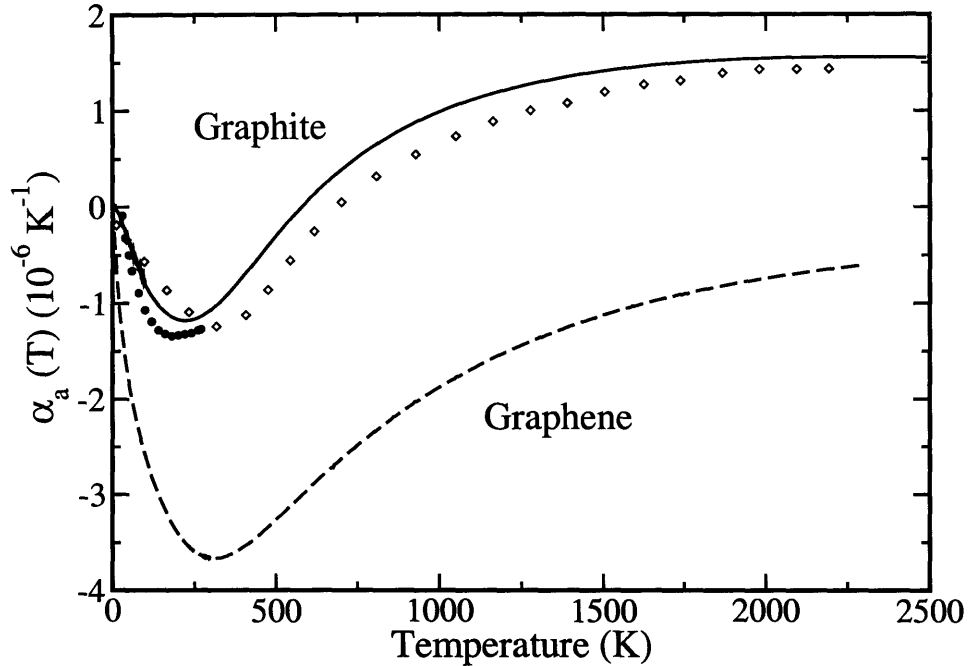
Figure 4-7: In-plane coefficient of linear thermal expansion as a function of temperature for graphite (solid line) and graphene (dashed line) from our QHA-GGA ab-initio study. The experimental results for graphite are from Ref. [33] (filled circles) and Ref. [7] (open diamonds).

not use the QHA, gives very similar results.

For graphite, the in-plane coefficient of linear thermal expansion slightly overestimates the experimental values, but overall the agreement remains excellent, even at high temperatures. Out-of-plane, the agreement holds well up to 150 K, after which the coefficient of linear thermal expansion is underestimated by about 30% at 1000 K. In-plane, the coefficient of linear thermal expansion is confirmed to be negative from 0 to about 600 K. This feature, absent in diamond, is much more apparent in graphene, where the coefficient of linear thermal expansion keeps being negative up to 2300 K.

Thermal contraction along the axis appears in both armchair (5,5) and zigzag (8,0) SWNTs, in a temperature range from 0 to $\sim$ 450 K. The maximum contraction is reached at 200 K for the armchair (5,5) tube, 210 K for the zigzag (8,0) one, compared to 220 K and 310 K for graphite and graphene respectively. At these temperatures, the coefficient of linear thermal expansion is $-0.7 \times 10^{-6} K^{-1}$ in armchair
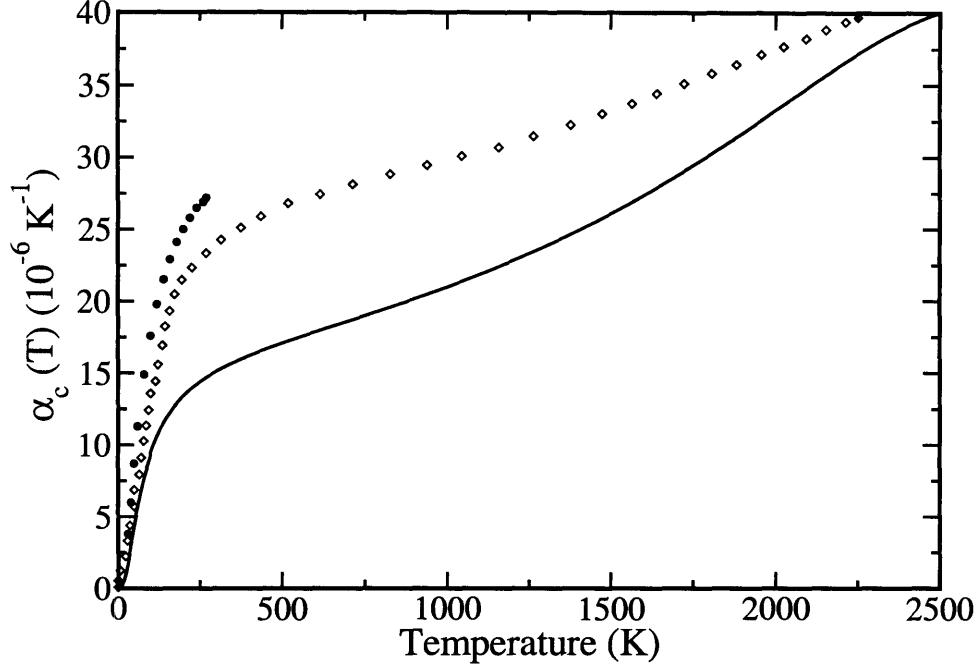
Figure 4-8: Out-of-plane coefficient of linear thermal expansion as a function of temperature for graphite from our QHA-GGA ab-initio study (solid line). The experimental results are from Ref. [33] (filled circles), and Ref. [7] (open diamonds).

(5,5), $-0.8 \times 10^{-6}K^{-1}$ in zigzag (8,0), compared to $-1.2 \times 10^{-6}K^{-1}$ in graphite (in-plane) and $-3.6 \times 10^{-6}K^{-1}$ in graphene. The thermal expansion curves of Fig. 4-9 are very similar, suggesting that the thermal expansion does not significantly depend on chirality. More likely, thermal expansion will depend on the diameter of the nanotube, as also stated in Ref. [12]. Our study disagrees however with the results of Ref. [12] (based, we stress, on an empirical interatomic potential), the most obvious discrepancy being the thermal contraction of graphene, calculated to be half of the in-plane contraction of graphite. Our calculations also disagree with results from molecular dynamics simulations of Ref. [11], in which thermal contraction of a (10,10) SWNT is found to be as large as 10 times higher than that of graphite. On the contrary, our study agrees well with the values obtained from the molecular dynamics simulations and Grüneisen parameters calculations of Ref. [10], which exhibit a coefficient of thermal expansion of $-0.9 \times 10^{-6}K^{-1}$ at room temperature and $2.5 \times 10^{-6}K^{-1}$ at high temperature. Finally, to the best of our knowledge the only experiment to determine
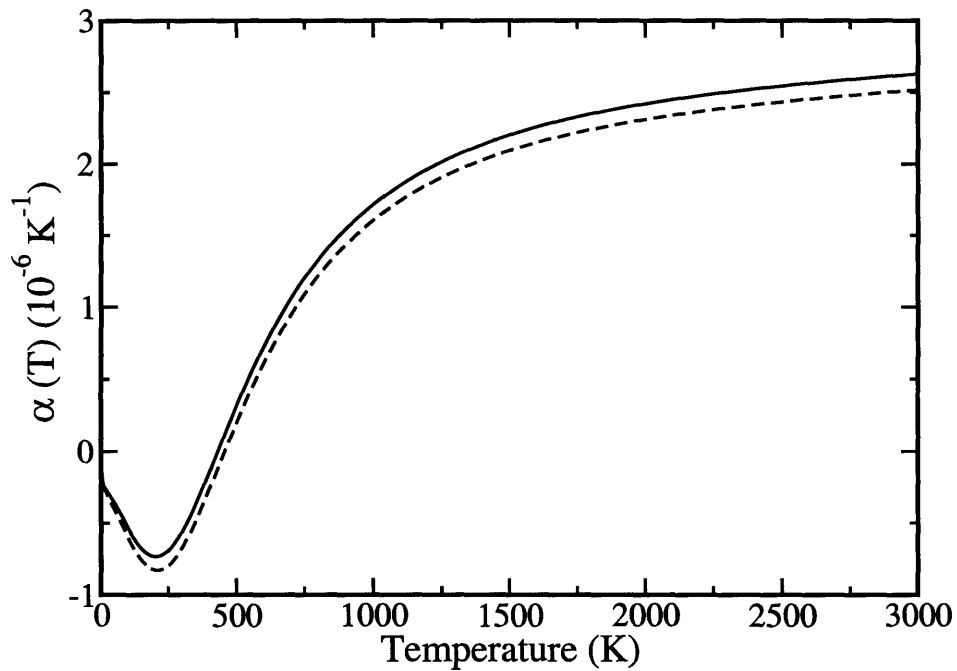
Figure 4-9: Temperature dependence of the coefficient of linear thermal expansion along the axis for armchair (5,5) (solid line) and zigzag(8,0) (dashed line) SWNTs from our QHA-GGA ab-initio study. Note that $\alpha(0) = 0$, and that for $T < 100K$ our calculations are not fully converged with respect to q-sampling.
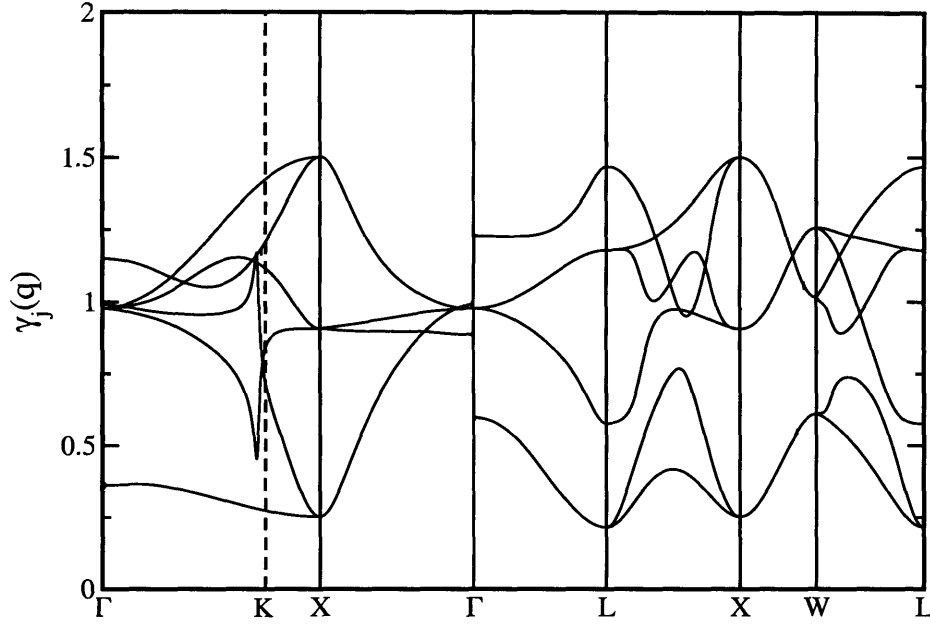
Figure 4-10: Ab-initio mode Grüneisen parameters for diamond

the thermal expansion of SWNT was done by Maniwa *et al* [29] on nanotube bundles, in which a value of $(-1.5 \pm 2.0) \times 10^{-6} K^{-1}$ for the *radial* expansion was found. From the study of Ref. [12] we can consider radial and axial thermal expansion to be similar, and therefore this experimental value is in relatively good agreement with our results.

To further analyze thermal contraction, we plot in Figs. 4-10, 4-11, 4-12, 4-13, and 4-14 the mode Grüneisen parameters (see Section 2.3) of diamond, graphene, graphite and zigzag (8,0) SWNT. These are obtained from an interpolation of the phonon frequencies by a quadratic (or linear, for graphite) polynomial of the lattice constants, and computed at the ground state lattice parameter.

The diamond Grüneisen parameters have been already calculated with LDA (see Refs. [20, 39]); our GGA results agree very well with these. In particular, all the Grüneisen parameters are shown to be positive (at odds with other group IV semiconductors such as Si or Ge). The situation is very different in graphite and graphene, where some bands display large and negative Grüneisen parameters (we have used the definition $\gamma_j(\mathbf{q}) = -\frac{a}{2\omega_j(\mathbf{q})} \frac{d\omega_j(\mathbf{q})}{da}$).

While not visible in the figure, the Grüneisen parameter for the lowest acoustic

67
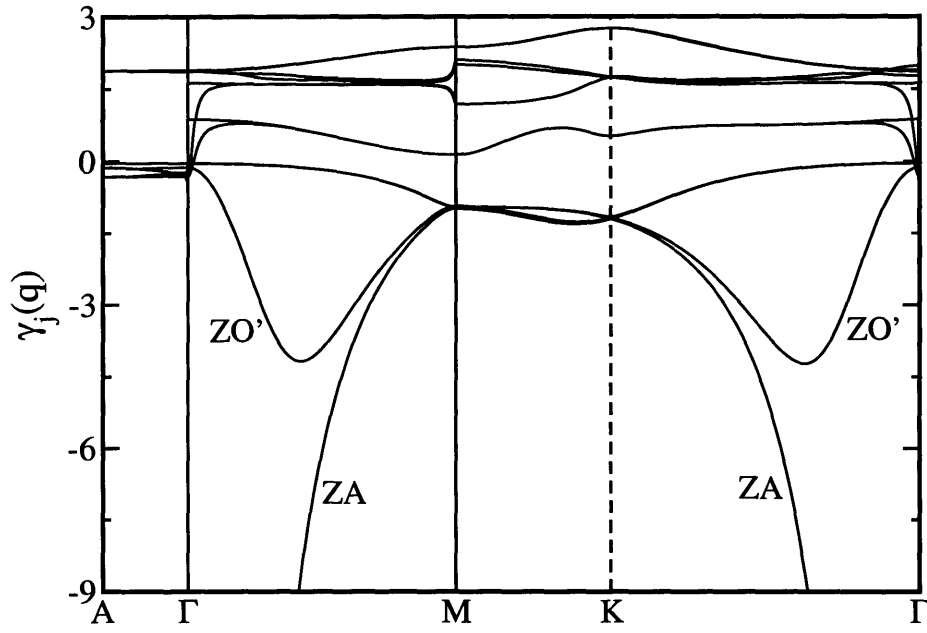
Figure 4-11: Ab-initio in-plane mode Grüneisen parameters for graphite
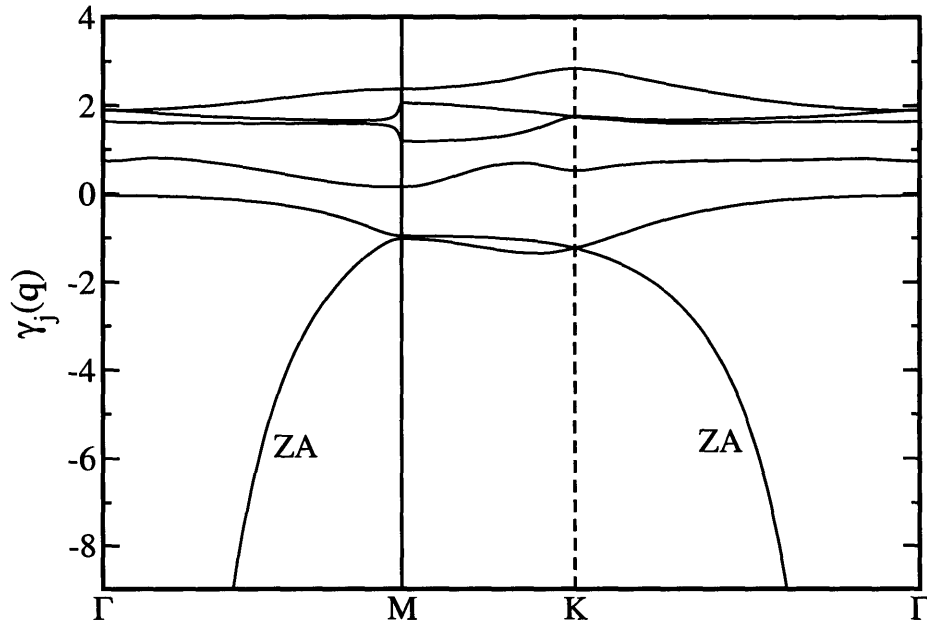
Figure 4-12: Ab-initio mode Grüneisen parameters for graphene
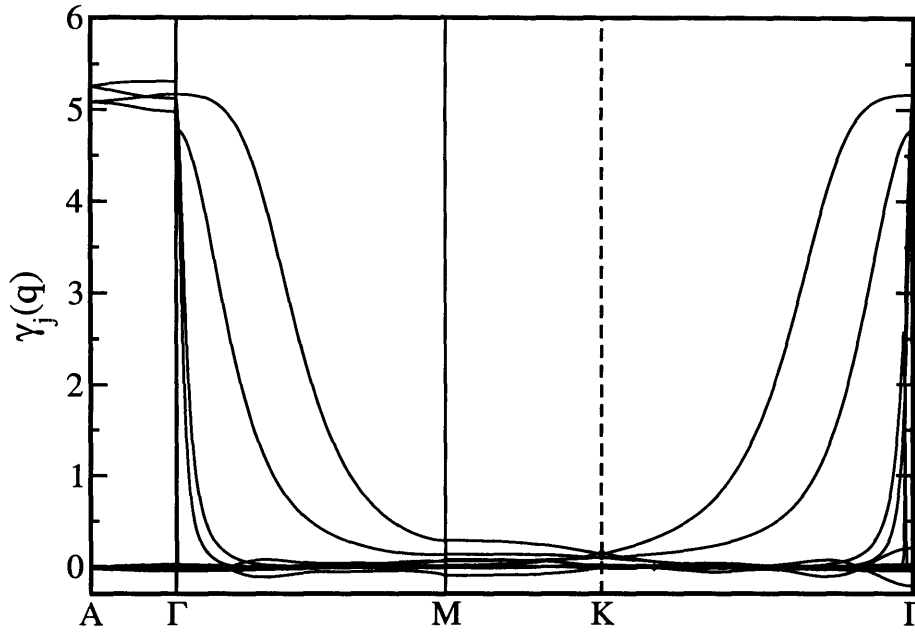
Figure 4-13: Ab-initio out-of-plane mode Grüneisen parameters for graphite
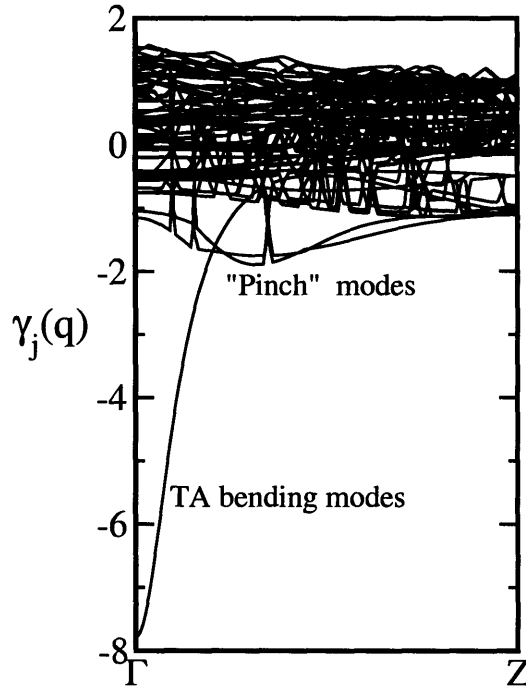
Figure 4-14: Ab-initio mode Grüneisen parameters along the axis for zigzag (8,0) SWNTs

branch of graphite becomes as low as -40, and as low as -80 for graphene. Therefore, at low temperatures (where most optical modes with positive Grüneisen parameters are still not excited) the contribution from the negative Grüneisen parameters will be dominant and thermal expansion (from Eq. 2.12) negative.

In graphene and graphite, the negative Grüneisen parameters correspond to the lowest transversal acoustic (ZA) modes, and in the case of graphite to the (ZO′) modes, which can be described as "acoustic" inside the layer and optical out-of-plane (see Section 3.2). Indeed, the phonon frequencies for such modes increase when the in-plane lattice parameter is increased, contrary to the usual behavior, because the layer is more "stretched" when a is increased, and atoms in that layer will be less free to move in the z direction (just like a rope that is stretched will have vibrations of smaller amplitude, and higher frequency). In graphite these parameters are less negative because of stacking: atoms are less free to move in the z-direction than in the case of graphene.

This thermal contraction, named "membrane effect", was predicted by I. M. Lifshitz [86, 88] in 1952, when he pointed out the role of the ZA modes (also called bending modes) in layered materials. In particular, several recent studies have highlighted the relevance of these modes to the thermal properties of layered crystals such as graphite, boron nitride and gallium sulfide [92, 93, 28].

This picture changes somewhat in SWNTs. In the narrow nanotubes studied the TA bending modes and the "pinch" modes contribute most significantly to the thermal contraction. We represent these modes in Figs. 4-15 and 4-16. The bending modes are playing a role comparable to that in graphene, that is, their frequencies increase when the tube is stretched along it axis, due to a a behavior analogous to that of a string. These modes will contribute less to the thermal contraction for tubes of larger diameters. On the other hand, for larger nanotubes the radial breathing mode (RBM), represented in Fig. 4-17, will start to dominate, since its contribution to the thermal contraction will become more and more similar to that of the ZA modes of graphene, to which it is equivalent in a zone-folding picture [16]. Moreover, the RBM frequency decreases with increasing diameter [15, 16], thus enabling excitation
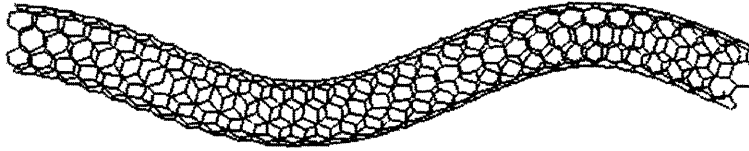
Figure 4-15: Bending mode of a zigzag (8,0) SWNT
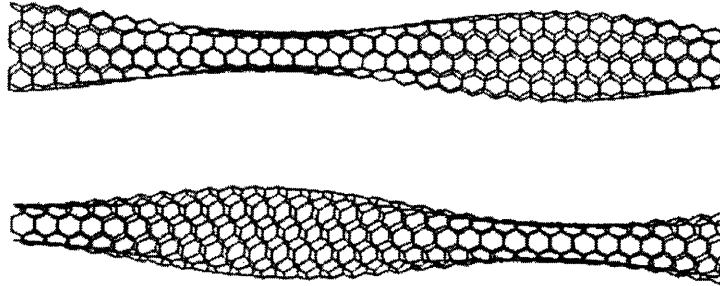
Figure 4-16: "Pinch" mode of a zigzag (8,0) SWNT in two different orientations

at lower temperatures.

Other relevant thermodynamic quantities can also be calculated from the vibrational free energy. E.g., the dependence of elastic constants on temperature can be derived from the second derivatives of the free energy (Eq. 2.8) taken at the respective minimum for any given T. Our results are shown in Figs. 4-18 and 4-19 (diamond and graphite respectively). Again, the zero-point motion has a significant effect on the elastic constants; the agreement with experimental data for the temperature dependence of the bulk modulus of diamond is excellent (upper panel of Fig. 4-18). We note that the temperature dependence of the bulk modulus of diamond has already been obtained by Karch *et al* [94] using LDA calculations.

Finally, we present results on the heat capacities for all the systems considered, both at constant volume (C_v) and constant pressure (C_p). C_v has been computed using Eq. (2.14), in which we use at each temperature T the interpolated phonon frequencies calculated at the lattice constant(s) that minimize the respective free energy. To obtain C_p, we add to C_v the additional term $C_p - C_v = TV_0B_0\alpha_V^2$ where

71
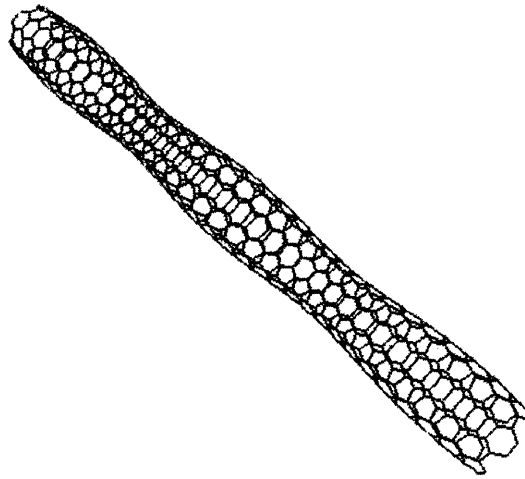
Figure 4-17: Radial breathing mode of a zigzag (8,0) SWNT
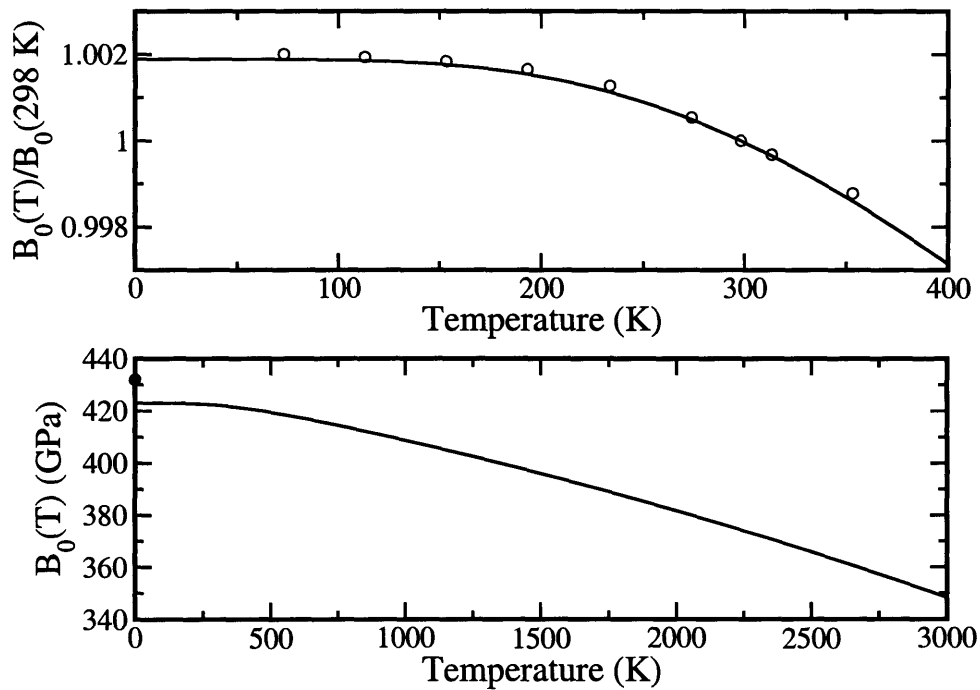
Figure 4-18: Lower panel: Bulk modulus $B_0(T)$ of diamond as a function of temperature. The filled circle indicates the value of the bulk modulus (as in Table 3.1) before accounting for zero-point motion. Upper panel: theoretical (solid line) and experimental values (Ref. [95], open circles) for the ratio between $B_0(T)$ and $B_0(298K)$ in the low temperature regime.
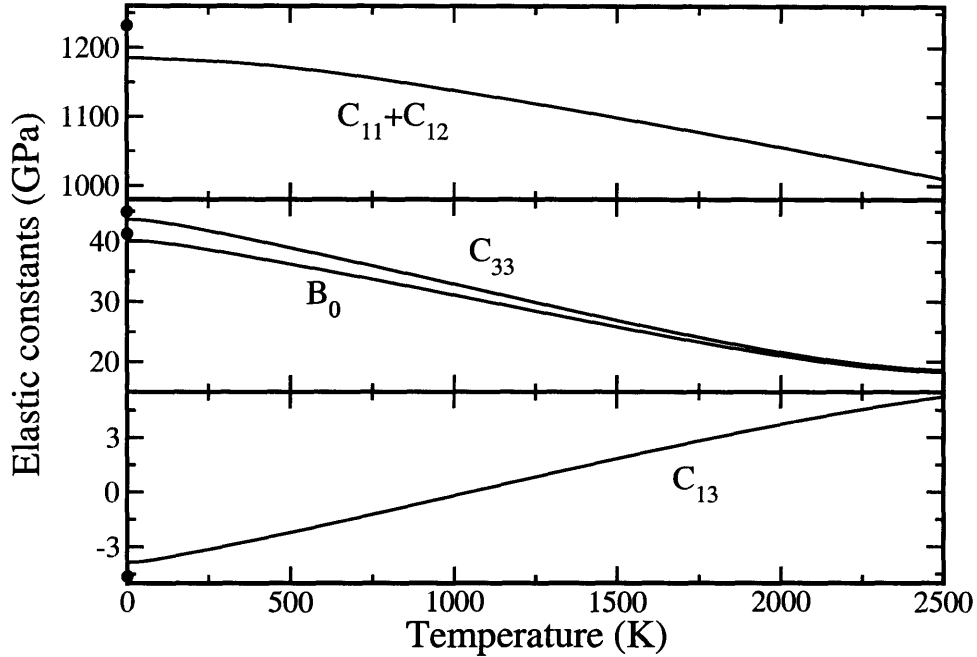
Figure 4-19: Elastic constants of graphite ($C_{11} + C_{12}$, C_{13}, C_{33}) and bulk modulus (B_0) as a function of temperature. The filled circles (at 0 K) indicate their ground state values (as in Table 3.2) before accounting for zero-point motion.

V_0 is the unit cell volume, α_V the volumetric thermal expansion and B_0 the bulk modulus. All these quantities are taken from our ab-initio results and evaluated at each of the temperatures considered. The difference between C_p and C_v is very small, at most about 2% of the value of C_v for graphite and 5% for diamond. Note that C_p and C_v shown on the figures are normalized by dividing by the unit cell mass.

The heat capacity of diamond, graphite, graphene and SWNTs are almost identical except at very low temperatures, in a manifestation of the law of corresponding states for different materials with essentially very similar Debye temperature. In particular, C_v obtained for both (5,5) and (8,0) SWNTs and for graphite are indistinguishable on the temperature range considered (Fig. 4-23). Agreement with experimental data of diamond and graphite is very good.
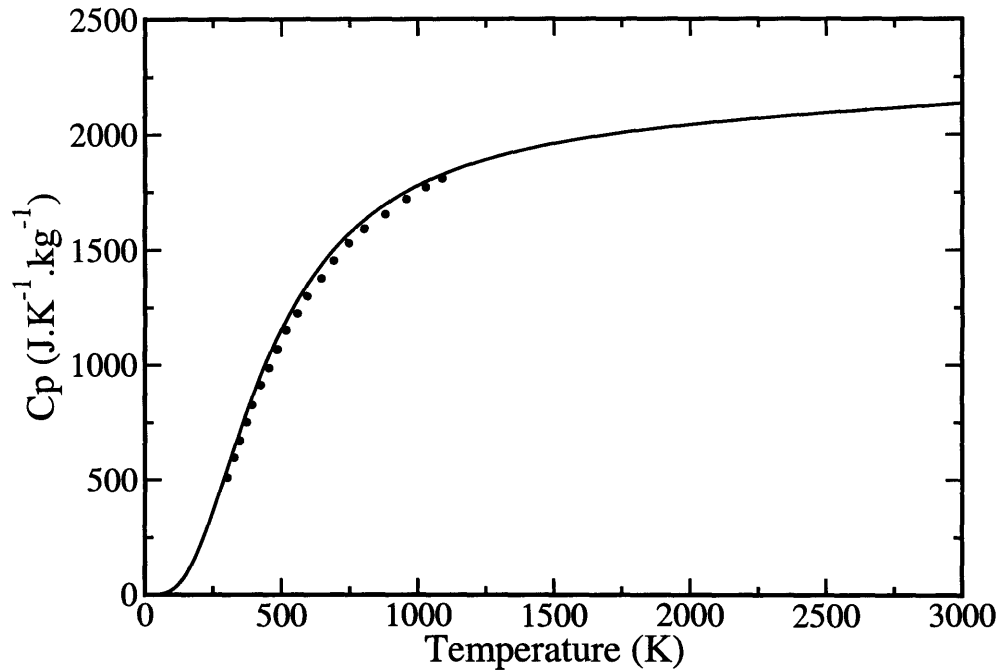
Figure 4-20: Constant pressure heat capacity for diamond (solid line). Experimental results are from Refs. [70] and [96] (circles), as reported by Ref. [91].
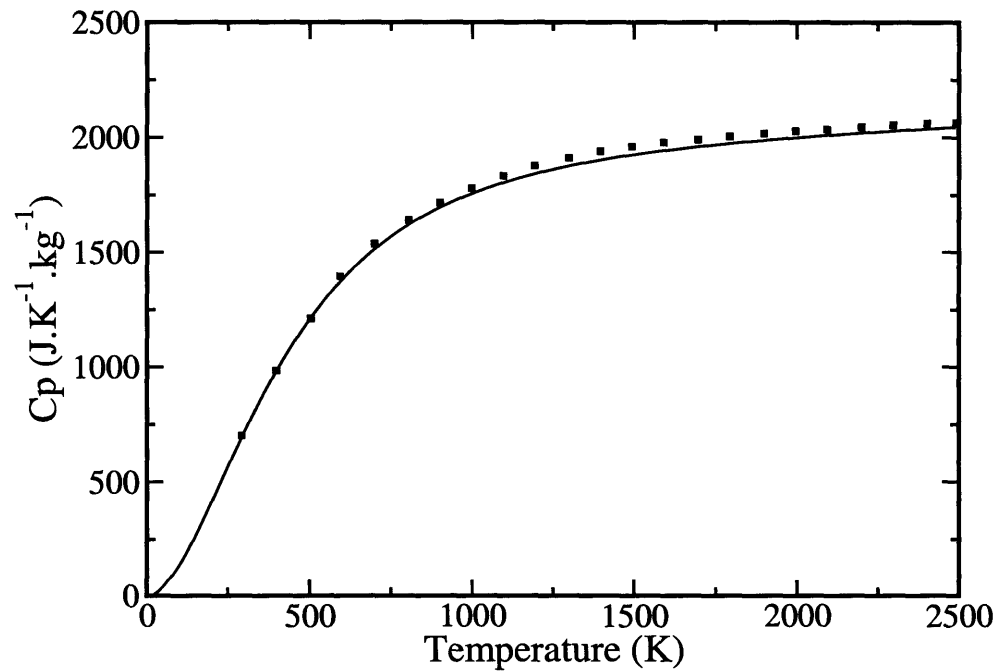
Figure 4-21: Constant pressure heat capacity for graphite (solid line). Experimental results are from Ref. [97] (squares), as reported by Ref. [98].
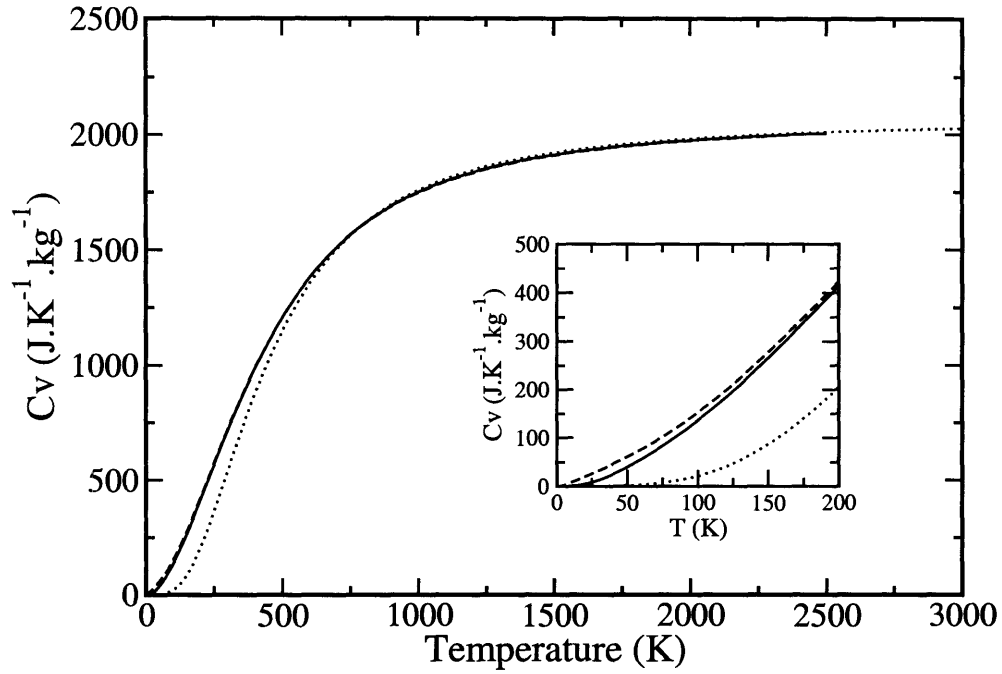
Figure 4-22: Constant volume heat capacity for graphite (solid line), graphene (dashed line) and diamond (dotted line). The inset shows an enlargement of the low temperature region.
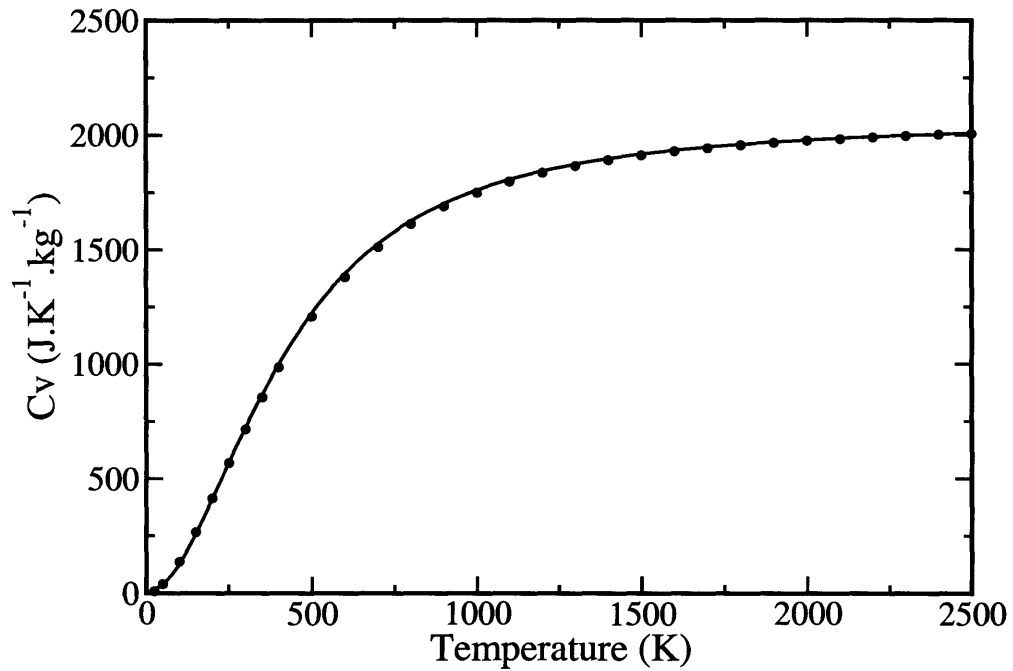
Figure 4-23: Constant volume heat capacity for armchair (5,5) and zigzag (8,0) SWNTs (solid line) and for graphite (circles).

Chapter 5

Conclusions

We have presented a full first-principles study of the structural, vibrational and thermodynamic properties of diamond, graphite, graphene and armchair and zigzag SWNTs at the GGA-PBE level and using the quasi-harmonic approximation to derive thermodynamic quantities. All our results are in very good agreement with experimental data: the phonon dispersions are well reproduced, as well as most of the elastic constants. In graphite, the C_{33} elastic constant and the Γ to A phonon dispersions are found to be in good agreement with experimental results provided the calculations are performed at the experimental c/a. Only the C_{13} constant remains in poor agreement with experimental data. In SWNTs, the elastic constants are shown to be independent on both chirality and diameter, except for very narrow nanotubes, and agree well with both experimental values and other theoretical studies.

The decay of the long-ranged interatomic force constants is analyzed in detail. It is shown that interactions in the (110) direction in diamond are longer-ranged than these in other directions, as is characteristic of the zincblende and diamond structures. For graphene and graphite, in-plane interactions are even longer-ranged and phonon frequencies sensitive to the truncation of the interatomic force constants. Also, the force constants of armchair and zigzag SWNTs are very similar to those of graphene.

Thermodynamic properties such as the thermal expansion, temperature dependence of elastic moduli and specific heat are calculated in the quasi-harmonic approximation. These quantities are all found to be in close agreement with experiments,

except for the out-of-plane thermal expansion of graphite at temperatures higher than 150 K. Graphite shows a distinctive in-plane negative thermal-expansion coefficient that reaches the minimum around room temperature, again in very good agreement with experiments. This effect is found to be three times as large in graphene, and half as large in both (5,5) and (8,0) SWNTs. In the case of graphene and graphite, the mode Grüneisen parameters show that the ZA bending acoustic modes are responsible for the contraction, in a direct manifestation of the membrane effect predicted by Lifshitz [86] in 1952. In narrow single-walled carbon nanotubes, the TA bending modes and the "pinch" modes seem to have the most significant role on the thermal contraction, while the radial breathing mode is likely to play dominant role in larger tubes, for which the thermal contraction may tend toward the value in graphene. In SWNTs, thermal contraction is currently under active investigation [10, 11, 99].

Appendix A

Acoustic sum rules for the interatomic force constants

The interatomic force constants (IFCs) of a material satisfy strict symmetry properties. Obvious ones are the symmetries with respect to a change of indices (index symmetries), deriving from Newton's law of reciprocal action; many others originate from invariance of the system with respect to discrete symmetry operations (e.g. the point-group of the structure). Finally, invariance with respect to translations — and in some cases, rotations as well — that are continuous and rigid also induces certain constraints on the IFCs, often called acoustic sum rules (ASRs). While the discrete symmetries of the system are usually taken into account in our DFPT calculations, it is not the case for the index symmetries or continuous translations and rotations. Therefore, the IFCs obtained using DFPT (see Section 2.2) do not rigorously satisfy either the index symmetries or the ASRs unless one reaches full numerical convergence with respect to the continuous k-point integration on the Brillouin Zone and the basis-set cutoffs. As a consequence, to get more accurate results it is often desirable to enforce these rules (ASRs and index symmetries) on the IFCs. We discuss in the following a novel and general approach to impose such constraints.

A.1 Preliminary definitions

We consider here a perfect crystal whose periodic Bravais lattice has primitive vectors $\{\mathbf{a}_1, \mathbf{a}_2, \mathbf{a}_3\}$. Any lattice vector is therefore expressed as:

$$\mathbf{R_L} = n_1\mathbf{a}_1 + n_3\mathbf{a}_2 + n_3\mathbf{a}_3 \quad , \text{ with } \quad \mathbf{L} = (n_1, n_2, n_3) \tag{A.1}$$

where $\{n_1, n_2, n_3\}$ are integers.

The position of any of the P atoms in the unit cell is then given by:

$$\boldsymbol{\tau}_i = e_1^i\mathbf{a}_1 + e_2^i\mathbf{a}_2 + e_3^i\mathbf{a}_3 \quad , \quad 1 \leq i \leq P \quad , \quad 0 \leq e_k^i \leq 1 \tag{A.2}$$

so that any atom in the crystal is located at:

$$\mathbf{R_{L},i} = \mathbf{R_L} + \boldsymbol{\tau}_i \tag{A.3}$$

These are the equilibrium positions of the ions in the crystal. Let us now consider a set of **lattice displacements** that alter these positions by some small amount:

$$\mathbf{R_{L},i} \rightarrow \mathbf{R_{L},i} + \mathbf{u}_i(\mathbf{R_L}) \tag{A.4}$$

The total energy of the crystal will change, and we can develop it around the equilibrium energy E_0 using a second order Taylor expansion:

$$E = E_0 + \frac{1}{2} \sum_{\mathbf{L},\mathbf{L}',i,j,\alpha,\beta} u_{\alpha i}(\mathbf{R_L})\, C_{\alpha i,\beta j}(\mathbf{R_L}, \mathbf{R_{L}'})\, u_{\beta j}(\mathbf{R_{L}'}) + \mathcal{O}(u^3) \tag{A.5}$$

where α and β can be either 1, 2 or 3 and refer to the cartesian coordinates, and i and j refer to the atoms in the unit cell. The first order term is zero since the expansion is done around the equilibrium configuration, where by definition the forces on the ions are zero.

The coefficients $C_{\alpha i,\beta j}(\mathbf{R_L}, \mathbf{R_{L}'})$ are called **interatomic force constants** (IFCs) and correspond to the second derivatives of the energy calculated at the equilibrium

configuration:

$$C_{\alpha i, \beta j}(\mathbf{R_L}, \mathbf{R_{L'}}) = \left. \frac{\partial^2 E}{\partial u_{\alpha i}(\mathbf{R_L}) \partial u_{\beta j}(\mathbf{R_{L'}})} \right|_{equilibrium} \tag{A.6}$$

The harmonic approximation consists in neglecting in Eq. (A.5) all the terms of order higher than two.

The coefficient $C_{\alpha i, \beta j}(\mathbf{R_L}, \mathbf{R_{L'}})$ represents the proportionality factor between the displacement in the direction β of the atom j of the cell located at $\mathbf{R_{L'}}$, and the component α of the force induced by this displacement on the atom i of the cell located at $\mathbf{R_L}$. For the total force on a given atom we have:

$$F_{\alpha i}(\mathbf{R_L}) = -\frac{\partial E}{\partial u_{\alpha i}(\mathbf{R_L})} = -\sum_{\mathbf{L'}, j, \beta} C_{\alpha i, \beta j}(\mathbf{R_L}, \mathbf{R_{L'}}) \, u_{\beta j}(\mathbf{R_{L'}}) + \mathcal{O}(u^2) \tag{A.7}$$

Due to the periodicity of the lattice, the IFCs must satisfy translational invariance, and will depend only on the relative difference $\mathbf{R_L} - \mathbf{R_{L'}}$:

$$C_{\alpha i, \beta j}(\mathbf{R_L}, \mathbf{R_{L'}}) = C_{\alpha i, \beta j}(\mathbf{R_L} - \mathbf{R_{L'}}) \tag{A.8}$$

We can therefore limit ourselves to the study of the following quantity:

$$C_{\alpha i, \beta j}(\mathbf{R_L}) = \left. \frac{\partial^2 E}{\partial u_{\alpha i}(\mathbf{R_L}) \partial u_{\beta j}(0)} \right|_{equilibrium} \tag{A.9}$$

In an (infinite) periodic crystal, the number of degrees of freedom is infinite, and the extension of the IFCs over $\mathbf{R_L}$, is, in principle, infinite. In practice, we can study systems only with a finite number of degrees of freedom. The natural approach to address this problem is to use periodic boundary conditions: a supercell is defined, of dimensions N_1, N_2 and N_3 times the dimensions of the primitive unit cell, and only perturbations of a wavelength compatible with this supercell are considered. The number of inequivalent atoms is obviously $N_1 N_2 N_3$ times the number of atoms in the primitive unit cell, and this number multiplied by 9, to account for the three cartesian coordinates, is also the number of IFCs. If e.g. we calculate the dynamical matrix on

a $8 \times 8 \times 8$ grid in the first Brillouin zone, then its Fourier transforms are the IFCs for a $8 \times 8 \times 8$ supercell periodically repeated to cover all space.

So the IFCs can be represented by a vector $\mathbf{C}$ in the vector space $\mathbb{R}^{9P^2 N_1 N_2 N_3}$ (P being the number of atoms in the unit cell), whose components are

$$(C_{\alpha i, \beta j}(\mathbf{R_L}(n_1, n_2, n_3)))_{1 \leq \alpha, \beta \leq 3, \ 1 \leq i,j \leq P, \ 1 \leq n_k \leq N_k}$$

This will also be written more compactly as

$$(C_{\alpha \beta i j n_1 n_2 n_3})_{1 \leq \alpha, \beta \leq 3, \ 1 \leq i,j \leq P, \ 1 \leq n_k \leq N_k}$$

to describe the different components.

We define in $\mathbb{R}^{9P^2 N_1 N_2 N_3}$ the usual scalar product

$$(\mathbf{u} \cdot \mathbf{v}) = \sum_{\alpha, \beta, i, j, n_1, n_2, n_3} u_{\alpha \beta i j n_1 n_2 n_3} \cdot v_{\alpha \beta i j n_1 n_2 n_3} \tag{A.10}$$

and the norm

$$\|\mathbf{u}\| = \sqrt{\sum_{\alpha, \beta, i, j, n_1, n_2, n_3} u^2_{\alpha \beta i j n_1 n_2 n_3}} \tag{A.11}$$

As a final note we stress that in all the following $-\mathbf{R_L}$ corresponds to $\mathbf{R_{L'}}$ with $\mathbf{L'} = (N_1 - n_1, N_2 - n_2, N_3 - n_3)$, since our periodic supercell has dimensions (N_1, N_2, N_3).

A.2   Properties of the IFCs

The first and most obvious property is that of index symmetries between the IFCs. By definition we have

$$
\begin{aligned}
C_{\alpha i, \beta j}(\mathbf{R_L}) &= \left. \frac{\partial^2 E}{\partial u_{\alpha i}(\mathbf{R_L}) \partial u_{\beta j}(0)} \right|_{equil} \\
&= \left. \frac{\partial^2 E}{\partial u_{\beta j}(0) \partial u_{\alpha i}(\mathbf{R_L})} \right|_{equil} \\
&= C_{\beta j, \alpha i}(-\mathbf{R_L})
\end{aligned} \tag{A.12}
$$

82

These relations can therefore be compactly written as

$$\forall\ \alpha,\ \beta,\ i,\ j,\ \text{and}\ \mathbf{L}:\quad C_{\alpha i,\beta j}(\mathbf{R_L}) - C_{\beta j,\alpha i}(-\mathbf{R_L}) = 0 \qquad (A.13)$$

In addition, there is continuous translational invariance: if the atoms are all translated by an identical amount, then the energy of the structure will not change (this is true both for infinite periodic crystals and isolated systems). In the case of such a rigid translation, the displacement vector of any atom j in the cell located at $\mathbf{R_L}$ from the origin is a constant that does not depend on j nor on $\mathbf{R_L}$. It can be written as

$$\mathbf{u}_j(\mathbf{R_L}) = \mathbf{u} \qquad (A.14)$$

or in cartesian components

$$u_{\beta j}(\mathbf{R_L}) = u_\beta \qquad (A.15)$$

The force $\mathbf{F}_i(\mathbf{0})$ acting on the ith atom of the unit cell located at the origin vanishes for any such displacement; from Eq. (A.7) we obtain that for any α and i:

$$
\begin{aligned}
F_{\alpha i}(\mathbf{0})\ &= -\sum_{\mathbf{L},j,\beta} C_{\alpha i,\beta j}(-\mathbf{R_L})\, u_{\beta j}(\mathbf{R_L}) \\
&= -\sum_{\mathbf{L},j,\beta} C_{\alpha i,\beta j}(-\mathbf{R_L})\, u_\beta \\
&= -\sum_{\mathbf{L},j,\beta} C_{\alpha i,\beta j}(\mathbf{R_L})\, u_\beta
\end{aligned}
$$

(since a sum over $\mathbf{L}$ is equivalent to a sum over $-\mathbf{L}$)

$$= 0 \qquad (A.16)$$

Since this is true for any uniform displacement field $\mathbf{u}$, we can apply these relations to the three cartesian basis vectors $(1,0,0)$, $(0,1,0)$ and $(0,0,1)$. We finally obtain $9P$ relations that the IFCs should verify:

$$\forall\ \alpha,\ \beta\ \text{and}\ i:\quad \sum_{\mathbf{L},j} C_{\alpha i,\beta j}(\mathbf{R_L}) = 0 \qquad (A.17)$$

These relations are called acoustic sum rules and ensure that the phonon frequencies of the three acoustic modes vanish at Γ.

For some structures rotational invariance can also occur. Then, for any displacement of the atoms corresponding to a uniform and rigid rotation of the system, the total energy will not change. This is true only for systems where such a rigid rotation is possible, which excludes infinite periodic 3D and 2D crystals. On the contrary, 1D crystals (e.g. infinite nanotubes) can rotate about their axis, and isolated finite systems containing three atoms or more can also rotate about three independent cartesian axes. Note that diatomic molecules can have meaningful rotations only about two axes (the two independent axes perpendicular to the line connecting the two atoms), because a rotation about the axis connecting the two atoms would not change the atomic positions. (Of course we do not consider here the trivial case of a single isolated atom for which the energy is a constant.)

To begin with, we consider the case of a system that has rotational invariance about one axis, that we assume to be (Oz). With the notations defined above, we have for any j and $\mathbf{L}$

$$\mathbf{u}_j(\mathbf{R_L}) = \boldsymbol{\tau}_j^{new} - \boldsymbol{\tau}_j^{old} \tag{A.18}$$

where $\boldsymbol{\tau}_j^{old}$ and $\boldsymbol{\tau}_j^{new}$ are the positions of the atom j before and after rotation, respectively. By definition the unperturbed position does not depend on $\mathbf{L}$ (the system is perfectly periodic at equilibrium), and $\boldsymbol{\tau}_j^{new}$ does not depend on $\mathbf{L}$ either: if the system is an isolated molecule, then the only possible value for $\mathbf{L}$ is $\mathbf{0}$ ($N_1 = N_2 = N_3 = 1$, and the IFCs supercell is the unit cell); if the system is one-dimensional the only possible invariant rotation is around the one-dimensional axis, so that for any $\mathbf{L}$, $\mathbf{R_L}$ is collinear to (Oz) and the new positions in each cell do not depend on where the cell is with respect to the origin. We call R_{Oz}^θ the matrix of rotations around (Oz) by an angle θ; in cartesian coordinates we write

$$R_{Oz}^\theta = \begin{bmatrix} \cos\theta & -\sin\theta & 0 \\ \sin\theta & \cos\theta & 0 \\ 0 & 0 & 1 \end{bmatrix} \quad , \quad \boldsymbol{\tau}_j^{old} = \begin{pmatrix} x_j^1 \\ x_j^2 \\ x_j^3 \end{pmatrix} \tag{A.19}$$

84

For any j and $\mathbf{L}$, we have therefore:

$$\mathbf{u}_j(\mathbf{R_L}) = (R_{Oz}^{\theta} - I)\tau_j^{old} \qquad (I \text{ being the identity matrix})$$

$$= \begin{pmatrix} x_j^1 \cos\theta - x_j^2 \sin\theta - x_j^1 \\ x_j^1 \sin\theta + x_j^2 \cos\theta - x_j^2 \\ 0 \end{pmatrix} \qquad (A.20)$$

We can obtain the sum rule sought for by requiring that for any small angle of rotation θ the force acting on the atoms of the unit cell is zero:

$$\forall \, \alpha \text{ and } i: \; F_{\alpha i}(\mathbf{0}) = -\sum_{\mathbf{L},j,\beta} C_{\alpha i,\beta j}(-\mathbf{R_L})\, u_{\beta j}(\mathbf{R_L})$$

$$= -\sum_{\mathbf{L},j} \big[C_{\alpha i,1j}(-\mathbf{R_L})\,(x_j^1 \cos\theta - x_j^2 \sin\theta - x_j^1)$$
$$+ \; C_{\alpha i,2j}(-\mathbf{R_L})\,(x_j^1 \sin\theta + x_j^2 \cos\theta - x_j^2)\big]$$

$$= -\sum_{\mathbf{L},j} \big[C_{\alpha i,1j}(\mathbf{R_L})\,(x_j^1 \cos\theta - x_j^2 \sin\theta - x_j^1)$$
$$+ \; C_{\alpha i,2j}(\mathbf{R_L})\,(x_j^1 \sin\theta + x_j^2 \cos\theta - x_j^2)\big]$$

$$= \cos\theta \sum_{\mathbf{L},j} \big[C_{\alpha i,1j}(\mathbf{R_L})x_j^1 + C_{\alpha i,2j}(\mathbf{R_L})x_j^2 \big]$$
$$+ \sin\theta \sum_{\mathbf{L},j} \big[-C_{\alpha i,1j}(\mathbf{R_L})x_j^2 + C_{\alpha i,2j}(\mathbf{R_L})x_j^1 \big]$$
$$- \sum_{\mathbf{L},j} \big[C_{\alpha i,1j}(\mathbf{R_L})x_j^1 + C_{\alpha i,2j}(\mathbf{R_L})x_j^2 \big] = \qquad (A.21)$$

Since we are working in the limit of small displacements $\cos\theta = 1$ and $\sin\theta = \theta$, and we get

$$\forall \, \alpha \text{ and } i: \; \sum_{\mathbf{L},j} -C_{\alpha i,1j}(\mathbf{R_L})x_j^2 + C_{\alpha i,2j}(\mathbf{R_L})x_j^1 = 0 \qquad (A.22)$$

By simple permutation of the indices $\{1,2\}$ into $\{2,3\}$ and $\{3,1\}$ one can obtain the relations for rotations about (Ox) and (Oy). So, depending on the number of independent rotation axes present in the system, we get one, two or three sets of equations, corresponding to $3P$, $6P$ or $9P$ relations between the IFCS, for one-dimensional

85

systems, diatomic molecules or molecules containing more than three atoms, respectively. This is in turn responsible for either one, two or three zero frequencies for the vibrational modes at Γ (in addition to the three frequencies that are zero because of continuous translational invariance), corresponding to one, two or three new rotational acoustic sum rules. Finally, we can write all these relations in a general form:

$\forall\ \alpha$, i, and $\forall\ \beta$ among the possible rotation axes of the system:

$$\sum_{\mathbf{L},j} -C_{\alpha i,(\beta+1)j}(\mathbf{R_L})x_j^{\beta+2} + C_{\alpha i,(\beta+2)j}(\mathbf{R_L})x_j^{\beta+1} = 0$$

(A.23)

in which the operations $\beta + 1$ and $\beta + 2$ are modulo 3 (i.e. 4 corresponds to 1 and 5 to 2). Note that Eqs. (A.17) and (A.23) were also obtained in Ref. [101] (Eqs. (3.2) and (3.3)).

In summary the relations that have to be satisfied by the IFCs are given by Eqs. (A.13), (A.17) and (A.23), corresponding to index symmetries, translational invariance and rotational invariance respectively. The IFCs coming from DFPT calculations will satisfy these relations only approximatively (and more and more accurately as the Brillouin zone sampling and cutoffs are increased). There are two reasons why it is advantageous to enforce — using a "post-processing" step — the ASRs on the IFCs resulting from DFPT calculations:

1. The long wavelength limit of the acoustic modes will always be zero.

2. The thermodynamic and numerical limit (infinite k-points and cutoffs) will be reached much faster for the renormalized IFCs than for the bare IFCs from DFPT. This is particularly significant for e.g. the parabolic bending modes in graphene or nanotubes, and the twisting mode in nanotubes.

In the next section we discuss our strategy to accomplish this task.

A.3 A new approach to apply the acoustic sum rules and index symmetry constraints

Usually the three translational acoustic sum rules and the index symmetries are imposed in the following way: the relations A.17 are enforced by calculating $\sum_{\mathbf{L},j} C_{\alpha i,\beta j}(\mathbf{R_L})$ (approximatively $\simeq 0$) and subtracting this result from $C_{\alpha i,\beta i}(\mathbf{R}_{(0,0,0)})$ (for any α, β and i). Then, the index symmetries are applied: for any pair of non diagonal elements (i.e. not in the form $C_{\alpha i,\alpha i}(\mathbf{R}_{(0,0,0)})$), the average $\frac{C_{\alpha i,\beta j}(\mathbf{R_L})+C_{\beta j,\alpha i}(-\mathbf{R_L})}{2}$ is calculated, and both $C_{\alpha i,\beta j}(\mathbf{R_L})$ and $C_{\beta j,\alpha i}(-\mathbf{R_L})$ are set equal to it. This procedure is trivial to implement, and obviously very fast, but it has some shortcomings:

- The two constraints (translational acoustic sum rules and index symmetries) are treated separately and therefore one cannot assure that the sum rules will remain unchanged when the index symmetries are applied (or vice versa).

- There is no guarantee that this procedure leads to "optimal" IFCs, i.e. IFCs that are the least different from the initial ones (e.g. the optical frequencies can be affected).

- To the best of our knowledge, no simple way has been found to incorporate the rotational acoustic sum rules into this procedure. Even if this were the case, the need of imposing all the sum rules simultaneously would become even more apparent.

Our novel approach strives to overcome all these shortcomings, by obtaining the IFCs the "nearest" to the original ones that verify all the relations (A.13), (A.17) and (A.23). This problem can be easily recast in the language of linear algebra: given a vector $\mathbf{C}$ of the space $\mathbb{R}^{9P^2 N_1 N_2 N_3}$ (see Section A.1), we want to find the vector $\mathbf{C}'$ such that:

- $\mathbf{C}'$ satisfies all the relations (A.13), (A.17) and (A.23),

- $\|\mathbf{C}' - \mathbf{C}\|$ is minimum.

Vectors of $\mathbb{R}^{9P^2 N_1 N_2 N_3}$ that satisfy (A.13), (A.17) and (A.23) span a vector subspace $\mathbb{F}$. The solution $\mathbf{C}'$ of our problem will then be simply given by taking the projection of $\mathbf{C}$ onto $\mathbb{F}$.

While this solution is very simple in principle, we also need to make this projection as computationally efficiently as possible. To begin with, elements $\mathbf{Q}$ of the subspace $\mathbb{F}$ are characterized by the following relations, valid for any α' and i' and equivalent to (A.13), (A.17) and (A.23):

$$\forall\, \beta', \qquad\qquad\qquad \left(\mathbf{Q} \cdot \mathbf{u}^{\alpha'\beta'i'}\right) = 0$$

$$\forall\, \beta' \text{ among the rotation axes of the system,} \qquad \left(\mathbf{Q} \cdot \mathbf{v}^{\alpha'\beta'i'}\right) = 0$$

$$\forall\, \beta' \geq \alpha',\ j' \geq i',\ n_1',\ n_2',\ n_3' \text{ such that} \qquad \left(\mathbf{Q} \cdot \mathbf{w}^{\alpha'\beta'i'j'n_1'n_2'n_3'}\right) = 0$$
$$(\beta', j', n_1', n_2', n_3') \neq (\alpha', i', 0, 0, 0),$$

$$\text{(A.24)}$$

where the components of the vectors $\mathbf{u}^{\alpha'\beta'i'}$, $\mathbf{v}^{\alpha'\beta'i'}$ and $\mathbf{w}^{\alpha'\beta'i'j'n_1'n_2'n_3'}$ of $\mathbb{R}^{9P^2 N_1 N_2 N_3}$ are defined as follow:

$$u^{\alpha'\beta'i'}_{\alpha\beta ijn_1 n_2 n_3} = \begin{cases} 1 & \text{if } \alpha = \alpha',\ i = i' \text{ and } \beta = \beta' \\ 0 & \text{in all the other cases} \end{cases} \qquad \text{(A.25a)}$$

$$v^{\alpha'\beta'i'}_{\alpha\beta ijn_1 n_2 n_3} = \begin{cases} -x_j^{\beta'+2} & \text{if } \alpha = \alpha',\ i = i' \text{ and } \beta = \beta'+1 \,(\text{mod } 3) \\ x_j^{\beta'+1} & \text{if } \alpha = \alpha',\ i = i' \text{ and } \beta = \beta'+2 \,(\text{mod } 3) \\ 0 & \text{in all the other cases} \end{cases} \qquad \text{(A.25b)}$$

$$w^{\alpha'\beta'i'j'n_1'n_2'n_3'}_{\alpha\beta ijn_1 n_2 n_3} = \begin{cases} \frac{1}{\sqrt{2}} & \text{if } \alpha = \alpha',\ \beta = \beta',\ i = i',\ j = j',\ n_1 = n_1',\ n_2 = n_2' \text{ and } n_3 = n_3' \\[2mm] \frac{-1}{\sqrt{2}} & \text{if } \alpha = \beta',\ \beta = \alpha',\ i = j',\ j = i',\ n_1 = N_1 - n_1', \\ & n_2 = N_2 - n_2' \text{ and } n_3 = N_3 - n_3' \\[2mm] 0 & \text{in all the other cases} \end{cases} \qquad \text{(A.25c)}$$

By definition, the subspace generated by the vectors $\mathbf{u}^{\alpha'\beta'i'}$, $\mathbf{v}^{\alpha'\beta'i'}$ and $\mathbf{w}^{\alpha'\beta'i'j'n_1'n_2'n_3'}$ is $\mathbb{F}^\perp$, the orthogonal of $\mathbb{F}$. To calculate $\mathbf{C}'$, projection of our initial vector $\mathbf{C}$ on $\mathbb{F}$, we choose first to compute the projection $\mathbf{C}''$ of $\mathbf{C}$ onto $\mathbb{F}^\perp$; $\mathbf{C}'$ can then be readily obtained from $\mathbf{C}' = \mathbf{C} - \mathbf{C}''$, since we know that $\mathbb{R}^{9P^2N_1N_2N_3} = \mathbb{F} \oplus \mathbb{F}^\perp$. The projection on $\mathbb{F}^\perp$ is easier to compute than the direct projection on $\mathbb{F}$ because we can obtain an orthonormal basis set of $\mathbb{F}^\perp$ from the family of vectors $\left(\mathbf{u}^{\alpha'\beta'i'}, \mathbf{v}^{\alpha'\beta'i'}, \mathbf{w}^{\alpha'\beta'i'j'n_1'n_2'n_3'}\right)$ which will allow us to calculate $\mathbf{C}''$ in a straightforward manner.

To build an orthonormal basis set of $\mathbb{F}^\perp$ we first notice that the vectors $\mathbf{w}^{\alpha'\beta'i'j'n_1'n_2'n_3'}$ — defined for any α', i', $\beta' \geq \alpha'$, $j' \geq i'$, n_1', n_2', n_3' except for $(\beta', j', n_1', n_2', n_3') = (\alpha', i', 0, 0, 0)$ — are orthonormal by definition (see Eq. A.25c). Then, one can orthonormalize the whole set by applying a Gram-Schmidt procedure. To simplify the notations we order the vectors $\mathbf{w}^{\alpha'\beta'i'j'n_1'n_2'n_3'}$ from $\mathbf{f}_1$ to $\mathbf{f}_q$, the vectors $\mathbf{u}^{\alpha'\beta'i'}$ from $\mathbf{f}_{q+1}$ to $\mathbf{f}_r$, and the vectors $\mathbf{v}^{\alpha'\beta'i'}$ from $\mathbf{f}_{r+1}$ to $\mathbf{f}_s$ (q, r, s are integers). From the set $(\mathbf{f}_l)_{1 \leq l \leq s}$ we build the orthonormal set $(\mathbf{g}_l)_{1 \leq l \leq m}$ (with $m \leq s$) using the following algorithm:

- For any $1 \leq l \leq q$: $\mathbf{g}_l = \mathbf{f}_l$ (since the vectors $\mathbf{w}^{\alpha'\beta'i'j'n_1'n_2'n_3'}$ are already orthonormalized)

- For any $l \geq q + 1$, until there is no $\mathbf{f}_l$ left:
  If $\left(\mathbf{f}_l - \sum_{l'=1}^{l-1} (\mathbf{f}_l \cdot \mathbf{g}_{l'}) \mathbf{g}_{l'}\right) = 0$ then $\mathbf{f}_l$ is not independent to $(\mathbf{f}_{l'})_{1 \leq l' \leq l-1}$, so we ignore it and reassign the subsequent $\mathbf{f}_{l'}$: $\mathbf{f}_l = \mathbf{f}_{l+1}$, $\mathbf{f}_{l+1} = \mathbf{f}_{l+2}$, etc. [1]
  Otherwise, we set:

$$\mathbf{g}_l = \frac{\mathbf{f}_l - \sum_{l'=1}^{l-1} (\mathbf{f}_l \cdot \mathbf{g}_{l'}) \mathbf{g}_{l'}}{\left\| \mathbf{f}_l - \sum_{l'=1}^{l-1} (\mathbf{f}_l \cdot \mathbf{g}_{l'}) \mathbf{g}_{l'} \right\|} \tag{A.26}$$

The advantages of this orthonormalization procedure (with respect to e.g. methods involving matrix diagonalization, that are more "symmetric") are

- Simplicity of implementation,

- Exploits trivially the notion that the vectors $\mathbf{w}^{\alpha'\beta'i'j'n_1'n_2'n_3'}$ are already orthonormalized,

---

[1] Note that this does not correspond to actual assignments in the computer program. In practice, to save time we simply store the indices of such $(\mathbf{f}_l)$ and skip those indices in all the succeeding operations.

- Vectors of the initial set that are not independent to those preceding them are automatically removed during the process[2].

On the other hand, the Gram-Schmidt orthonormalization is known to be numerically unstable [102] and its resulting basis set depends on the order of the initial set. These do not seem to be serious drawbacks here, first because we are not concerned with the basis set in itself but only as a basis to provide an inexpensive projection onto $\mathbb{F}^\perp$. Second, in all our practical applications we did not notice any hint of numerical instabilities.

Once one obtains the orthonormalized basis set $(\mathbf{g}_l)_{1 \leq l \leq m}$, $\mathbf{C}''$ (the projection of $\mathbf{C}$ onto $\mathbb{F}^\perp$) and then $\mathbf{C}'$ (the projection of $\mathbf{C}$ onto $\mathbb{F}$) can be readily calculated from

$$\mathbf{C}'' = \sum_{l=1}^{m} (\mathbf{C} \cdot \mathbf{g}_l)\, \mathbf{g}_l \qquad (A.27)$$

$$\text{and} \quad \mathbf{C}' = \mathbf{C} - \mathbf{C}'' \qquad (A.28)$$

$\mathbf{C}'$ is the optimal solution of our problem: it satisfies all relations (A.13), (A.17) and (A.23) and minimizes the distance (norm of the difference) with respect to the initial ab-initio interatomic force constants $\mathbf{C}$.

A.4   Complexity of the algorithm

A.4.1   Memory requirements

The standard algorithm used to apply translational acoustic sum rules (presented at the beginning of Section A.3) obviously requires the least amounts of memory, i.e.

---

[2]In particular, some acoustic sum rules that would be "too much" for the system are taken away automatically at this point. It is the case of e.g. diatomic molecules for which the three rotation acoustic sum rules would have been initially applied: the one that should not be there will disappear during the Gram-Schmidt orthonormalization. More generally, it can be shown that the "translational" (**u**) and "rotational" (**v**) vectors are not independent if and only if all the atoms are aligned on a single line at equilibrium (the proof of this result being quite tedious, we will not provide it here). Therefore, even after having applied our procedure, linear structures might exhibit less zero-frequency phonon modes at Γ than expected from what was outlined in Section A.2. A simple remedy to this issue would be to displace slightly the atoms so that they are not exactly aligned anymore.

only the memory necessary to store the IFCs, which is $\mathcal{O}\left(P^2 N_1 N_2 N_3\right)$ (using the definitions from Section A.1).

Our approach is more demanding. We choose to store the vectors $\mathbf{u}^{\alpha'\beta'i'}$ and $\mathbf{v}^{\alpha'\beta'i'}$ (i.e. the vectors $(\mathbf{f}_l)_{q<l\leq s}$) as full vectors of $\mathbb{R}^{9P^2 N_1 N_2 N_3}$, i.e. as seven-indices arrays containing $9P^2 N_1 N_2 N_3$ components. These arrays are used first to store the vectors $\mathbf{f}_l$ ($q < l \leq s$) and are then gradually replaced by the vectors $\mathbf{g}_l$ ($q < l \leq m$) during the orthonormalization procedure. Since the latter vectors can have all their components different from zero, we cannot gain space in memory, even if the initial vectors $\mathbf{f}_l$ ($q < l \leq s$) have most of their components equal to zero. The number $s - q$ of vectors $\mathbf{u}^{\alpha'\beta'i'}$ and $\mathbf{v}^{\alpha'\beta'i'}$ is at most $18P$ (see Section A.2) and each of them takes as much space as the IFCs, so on the whole we have a memory requirement of $\mathcal{O}\left(P^3 N_1 N_2 N_3\right)$.

On the other hand, the vectors $\mathbf{w}^{\alpha'\beta'i'j'n_1'n_2'n_3'}$ (i.e. the vectors $(\mathbf{f}_l)_{1\leq l\leq q}$) are stored as compactly as possible. Indeed, these vectors have all their components but two equal to zero (see Eq. A.25c), and they do not change during the orthonormalization procedure. So we can store only the seven indices $(\alpha, \beta, i, j, n_1, n_2, n_3)$ of each of the two non-zero elements, as well as the value of these two elements (instead of storing all the $9P^2 N_1 N_2 N_3$ coefficients of the vector). This corresponds to a memory requirement of $\mathcal{O}\left(P^2 N_1 N_2 N_3\right)$ (the number q of such vectors is of same order as the number of coefficients in the IFCs).

Finally, the memory requirements are dominated by the storage of the $\mathbf{u}$ and $\mathbf{v}$ vectors and are of order $\mathcal{O}\left(P^3 N_1 N_2 N_3\right)$. These allocations remain manageable even for a system such as the (8,0) nanotube ($P = 32$) with a $1 \times 1 \times 8$ q-points grid, and are in any case negligible compared to the memory requirements of the corresponding DFPT calculations.

A.4.2   Computational time

Again, the standard algorithm to apply the translational acoustic sum rules requires negligible computation time. Only two loops on all the components of the IFCs (one for the acoustic sum rules, one for the index symmetries) are sufficient, corresponding to a complexity of $\mathcal{O}\left(P^2 N_1 N_2 N_3\right)$.

Our method is computationally much more intensive and the time requirement would rapidly dominate if several shortcuts were not used. Our optimal algorithm is articulated in three steps:

1. We initialize the $\mathbf{u}$, $\mathbf{v}$ and $\mathbf{w}$ vectors according to Eq. (A.25): this takes an amount of time of the same order as the total memory requirement, i.e. $\mathcal{O}\left(P^3 N_1 N_2 N_3\right)$.

2. We perform the Gram-Schmidt orthonormalization, having to calculate as many as $s - q = 18P$ (which is the total number of $\mathbf{u}$ and $\mathbf{v}$ vectors, see Section A.2) sums $\sum_{l'=1}^{l-1}\left(\mathbf{f}_l \cdot \mathbf{g}_{l'}\right)\mathbf{g}_{l'}$ for l between $q+1$ and s (see Eq. A.26). Each of these sums of vectors can be separated into two terms: $\sum_{l'=1}^{q}\left(\mathbf{f}_l \cdot \mathbf{g}_{l'}\right)\mathbf{g}_{l'}$ and $\sum_{l'=q+1}^{l-1}\left(\mathbf{f}_l \cdot \mathbf{g}_{l'}\right)\mathbf{g}_{l'}$. The first one is a sum over $\mathcal{O}\left(P^2 N_1 N_2 N_3\right)$ terms (the number of $\mathbf{w}$ vectors), but where the scalar products can be programmed as a $\mathcal{O}(1)$ operation. Indeed, the vectors $\left(\mathbf{g}_{l'}\right)_{1 \leq l' \leq q}$ are the $\mathbf{w}$ vectors and they are coded indicating the indices of the two non-zero elements (as explained in Section A.4.1); therefore there is no need to loop on all the coefficients of $\mathbf{g}_{l'}$ and only two operations are needed. At each step l' of the summation only two coefficients (corresponding to the non-zero components of $\mathbf{g}_l'$) of the current vector-sum being computed need to be reassigned. So this first sum of vectors takes an amount of time of $\mathcal{O}\left(P^2 N_1 N_2 N_3\right)$.

The second term is a sum over $l - q$ elements, that can be at most equal to $s - q = 18P$. The scalar products can be simplified realizing that most of the components of $\mathbf{f}_l$ are zero: only $3P N_1 N_2 N_3$ components are non-zero (the ones corresponding to $\alpha = \alpha'$ and $i = i'$ if $\mathbf{f}_l = \mathbf{u}^{\alpha' \beta' i'}$), and the scalar product will need only $\mathcal{O}\left(P N_1 N_2 N_3\right)$ operations. On the other hand, all the components of the current vector-sum being computed need to be reassigned at each step in the summation, which represents a cost of $\mathcal{O}\left(P^2 N_1 N_2 N_3\right)$. In the end we get a total complexity of $\mathcal{O}\left(P^3 N_1 N_2 N_3\right)$, since there are $18P$ terms in that sum.

Since there are $18P$ sums, we have a total time requirement $\mathcal{O}\left(P^4 N_1 N_2 N_3\right)$ for the whole orthonormalization procedure. Note that if we had not used

these shortcuts (especially regarding the management of the $\mathbf{w}$ vectors), the complexity would have been much higher, of order $\mathcal{O}\left(P^5 N_1^2 N_2^2 N_3^2\right)$.

3. We project $\mathbf{C}$ onto $\mathbb{F}^\perp$. The sum $\sum_{l=1}^{m}\left(\mathbf{C} \cdot \mathbf{g}_l\right) \mathbf{g}_l$ in Eq. (A.27) can be separated into two terms: $\sum_{l=1}^{q}\left(\mathbf{C} \cdot \mathbf{g}_l\right) \mathbf{g}_l$ and $\sum_{l=q+1}^{m}\left(\mathbf{C} \cdot \mathbf{g}_l\right) \mathbf{g}_l$. As above, in the first term the $\mathbf{g}_l$ are the $\mathbf{w}$ vectors and the sum takes an amount of time of $\mathcal{O}\left(P^2 N_1 N_2 N_3\right)$, since both the scalar product and the reassignments are $\mathcal{O}(1)$. The second term needs a full scalar product to be performed since we do not know in advance which of the components of $\mathbf{g}_l$ will be zero, if any. Both the scalar product and the reassignment of $\mathbf{C}''$ are $\mathcal{O}\left(P^2 N_1 N_2 N_3\right)$ in time, and since this sum is over $18P$ terms at most, the computational time is $\mathcal{O}\left(P^3 N_1 N_2 N_3\right)$. So this final projection step takes an amount of time proportional to $\mathcal{O}\left(P^3 N_1 N_2 N_3\right)$.

It is clear from the above that the most computationally demanding step is the Gram-Schmidt orthonormalization. The complexity of the whole algorithm is therefore expected to be $\mathcal{O}\left(P^4 N_1 N_2 N_3\right)$. In our most dramatic cases, it proves to be still negligible versus the time needed for DFPT calculations, but is certainly not as fast as the standard algorithm usually implemented.

A.5 Conclusion

We have introduced a novel and general method to enforce consistently all the acoustic sum rules and index-symmetry constraints of the IFCs. This approach can be applied to different systems, ranging from 3D crystals (e.g. diamond) to 1D structures (e.g. carbon nanotubes) and diatomic and triatomic molecules. In particular, using DFPT we can compute the dynamical matrix in a regular mesh of q-points in the Brillouin zone, calculate its Fourier transform (obtaining the real space IFCs), renormalize the IFCs with the algorithm detailed above, and then Fourier interpolate back the IFCs at any arbitrary wave-vector. The diagonalization of the dynamical matrix at $\mathbf{q} = \mathbf{0}$ provides three zone-center phonons with exactly zero frequency, and leaves

all the remaining frequencies and eigenvectors largely unaltered when compared with the original quantities obtained diagonalizing the unrenormalized dynamical matrix at any $\mathbf{q}$. This is a definite improvement compared to the standard algorithm which affects higher-energy phonon frequencies and eigenvectors in a more appreciable manner. This improvement is ultimately due to our approach representing the optimal solution to the problem of enforcing all the ASRs, since the distance between the initial IFCs and the renormalized ones is chosen to be minimum via the projection technique. Even if the computational time and memory requirement become significantly larger, they still remain very manageable and fast compared to the DFPT calculation itself. We did not notice any numerical instability in the Gram-Schmidt orthonormalizations; were they to appear, we could still use the "modified" Gram-Schmidt algorithm described in Ref. [102], which does not exhibit this drawback.

Bibliography

[1] K. S. Novoselov, A. K. Geim, S. V. Morozov, D. Jiang, Y. Zhang, S. V. Dubonos, I. V. Grigorieva, and A. A. Firsov. Electric field effect in atomically thin carbon films. *Science*, 306:666, 2004.

[2] R. J. Chen, S. Bangsaruntip, K. A. Drouvalakis, N. Wong Shi Kam, M. Shim, Y. Li, W. Kim, P. J. Utz, and H. Dai. Noncovalent functionalization of carbon nanotubes for highly specific electronic biosensors. *Proc. Natl. Acad. Sci. U.S.A.*, 100:4984, 2003.

[3] G. Galli, R. M. Martin, R. Car, and M. Parrinello. Carbon: The nature of the liquid state. *Phys. Rev. Lett.*, 63:988, 1989.

[4] G. Galli, R. M. Martin, R. Car, and M. Parrinello. Structural and electronic properties of amorphous carbon. *Phys. Rev. Lett.*, 62:555, 1989.

[5] A. De Vita, G. Galli, A. Canning, and R. Car. A microscopic model for surface-induced diamond-to-graphite transitions. *Nature*, 379:523, 1996.

[6] P. Delhaes, editor. *Graphite and Precursors*, chapter 6. Gordon and Breach, Australia, 2001.

[7] H. O. Pierson. *Handbook of carbon, graphite, diamond, and fullerenes : properties, processing, and applications*, pages 59–60. Noyes Publications, Park Ridge, New Jersey, 1993.

[8] S. Iijima. Helical microtubules of graphitic carbon. *Nature*, 354:56, 1991.

[9] C. Li and T.-W. Chou. Elastic properties of single-walled carbon nanotubes in transverse directions. *Phys. Rev. B*, 69:073401, 2004.

[10] P. K. Schelling and P. Keblinski. Thermal expansion of carbon structures. *Phys. Rev. B*, 68:035425, 2003.

[11] Y. K. Kwon, S. Berber, and D. Tománek. Thermal contraction of carbon fullerenes and nanotubes. *Phys. Rev. Lett.*, 92:015901, 2004.

[12] H. Jiang, B. Liu, Y. Huang, and K. C. Hwang. Thermal expansion of single wall carbon nanotubes. *J. Eng. Mater. Technol.*, 126:265, 2004.

[13] M. S. Dresselhaus, G. Dresselhaus, J. C. Charlier, and E. Hernández. Electronic, thermal and mechanical properties of carbon nanotubes. *Phil. Trans. R. Soc. Lond. A*, 362:2065, 2004.

[14] H. Rafii-Tabar. Computational modelling of thermo-mechanical and transport properties of carbon nanotubes. *Physics Reports*, 390:235, 2004.

[15] R. Saito, G. Dresselhaus, and M. S. Dresselhaus. *Physical Properties of Carbon Nanotubes*. Imperial College Press, London, 1998.

[16] S. Reich, C. Thomsen, and J. Maultzsch. *Carbon nanotubes : basic concepts and physical properties*. Wiley-VCH, Weinheim, 2004.

[17] Michael S. Strano. Probing chiral selective reactions using a revised kataura plot for the interpretation of single-walled carbon nanotube spectroscopy. *J. Am. Chem. Soc.*, 125:16148, 2003.

[18] J. L. Warren, J. L. Yarnell, G. Dolling, and R. A. Cowley. Lattice dynamics of diamond. *Phys. Rev.*, 158:805, 1967.

[19] G. A. Slack and S. F. Bartram. Thermal expansion of some diamondlike crystals. *J. Appl. Phys.*, 46:89, 1975.

[20] P. Pavone, K. Karch, O. Schütt, W. Windl, D. Strauch, P. Giannozzi, and S. Baroni. Ab initio lattice dynamics of diamond. *Phys. Rev. B*, 48:3156, 1993.

[21] J. Maultzsch, S. Reich, C. Thomsen, H. Requardt, and P. Ordejón. Phonon dispersion in graphite. *Phys. Rev. Lett.*, 92:075501, 2004.

[22] L. Wirtz and A. Rubio. The phonon dispersion of graphite revisited. *Solid State Commun.*, 131:141, 2004.

[23] O. Dubay and G. Kresse. Accurate density functional calculations for the phonon dispersion relations of graphite layer and carbon nanotubes. *Phys. Rev. B*, 67:035401, 2003.

[24] L. H. Ye, B. G. Liu, D. S. Wang, and R. Han. Ab initio phonon dispersions of single-wall carbon nanotubes. *Phys. Rev. B*, 69:235409, 2004.

[25] D. Sánchez-Portal, E. Artacho, J. M. Soler, A. Rubio, and P. Ordejón. Ab initio structural, elastic, and vibrational properties of carbon nanotubes. *Phys. Rev. B*, 59:12678, 1999.

[26] S. Rols, Z. Benes, E. Anglaret, J. L. Sauvajol, P. Papanek, J. E. Fischer, G. Coddens, H. Schober, and A. J. Dianoux. Phonon density of states of single-wall carbon nanotubes. *Phys. Rev. Lett.*, 85:5222, 2000.

[27] K. P. Bohnen, R. Heid, H. J. Liu, and C. T. Chan. Lattice dynamics and electron-phonon interaction in (3,3) carbon nanotubes. *Phys. Rev. Lett.*, 93:245501, 2004.

[28] N. A. Abdullaev, R. A. Suleimanov, M. A. Aldzhanov, and L. N. Alieva. On the role played by bending vibrations in heat transfer in layered crystals. *Phys. Solid State*, 44:1859, 2002.

[29] Y. Maniwa, R. Fujiwara, H. Kira, H. Tou, H. Kataura, S. Suzuki, Y. Achiba, E. Nishibori, M. Takata, M. Sakata, A. Fujiwara, and H. Suematsu. Thermal expansion of single-walled carbon nanotube (SWNT) bundles: X-ray diffraction studies. *Phys. Rev. B*, 64:241402, 2001.

[30] N. R. Raravikar, P. Keblinski, A. M. Rao, M. S. Dresselhaus, L. S. Schadler, and P. M. Ajayan. Temperature dependence of radial breathing mode Raman frequency of single-walled carbon nanotubes. *Phys. Rev. B*, 66:235424, 2002.

[31] V. N. Popov. Theoretical evidence for $T^{1/2}$ specific heat behavior in carbon nanotube systems. *Carbon*, 42:991, 2004.

[32] T. Yamamoto, S. Watanabe, and K. Watanabe. Universal features of quantized thermal conductance of carbon nanotubes. *Phys. Rev. Lett.*, 92:075502, 2004.

[33] A. C. Bailey and B. Yates. Anisotropic thermal expansion of pyrolytic graphite at low temperatures. *J. Appl. Phys.*, 41:5088, 1970.

[34] J. B. Nelson and D. P. Riley. The thermal expansion of graphite from 15°C. to 800°C.: Part I. experimental. *Proc. Phys. Soc., London*, 57:477, 1945.

[35] S. Baroni, S. de Gironcoli, A. Dal Corso, and P. Giannozzi. Phonons and related crystal properties from density-functional perturbation theory. *Rev. Mod. Phys.*, 73:515, 2001.

[36] P. Giannozzi, S. de Gironcoli, P. Pavone, and S. Baroni. Ab initio calculation of phonon dispersions in semiconductors. *Phys. Rev. B*, 43(9):7231, 1991.

[37] D. Vanderbilt. Soft self-consistent pseudopotentials in a generalized eigenvalue formalism. *Phys. Rev. B*, 41:R7892, 1990.

[38] J. P. Perdew, K. Burke, and M. Ernzerhof. Generalized gradient approximation made simple. *Phys. Rev. Lett.*, 77:3865, 1996.

[39] J. Xie, S. P. Chen, J. S. Tse, S. de Gironcoli, and S. Baroni. High-pressure thermal expansion, bulk modulus, and phonon structure of diamond. *Phys. Rev. B*, 60:9444, 1999.

[40] F. Favot and A. Dal Corso. Phonon dispersions: Performance of the generalized gradient approximation. *Phys. Rev. B*, 60:11427, 1999.

[41] J. C. Boettger. All electron full-potential calculation of the electronic band structure, elastic constants, and equation of state for graphite. *Phys. Rev. B*, 55(17):11202, 1997.

[42] M. C. Schabel and J. L. Martins. Energetics of interplanar binding in graphite. *Phys. Rev. B*, 46:7185, 1992.

[43] P. Pavone, R. Bauer, K. Karch, O. Schütt, S. Vent, W. Windl, D. Strauch, S. Baroni, and S. de Gironcoli. Ab initio phonon calculations in solids. *Physica B*, 219/220:439, 1996.

[44] I. H. Lee and R. M. Martin. Applications of the generalized-gradient approximation to atoms, clusters, and solids. *Phys. Rev. B*, 56:7197, 1997.

[45] K. R. Kganyago and P. E. Ngoepe. Effects of local and gradient-corrected density approximations on the prediction of the intralayer lattice distance c, in graphite and LiC_6. *Mol. Simul.*, 22:39, 1999.

[46] S. Piscanec, M. Lazzeri, F. Mauri, A. C. Ferrari, and J. Robertson. Kohn anomalies and electron-phonon interactions in graphite. *Phys. Rev. Lett.*, 93:185503, 2004.

[47] K. N. Kudin, G. E. Scuseria, and B. I. Yakobson. C_2F, BN, and C nanoshell elasticity from ab initio computations. *Phys. Rev. B*, 64:235406, 2001.

[48] V. Barone, J. Heyd, , and G. E. Scuseria. Interaction of atomic hydrogen with single-walled carbon nanotubes: A density functional theory study. *J. Chem. Phys.*, 120:7169, 2004.

[49] V. Barone and G. E. Scuseria. Theoretical study of the electronic properties of narrow single-walled carbon nanotubes: Beyond the local density approximation. *J. Chem. Phys.*, 121:10376, 2004.

[50] V. Kumar, M. Sluiter, and Y. Kawazoe. Structural transformations in single wall carbon nanotube bundles. *AIP Conf. Proc.*, 590:277, 2001.

[51] P. Pavone. *Lattice Dynamics of Semiconductors from Density-Functional Perturbation Theory*. PhD thesis, SISSA, Trieste (Italy), 1991.

[52] H. Rydberg, M. Dion, N. Jacobson, E. Schroder, P. Hyldgaard, S. I. Simak, D. C. Langreth, and B. I. Lundqvist. Van der Waals density functional for layered structures. *Phys. Rev. Lett.*, 91(12):126402, 2003.

[53] W. Kohn, Y. Meir, and D. E. Makarov. Van der Waals energies in density functional theory. *Phys. Rev. Lett.*, 80:4153, 1998.

[54] W. Kohn and L. J. Sham. Self-consistent equations including exchange and correlation effects. *Phys. Rev. A*, 140:A1133, 1965.

[55] P. Hohenberg and W. Kohn. Inhomogeneous electron gas. *Phys. Rev.*, 136:B864, 1964.

[56] S. Baroni, P. Giannozzi, and A. Testa. Green's-function approach to linear response in solids. *Phys. Rev. Lett.*, 58:1861, 1987.

[57] S. de Gironcoli. Lattice dynamics of metals from density-functional perturbation theory. *Phys. Rev. B*, 51(10):R6773, 1995.

[58] A. A. Maradudin, E. W. Montroll, and G. H. Weiss. *Theory of lattice dynamics in the harmonic approximation*, volume 3 of *Solid-state physics*, pages 45–46. Academic Press, New York, 1963.

[59] A. A. Quong and A. Y. Liu. First-principles calculations of the thermal expansion of metals. *Phys. Rev. B*, 56:7767, 1997.

[60] S. Narasimhan and S. de Gironcoli. Ab initio calculation of the thermal properties of Cu: Performance of the LDA and GGA. *Phys. Rev. B*, 65:064302, 2002.

[61] T. H. K. Barron, J. G. Collins, and G. K. White. Thermal expansion of solids at low temperatures. *Adv. Phys.*, 29(3):609, 1980.

[62] S. Baroni, A. Dal Corso, S. de Gironcoli, P. Giannozzi, C. Cavazzoni, G. Ballabio, S. Scandolo, G. Chiarotti, P. Focher, A. Pasquarello, K. Laasonen, A. Trave, R. Car, N. Marzari, and A. Kokalj. http://www.pwscf.org.

[63] http://www.gnu.org/copyleft/gpl.html.

[64] A. Dal Corso. C.pbe-rrkjus.upf. http://www.pwscf.org/pseudo/1.3/UPF/C.pbe-rrkjus.UPF.

[65] A. M. Rappe, K. M. Rabe, E. Kaxiras, and J. D. Joannopoulos. Optimized pseudopotentials. *Phys. Rev. B*, 41:R1227, 1990.

[66] J. P. Perdew and A. Zunger. Self-interaction correction to density-functional approximations for many-electron systems. *Phys. Rev. B*, 23:5048, 1981.

[67] N. Marzari, D. Vanderbilt, A. De Vita, and M. C. Payne. Thermal contraction and disordering of the Al(110) surface. *Phys. Rev. Lett.*, 82(16):3296, 1999.

[68] W. Kohn. Image of the fermi surface in the vibration spectrum of a metal. *Phys. Rev. Lett.*, 2:393, 1959.

[69] E. Ziambaras and E. Schröder. Theory for structure and bulk modulus determination. *Phys. Rev. B*, 68:064112, 2003.

[70] O. Madelung, editor. *Physics of Group IV and III-V compounds*, volume 17a of *Landolt-Börnstein, New Series, Group III*, page 107. Springer-Verlag, Berlin, 1982.

[71] M. H. Grimsditch and A. K. Ramdas. Brillouin scattering in diamond. *Phys. Rev. B*, 11:3139, 1975.

[72] Y. X. Zhao and I. L. Spain. X-ray diffraction data for graphite to 20 GPa. *Phys. Rev. B*, 40:993, 1989.

[73] M. Hanfland, H. Beister, and K. Syassen. Graphite under pressure: Equation of state and first-order Raman modes. *Phys. Rev. B*, 39:12598, 1989.

[74] J. Donohue. *The Structures of the Elements*, page 256. Kreiger, Malabar, 1982.

[75] O. L. Blakslee, D. G. Proctor, E. J. Seldin, G. B. Spence, and T. Weng. Elastic constants of compression-annealed pyrolytic graphite. *J. Appl. Phys.*, 41:3373, 1970.

[76] J. P. Lu. Elastic properties of carbon nanotubes and nanoropes. *Phys. Rev. Lett.*, 79:1297, 1997.

[77] A. Krishnan, E. Dujardin, T. W. Ebbesen, P. N. Yianilos, and M. M. J. Treacy. Young's modulus of single-walled nanotubes. *Phys. Rev. B*, 58:14013, 1998.

[78] J.-P. Salvetat, G. A. D. Briggs J.-M. Bonard, R. R. Bacsa, A. J. Kulik, T. Stoeckli, N. A. Burnham, and L. Forró. Elastic and shear moduli of single-walled carbon nanotube ropes. *Phys. Rev. Lett.*, 82:944, 1999.

[79] G. Van Lier, C. V. Alsenoy, V. V. Doren, and P. Geerlings. Ab initio study of the elastic properties of single-walled carbon nanotubes and graphene. *Chem. Phys. Lett.*, 326:181, 2000.

[80] C. Oshima, T. Aizawa, R. Souda, Y. Ishizawa, and Y. Sumiyoshi. Surface phonon dispersion curves of graphite (0001) over the entire energy region. *Solid State Commun.*, 65:1601, 1988.

[81] S. Siebentritt, R. Pues, K-H. Rieder, and A. M. Shikin. Surface phonon dispersion in graphite and in a lanthanum graphite intercalation compound. *Phys. Rev. B*, 55:7927, 1997.

[82] H. Yanagisawa, T. Tanaka, Y. Ishida, M. Matsue, E. Rokuta, S. Otani, and C. Oshima. Submitted to SIA, 2004.

[83] R. Nicklow, N. Wakabayashi, and H. G. Smith. Lattice dynamics of pyrolytic graphite. *Phys. Rev. B*, 5:4951, 1972.

[84] F. Tuinstra and J. L. Koenig. Raman spectrum of graphite. *J. Chem. Phys.*, 53:1126, 1970.

[85] H. Zabel. Phonons in layered compounds. *J. Phys. Condens. Matter*, 13:7679, 2001.

[86] I. M. Lifshitz. *Zh. Eksp. Teor. Fiz.*, 22:475, 1952.

[87] C. Kittel. *Introduction to Solid State Physics*, chapter 3. Wiley, New York, 5th edition, 1976.

[88] I. M. Lifshitz. *Zh. Eksp. Teor. Fiz.*, 22:471, 1952.

[89] V. N. Popov, V. E. Van Doren, and M. Balkanski. Lattice dynamics of single-walled carbon nanotubes. *Phys. Rev. B*, 59:8355, 1999.

[90] T. Aizawa, R. Souda, S. Otani, Y. Ishizawa, and C. Oshima. Bond softening in monolayer graphite formed on transition-metal carbide surfaces. *Phys. Rev. B*, 42:11469, 1990.

[91] C. P. Herrero and R. Ramírez. Structural and thermodynamic properties of diamond: A path-integral monte carlo study. *Phys. Rev. B*, 63:024103, 2000.

[92] G. L. Belenkii, R. A. Suleimanov, N. A. Abdullaev, and V. Y. Stenshraiber. Thermal expansion of layered crystals, the Lifshitz model. *Sov. Phys. Solid State*, 26:2142, 1984.

[93] N. A. Abdullaev. Grüneisen parameters for layered crystals. *Phys. Solid State*, 43:727, 2001.

[94] K. Karch, T. Dietrich, W. Windl, P. Pavone, A. P. Mayer, and D. Strauch. Contribution of quantum and thermal fluctuations to the elastic moduli and dielectric constants of covalent semiconductors. *Phys. Rev. B*, 53:7259, 1996.

[95] H. J. McSkimin and P. Andreatch. Elastic moduli of diamond as a function of pressure and temperature. *J. Appl. Phys.*, 43:2944, 1972.

[96] A. C. Victor. Heat capacity of diamond at high temperatures. *J. Chem. Phys.*, 36:1903, 1962.

[97] R. R. Hultgren. *Selected Values of the Thermodynamic Properties of the Elements*. American Society for Metals, Metals Park, Ohio, 1973.

[98] L. E. Fried and W. M. Howard. Explicit gibbs free energy equation of state applied to the carbon phase diagram. *Phys. Rev. B*, 61:8734, 2000.

[99] N. Mounet and N. Marzari. In preparation.

[100] N. Mounet and N. Marzari. First-principles determination of the structural, vibrational, and thermodynamic properties of diamond, graphite, and derivatives. To be published in Phys. Rev. B, 2005.

[101] M. H. Cohen R. M. Pick and R. M. Martin. Microscopic theory of force constants in the adiabatic approximation. *Phys. Rev. B*, 1:910, 1970.

[102] G. H. Golub and C. F. van Loan. *Matrix Computations*. Johns Hopkins University Press, Baltimore, Maryland, 2nd edition, 1989.